WAVELENGTH-AGILE ABSORPTION SPECTROSCOPY FOR MEASURING TEMPERATURE AND H_2O MOLE FRACTION IN HARSH ENVIRONMENTS

by

Laura A. Kranendonk

A thesis submitted in partial fulfillment of the

requirements for the degree of

Doctor of Philosophy

(Mechanical Engineering)

at the

UNIVERSITY OF WISCONSIN-MADISON

2007

WAVELENGTH-AGILE ABSORPTION SPECTROSCOPY FOR MEASURING TEMPERATURE AND H_2O MOLE FRACTION IN HARSH ENVIORNMENTS

Laura A. Kranendonk

Under the supervision of Assistant Professor Scott T. Sanders

At the University of Wisconsin – Madison

This project develops the necessary tools and methods to measure H_2O absorption spectra in harsh environments, and calculate temperature and mole fraction from the measured spectra. Various wavelength-agile sources are designed to obtain absorption spectra. The best performing wavelength-agile laser source for H_2O measurements to date is the Fourier-Domain Mode-Locking laser. Specific procedures are highlighted to best accommodate the measurements in the presence of beam steering and thermal emission. A robust method to calculate temperature and absorber mole fraction is also developed.

Measurements were taken to quantify accuracy in a shock tube and steady burner (used to stimulate gas turbine conditions). Results from HCCI engine measurements demonstrated the precision of the measurements. Temperature results greater than 1000 K have been shown to be biased low. This is a major concern since the main function of the sensor is high temperature combustion studies. Preliminary studies indicate that using a better database for reference spectra should improve these high temperature results.

Acknowledgments

First and foremost, I would like to thank Dr. Scott Sanders for his teaching, motivation, and the numerous opportunities he has provided me. He has been an inspiration due to his passion and commitment to his work. Dr. Jaal Ghandhi has also provided not only significant help and insight during the course of my research, but also supplied the engines which were used to acquire the vast majority of the data in my research. I especially owe his students: Tangwoo Kim, Mark Schwere, Randy Herold, and Sean Younger gratitude for running and maintaining the engines over the years. Their work has allowed my research to go smoothly.

My fellow grad students from the Sander's group each deserve credit for their companionship as well has helpful discussions. Adam Myers, Jon Filipa, Matt Borden, Jason Schmidt, Mandy Pertzborn, Natalie Bednar, Renata Bartula, and Chun Lan have all contributed to aspects of my research over the years. Chris Hagen and Tom Briggs have always been there to commiserate over the stresses of being a PhD student. Drew Caswell constantly writes codes and solves many of the lab's problems. Without Drew around, my data would have been much more difficult to obtain and analyze.

Finally, my family and friends have always been there for me. Without their support, I would not have been motivated to push through the harder stages of this degree. Last but not least, my boyfriend Mike has made my time here at Madison worth staying in school longer than most people ever expected.

Table of Contents

List of Figures

List of Tables

Nomenclature and Variables

α:	Absorbance [1]
AOM:	Acousto-Optic Modulator
ASE:	Amplified Spontaneous Emission
aTDC:	after Top Dead Center
c:	Speed of light [L/Time]
CAD:	Crank Angle Degrees
COV:	Coefficient Of Variation
d:	$1/e^2$ beam diameter [L]
$E"$:	Lower state energy [M L^2 $Time^{-2}$]
E_{CAD}:	Offset due to emission at one CAD
ECDL:	External Cavity Diode Laser
EGR:	Exhaust Gas Recirculation
EICO:	Emissions Index of CO
Δf:	Frequency shift [$Time^{-1}$]
ΔL:	Change in cavity length in one optical round trip [L]
$d\lambda$:	Spectral resolution [L]
$\Delta\lambda$:	Spectral bandwidth [L]
Δn:	Change in refractive index [1]
$\Delta\rho$:	Change in density [ML^{-3}]
ds:	Differential length along a path [L]
f:	Focal length [L]
Φ:	Equivalence ratio [1]
ϕ:	Line Shape [L]
F/A:	Fuel-to-Air ratio [1]
FDML:	Fourier-Domain Mode-Locking
FFP-TP:	Fiber Fabry-Perot-Tunable Filter
FFT:	Fast Fourier Transform
FSFL:	Frequency-Shifted Feedback Laser
FSR:	Free Spectral Range [$Time^{-1}$]
FWHM:	Full-Width Half-Maximum
γ:	Polytropic coefficient [1]
γ_{air}:	Collisional broadening coefficient due to air [Time M^{-1}]
γ_{self}:	Collisional broadening coefficient due to molecule [Time M^{-1}]
h:	Planck's constant [M L^2 $Time^{-1}$]
HITRAN:	**Hi**gh Resolution **TRAN**smission database
I:	Transmitted intensity
I_o:	Initial intensity
IMEP:	Indicated Mean Effective Pressure [M L^{-1} $Time^{-2}$]
k_ν:	Absorption Coefficient [L^{-1}] at wavenumber ν
k:	Boltzman's constant [M L^2 $Time^{-2}$ T]
K:	Beam steering coefficient [L^{-1}]
K_{meas}:	Measured beam steering coefficient [L^{-1}]

L:	Optical path length [L]
L:	Length
λ:	Instantaneous wavelength [L]
ℓ_d:	Kolmogorov length scale [L]
Λ:	Integral length scale [L]
M:	Mass
MSE:	Mean Squared Error [1]
n:	Refractive index [1]
ν:	Optical Frequency or Wavenumber [L^{-1}]
NA:	Numerical Aperture
ND:	Neutral Density
OMA:	Optical Multichannel Analyzer
OSA:	Optical Spectral Analyzer
P:	Pressure [M L^{-1} $Time^{-2}$]
PP:	Peak Pressure [M L^{-1} $Time^{-2}$]
P-P:	Peak-to-Peak
Q:	Partition function [1]
R:	Ratio of ΔL to λ [1]
$\Re$:	Universal gas constant [M L^2 T^{-1} $Time^{-2}$ mol^{-1}]
Re:	Reynolds number [1]
S:	Line Strength [$Time^2$ L^{-1} M^{-1}]
SOA:	Semi-conducting Optical Amplifier
STP:	Standard Temperature and Pressure
T:	Temperature
T_B:	Fractional transmission due to beam steering [1]
T:	Fractional transmission [1]
τ:	Optical round-trip travel time in the cavity [Time]
TDC:	Top Dead Center
θ:	$1/e^2$ optical divergence half-angle [rad]
Θ:	Crank angle degree
T_{IG}:	Ideal gas temperature [T]
T_{ABS}:	Temperature measured from absorption spectroscopy [T]
V:	Instantaneous speed of cavity length change [L/Time]
$\forall$:	Volume [L^3]
X:	Mole Fraction [1]

1 Introduction

Wavelength-agile absorption spectroscopy can be used to measure temperature and absorber mole fraction non-intrusively in harsh, combusting environments. These environments are generally not conducive to more traditional thermometry techniques. This thesis provides an overview for obtaining quantitative temperature and mole fraction measurements from measured absorption spectra. This opening chapter will provide the necessary background for understanding the scope of the project, as well as an overview of the overall organization of the thesis.

1.1 Motivation

In most combustion problems, gas temperature is a critical variable. In many situations, it is the single most important parameter desired for understanding or optimizing the combustion process. Given the tremendous need for reliable thermometry, it is remarkable that there is still no ready temperature measurement solution for numerous combustion problems. The thermocouple is probably the closest approximation to a universal combustion thermometer. Properly corrected (e.g., for radiative losses), it suits many combustion scenarios [1]. Still, the thermocouple is invasive, has a non-negligible time constant, suffers materials limitations above ~2000 C, and can be expensive or awkward to implement in an arrayed format (e.g., to image temperature). For these and other reasons, countless thermometric alternatives have been developed for combustion studies, many of them optical.

Few of the optical thermometry schemes approach the universal applicability of thermocouples. Laser-induced fluorescence (LIF) is limited to reaction zones or seeded tracers [2-4]. Coherent

anti-Stokes Raman scattering (CARS) can effectively measure the temperature of nitrogen [5], however CARS often suffers from interference due to soot/C_2 [6] and is often classified as a complicated or expensive technique. UV absorption of CO_2 [7] may allow more general thermometry, but is ineffective below ~ 1000 K.

There has also been a large body of work on H_2O thermometry by two-line diode laser absorption spectroscopy (see, e.g., [8, 9]). This type of optical thermometry involves measuring a spectroscopic parameter at each of two wavelengths and subsequently solving an algebraic equation for two unknowns (typically temperature and one species mole fraction) [10, 11]. Interference associated with harsh environments (due to window fouling, thermal emission, etalons, and unknown absorbers) can compromise the results. Two-line spectroscopy either relies on very accurate known spectroscopic coefficients at specific wavelengths, or determining these coefficients in well controlled experiments. They also are only accurate in narrow temperature or pressure ranges, and therefore generally designed on a case-by-case basis.

The method presented here relies on H_2O vapor to be present, has no known temperature or pressure limits, and is insensitive to minor errors in spectroscopic databases. The wavelength-agile system is based on direct absorption spectroscopy of H_2O vapor. It provides only path-integrated measurements (potentially enhanced by multi-beam tomography techniques [12] or by inferring distributed properties along the path [13]) and depending on the required measurement bandwidth, real-time data-reduction to temperature may not be possible. Still, it represents a reliable and generally applicable approach to absorption spectroscopy.

One environment in which temperature measurements would be useful is an engine operating under homogeneous charge compression ignition (HCCI). HCCI combustion combines the processes of diesel compression-ignition and gasoline spark-ignition. Fuel is mixed with air upstream of the cylinder (as in a gasoline engine), and ignition is initiated as a function of many factors, but a main one being pressure (as in a diesel engine). The benefits of this type of combustion are high fuel economy, low NOx emissions, and particulate emissions. The major difficulty with this type of combustion is control, since there is no spark plug or fuel injector in the cylinder. Chemical kinetics, specifically temperature, pressure, and concentration, dictate the behavior of the combustion. For these control issues, HCCI remains an interesting combustion process, rather than a viable alternative to diesel and gasoline engines. HCCI combustion is one scenario where temperature measurements are critically important and traditional thermocouples are inappropriate. HCCI combustion represents a suitable environment for demonstrating this sensor's performance because a wide range of pressures (~ atmospheric to 4 MPa) and temperatures (~ ambient to ~ 2000K) is encountered.

1.2 Absorption Spectroscopy

Spectroscopy is governed by the Beer-Lambert law:

$$\left(\frac{I}{I_o}\right)_\nu = \exp(-k_\nu L) \qquad 1.2\text{-}1$$

This law states that that the transmitted intensity (I) divided by the initial intensity (I_o) (or, the fractional transmission) at a specific optical frequency ν [cm^{-1}] is a function of the spectral absorption coefficient k_ν [cm^{-1}] and path length L [cm]. Optical frequency is synonymous with wave number, and both are inversely proportional to wavelength.

The spectral coefficient is a product of total pressure P [atm], mole fraction of the absorbing species X_i, linestrength $S_i(T)$ [cm^{-2} atm^{-1}], and lineshape ϕ_ν [cm]. The product $k_\nu L$ is termed absorbance (abbreviated α_ν). This is summarized in equation 1.2-2:

$$\alpha_\nu = -\ln\left(\frac{I}{I_o}\right)_\nu = PX_i S_i(T)\phi_\nu L \qquad 1.2\text{-}2$$

By scaling the absorbance to PX_i, the equation assumes that the gas obeys the ideal gas law. Non-ideal gas conditions would force the equation to be solved for number density instead of mole fraction. The path length, L, is a scaling factor to absorbance; temperature, pressure and mole fraction are either known or calculated values in the final experiment, leaving linestrength and line shape.

Linestrength is highly dependent on temperature. In order to calculate the linestrength centered at ν_o and at a particular temperature T, the linestrength at a reference temperature $S(T_o)$ [$cm^{-2}atm^{-1}$], the lower state energy E'' [J], and the partition function Q must be known to use the following equation [14]:

$$S(T) = S(T_o)\frac{Q(T_o)}{Q(T)}\left(\frac{T_o}{T}\right)\exp\left[-\frac{hcE''}{k}\left(\frac{1}{T}-\frac{1}{T_o}\right)\right]\left[1-\exp\left(\frac{-hc\nu_o}{kT}\right)\right]\left[1-\exp\left(\frac{-hc\nu_o}{kT_o}\right)\right]^{-1} \qquad 1.2\text{-}3$$

The constants in Eqn. 1.2-3 are: Boltzman's constant k [J/K], Planck's constant h [J*s], and the speed of light c [cm/s]. The left panel of Figure 1-1 shows a plot of linestrength versus line-center in the $\nu_1+\nu_3$ combination band for H_2O using Eqn. 1.2-3 and values from a database of spectroscopic parameters, the HITRAN 2004 database [15].

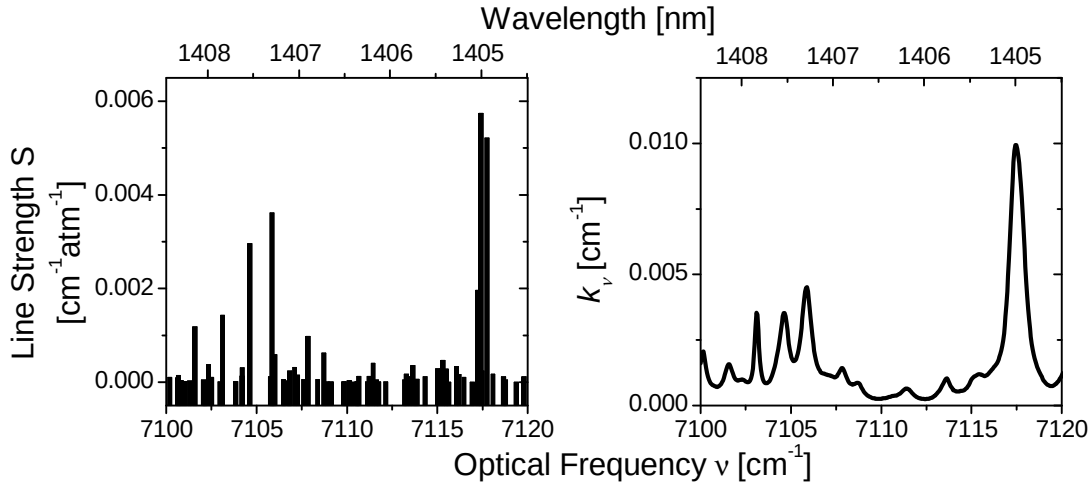

Figure 1-1 - *Left panel:* Linestrength S versus frequency ν using Eqn. 1.2-3 and values from the HITRAN 2004 database at 1500 K. *Right panel:* Absorption spectrum (k_ν) for H_2O at 1500 K, 1.01 MPa, and 5% mole fraction.

Each spectral line is given a spectral shape owing to mechanisms such as Doppler and collisional broadening. Lineshapes (ϕ) can be approximated using a Voigt profile, which combines Gaussian (Doppler) and Lorentzian (collisional) distributions. Both profiles are defined by their full-width at half maximum (FWHM) $\Delta\nu$. The FWHM for Doppler broadening ($\Delta\nu_D$) is defined by Eqn. 1.2-4:

$$\Delta\nu_D = \nu_o\sqrt{\frac{8kT\ln 2}{mc^2}} \qquad 1.2\text{-}4$$

where m is mass [kg/molecule], k is Boltzman's constant [J/K], and c is the speed of light [m/s]. The FWHM for collisional broadening ($\Delta\nu_C$) is defined by Eqn. 1.2-5:

$$\Delta\nu_C = 2P\left[X\gamma_{self}\,n\frac{T_o}{T} + (1-X)\gamma_{air}\left(\frac{T_o}{T}\right)^n\right] \qquad 1.2\text{-}5$$

In Eqn. 5, γ_{self} and γ_{air} [$cm^{-1}atm^{-1}$] are the collisional broadening coefficients due to the molecule and air respectively, along with *n*, the temperature exponent. γ_{air} is generally used to simplify the problem rather than broadening coefficients for specific molecules, although it may be important to consider using specific γ's depending on conditions. The FWHM of the Voigt function for one spectral feature can be estimated as:

$$\Delta\nu_V = \frac{\Delta\nu_C}{2} + \sqrt{\frac{\Delta\nu_C{}^2}{4} + \Delta\nu_D{}^2} \qquad 1.2\text{-}7$$

Further details concerning specifics for implementing the Voigt profile for absorption spectroscopy simulation are reported by Whiting and Hui [16, 17].

Combining the Voigt profile with the linestrengths reported in Figure 1-1, as well as pressure and mole fraction, an absorption spectrum can be simulated as shown on the right panel of Figure 1-1. Figure 1-1 plots H_2O vapor at 1500 K, 1.01 MPa, and 5% mole fraction. Comparing the right and left panels, it becomes apparent how multiple lines can combine to form one spectral feature.

Figure 1-2 summarizes the effects of temperature and pressure on H_2O vapor absorbance spectra. The top panel contains two colder spectra, one at a higher pressure (31 atm), and one at a lower pressure (4 atm). At a constant temperature, it is easy to observe the broadening caused by pressure. Comparing the spectra from the top colder spectra to the bottom hotter spectra, it is also evident that temperature plays a major role in the overall appearance of the spectra.

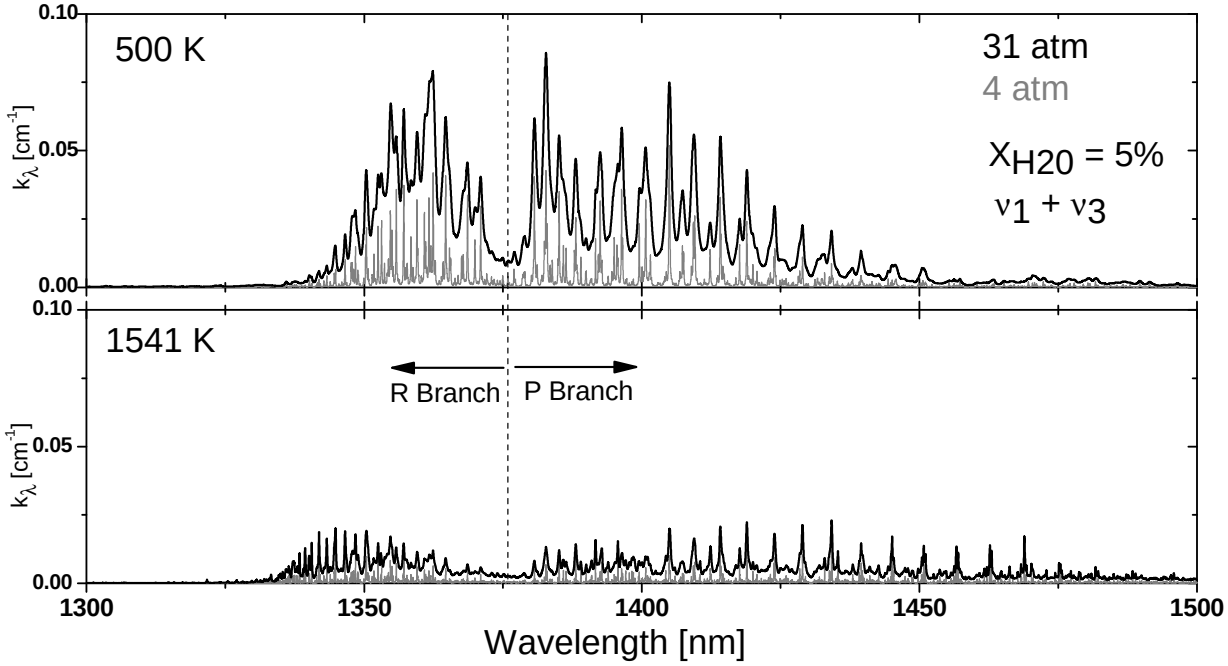

Figure 1-2 – *Lower panel*: Two H_2O vapor absorption spectra (absorption coefficient versus wavelength) simulated at 1541 K. The thicker black line is simulated at 31 atm (3.14 MPa) and the thinner grey line is simulated at 4 atm (0.4 MPa). *Upper panel*: Two H_2O vapor absorption spectra simulated at 500 K. The thicker black line is simulated at 31 atm (3.14 MPa) and the thinner grey line is simulated at 4 atm (0.4 MPa). All simulations contain 5% water mole fraction.

1.3 Thesis Overview

This thesis is organized as follows:

Chapters 2-4 will introduce wavelength-agile lasers. Because wavelength-agile sources are an emerging technology, a major focus of this project was to engineer a light source optimized for temperature measurements. Chapter 2 provides a background and overview to wavelength-agile

designs and applications. Chapter 3 provides an example of a modeless laser which was specifically designed for this experiment. The methodology for wavelength-agile laser design is included. Chapter 4 introduces another laser, which eventually out-performed the modeless laser.

Chapters 5-7 will introduce the issues and solutions that arise when attempting to make optical measurements in harsh environments. Chapter 5 provides a general overview of these issues. Three environments that were tested with the wavelength-agile sensor are presented, and the unique problems that each set of testing condition is presented. Chapter 6 expands on one problem that is inherent to many harsh environments, light being steering due to index of refraction gradients, also known as 'beam steering'. Chapter 7 expands on another issue with harsh environments, thermal emissions.

Chapter 8 describes the calculation method to convert measured laser light intensity into temperature and H_2O mole fraction results. A method is also presented for calculating pressure; however current wavelength-agile lasers do not have the required resolution to make these calculations very accurate.

Chapter 9 presents temperature and H_2O mole fraction results from HCCI engine measurements. The results are analyzed to see if they pass basic common sense and basic thermodynamic tests. A discussion of precision and accuracy is also presented. Accuracy is measured based on shock tube and gas turbine measurements.

Finally, Chapter 10 provides a practical application for this sensing strategy. The temperatures from a HCCI engine were measured at different operating conditions. CO emissions defined at which engine conditions acceptable combustion transitioned to unacceptable combustion, as defined by too much CO in exhaust gases. The peak temperatures in these critical conditions were compared with temperatures previously reported in the literature.

2 Light Source Engineering I: Wavelength-Agile Introduction

This chapter introduces the motivation for designing wavelength-agile light sources. A brief overview of the history of wavelength-agile sources is presented. Alternative strategies to wavelength-agile systems will be discussed, leading to a comparison of advantages and disadvantages. Finally, emerging technology due to improve wavelength-agile systems is introduced.

2.1 Motivation

A wavelength-agile source is one which spans a broad range of wavelengths quickly. Wavelength-agile laser sources are an emerging class of lasers, and therefore the technology is still quite immature compared to more established lasers. Despite the current relatively poor behavior of wavelength-agile lasers, the overall benefits of such systems still make them attractive. They allow broad, complete absorption spectrum to be measured. These measurements contain a wealth of information such as temperature, pressure, and absorber mole fraction. The main motivation for engineering wavelength-agile sources therefore is the ability to measure these quantities non-intrusively in harsh environments.

Temperature measurements in harsh environments are traditionally difficult for a number of reasons. Thermocouples are the most common way to acquire temperature; however, thermocouples are invasive, have non-negligible time constants, suffer material limitations above ~2000 C, and can be expensive or awkward to implement in an arrayed format (e.g., to image temperature). Several optical techniques have been developed to try to compensate for the thermocouple's shortcomings, such as laser induced fluorescence (LIF), coherent anti-Stokes

Raman scattering (CARS), two-line diode laser absorption spectroscopy, and wavelength-agile absorption spectroscopy. These techniques are non-intrusive and have a quicker response time, but they also have drawbacks. For example, LIF typically requires specific tracers [4], and CARS suffers from interference in the presence of soot and is considered expensive and complicated [5]. Two-line diode laser absorption spectroscopy is generally tailored to relatively narrow temperature and pressure ranges [8].

Absorption spectroscopy using a wavelength-agile laser is attractive because water is almost always present during combustion (so no tracer is typically required), species such as soot do not hinder the measurements, an extreme variety of pressure and temperature conditions can be measured with a single source, and simple photodetectors can be used. The main drawback of absorption spectroscopy techniques is the path-integrated nature of the measurements, requiring tomographic reconstruction for temperature imaging. The many benefits of wavelength-agile absorption spectroscopy may outweigh this drawback, particularly when nearly homogenous conditions are present (such as in homogeneous charge compression ignition combustion, detonations or shock tubes) [18]. The following sections expand on the benefits of wavelength-agile sources as means of measuring absorption spectra.

2.1.1 Rapid Response

Many combustion environments require rapid measurements for them to be useful. For example, in the HCCI piston/cylinder engine presented in this project, 500 kHz measurements have been the ultimate goal in order to study high speed engine characteristics. This means that one temperature measurement is obtained in 2 μs. This rate safely assumes that combustion events are considered “frozen”. 5 μs measurements (200 kHz) have been obtained, which are still

useful measurements, especially at slower speeds (600 rpm). For comparisons, the fastest thermocouple response offered by the Omega Engineering, Inc. is 3 ms, or 600 times slower than the wavelength-agile scan (http://www.omega.com/temperature/Z/pdf/z051.pdf). The thermocouples are butt welded and 0.001 in diameter wire.

It is tempting to try to always increase the scanning rate, but at some point the wavelength-agile technology begins to surpass the photodetector technology. The faster the detector, the noisier the detector output tends to be. Detectors that acquire signal faster than 1 GHz have noise that can compromise the measured spectra. For the 200 kHz measurements, an InGaAs 350MHz (Thorlabs, PDB150C) detector was used.

Figure 2-1 shows 50 temperature profiles measured in a firing HCCI engine from the 200 kHz source. The measurements were taken while the engine was warming up, showing cycle to cycle variation. In order to study these transient behaviors, it is important to have sufficiently quick measurements. There are no averages used in Figure 2-1, they are all obtained from single laser scans. There was a 70 μs pause between each measurement (1 measurement every 0.25 CAD), this was only because the data acquisition system had a limited amount of memory. These results emphasize the need for high speed measurements.

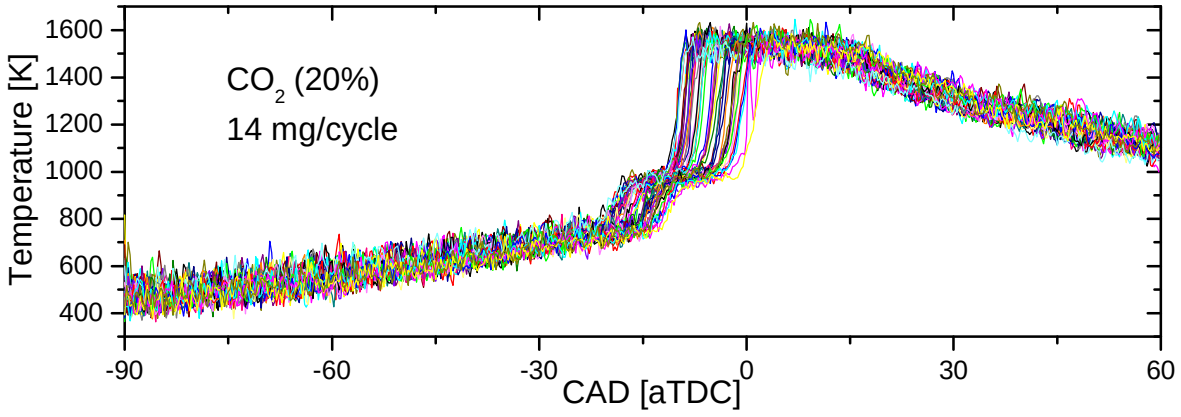

Figure 2-1 – 50 temperature profiles taken in a firing HCCI engine. The measurements were taken while the engine was warming up, showing great cycle to cycle variation.

2.1.2 Spectrally Broad

Wavelength multiplexing is a similar approach to wavelength-agile for obtaining absorption spectra. In wavelength multiplexing, only a few, carefully selected wavelengths are generated (generally 2 – 6 wavelengths). The advantages of multiplexing are that those generated wavelengths have extremely good resolution and stability because they do not rely on immature laser technology. Calculations with wavelength multiplexing generally involve simple or linear algebra. Although the calculations are relatively simple, they rely on specific spectroscopic information to be known and accurate. HITRAN 2004, the latest release of a database which includes spectroscopic parameters relevant to the $\nu_1+\nu_3$ band of H_2O, is known to contain errors [19, 20]. Minor errors in the database could have major effects on temperature (or pressure, or concentration) calculations if those errors include the specific wavelengths designed in the multiplex system. Wavelength multiplexing will also have optimum temperature ranges, depending on which wavelengths are chosen. For example, if the majority of the chosen

wavelengths are near the band center, the system is optimized for cold measurements, and will perform poorly in hot conditions.

On the other hand, there are several advantages to measuring broad spectra as compared to a limited set of wavelengths. Broad spectral measurements will include more information than minimally required. They are immune to 'minor' omissions in the spectroscopic database, meaning that small errors in HITRAN should only have minor effects on calculations.

Another benefit of a broad spectral measurement is that the advanced calculation techniques can be implemented. Chapter 8 will outline a robust method for calculating temperature, pressure, and absorber mole fraction. The advantage to this more complicated calculation method is that low signal to noise ratios can still produce meaningful results. Measuring a complete spectrum will also provide "reality checks". If there are large broadband absorbers, strange etalons, excessive thermal emissions, the broad spectral measurement will paint a more complete picture.

Finally, broad spectral measurements also have the potential to measure multiple absorber species. Figure 2-2 shows absorption strengths of various molecules commonly found during combustion events. Any or even all of these species could be measured with broad sources. Focus on near IR sources has been emphasized because the telecomm industry has developed cheap and robust equipment (fibers, diodes, and photodetectors). There is no fundamental reason that if wavelength-agile systems were developed in other ranges (UV, mid-IR), all species in Figure 2-2 could be measured.

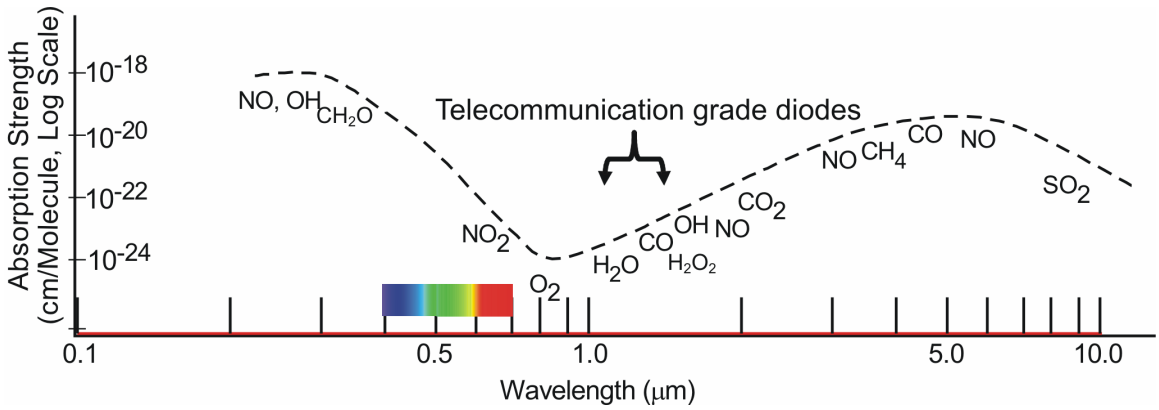

Figure 2-2 – Absorption strengths versus wavelength of species which are found during combustion events [10].

2.2 History

There are a wide range of concepts that create spectrally broad, rapidly scanning light sources. Figure 2-3 is considered a master plot of wavelength-agile sources, most of which have been developed by Professor Sanders. Table 2-1 references the sources presented in Figure 2-3.

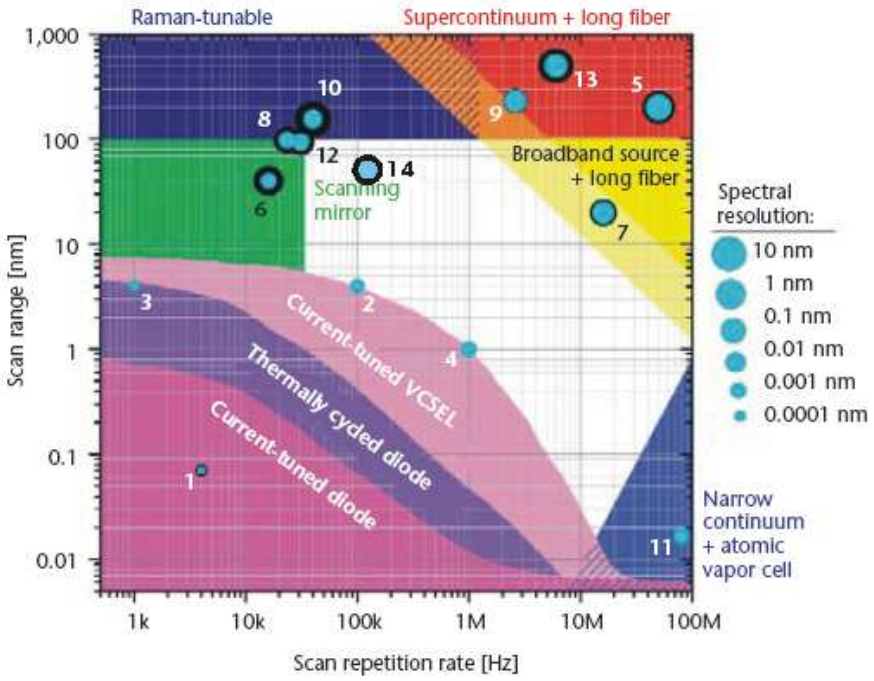

Figure 2-3 – Wavelength-agile map of developed sources as a function of scan rate, range and resolution. Blue dots represent successfully designed lasers. The size of the dot identifies the spectral resolution.

Figure Number	Description	Reference
1	Current-tuned diode laser	[21]
2	Current-tuned VCSEL	[22]
3	Thermally cycled diode laser	[23]
4	Current-tuned VCSEL	[24]
5	Super continuum and long fiber	[25]
6	Scanning mirror ECDL	[26]
7	Broadband source and long fiber	[27]
8	Scanning mirror ECDL	[28]
9	Super continuum and long fiber	[29]
10	Raman tunable	[30]
11	Narrow continuum and atomic vapor cell	[31]
12	Scanning mirror ECDL	[32]
13	Super continuum and long fiber	[29]
14	Fourier-domain mode-locking laser	[33]

Table 2-1 – Description and references for the wavelength-agile sources from Figure 2-3.

This project has focused on scanning mirror wavelength-agile sources (lasing and non-lasing) and the FDML laser. Other types of sources represented in Figure 2-3 have various advantages and disadvantages over these two systems. The focus here is not to describe each approach (see references from Table 2-1 for details), but to introduce the topic of wavelength agility, and expand on the pertinent systems.

2.2.1 Non-Lasing Systems

Wavelength-agile systems do not need to lase to be useful. Lasing will provide more optical power, but as long as there is a sufficient signal to noise ratio in the final measured spectrum, lasing is not required. Figure 2-4 diagrams the first wavelength-agile source that was created in the Sander's research laboratory.

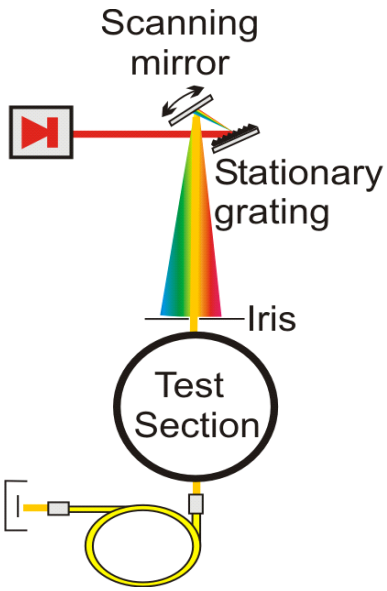

Figure 2-4 – First generation wavelength-agile system.

This source had light originate from a diode and directed at a diffraction grating. The light from the grating was directed at a scanning mirror. The oscillating light then traveled through a small iris. Although significant optical power was thrown away at the iris, temperature calculations could still be performed [27]. The reason that this is worth mentioning is that it opens the door for spectral ranges that may not have convenient sources conducive for lasing, which would allow new species measurements.

2.2.2 External Cavity Diode Lasers

In a typical external cavity diode lasers (ECDL), great care is taken to ensure that the cavity path length remains at a fixed multiple of laser wavelengths as the laser tunes [34], thus ensuring single-mode tuning. However, at these speeds such precise motions become a daunting requirement. Since the high-pressure H_2O absorption features of interest here are relatively broad (42-105 GHz), the precision length requirement was ignored and the laser was allowed to operate in a multi-mode fashion.

The first wavelength-agile ECDL that was designed in this laboratory is shown in Figure 2-5. External cavity diode lasers are convenient because of their simplicity to build; however, they do have several drawbacks such as moving parts, one scan superior to another (eliminating continuous monitoring), and unstable and poor spectral resolution. This section will describe the construction and consideration of the laser in Figure 2-5. A more advanced ECDL laser will be presented in the next chapter.

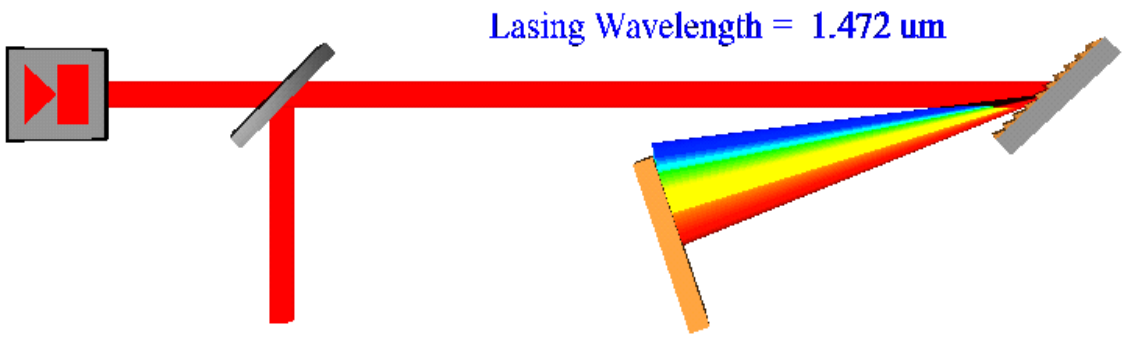

Figure 2-5 – Wavelength-agile external cavity diode, used to measure temperature at 11.7 kHz.

A diode equipped with one anti-reflecting facet (from a New Focus model 6327 ECDL) was aligned within a modified Littman-Metcalf cavity as shown in Figure 2-5. The cavity consisted of the diode, a beam splitter, an 1100 g/mm holographic grating, and a plane mirror. The grating was mounted on a resonant scanner vibrating at 11.7 kHz. The laser system was contained in a sealed box and purged with nitrogen to avoid water absorption within the cavity. The vibrating grating forced the diode laser to sweep from 1374 to 1472 nm in 42.5 μs, and then to return from 1472 to 1374 nm in the next 42.5 μs. Note that 42.5 μs corresponds to 0.15 crank angle degree in a 600-rpm engine.

The laser tuned simply by hopping among the ~24,000 cavity modes available in the 1374-1472 nm range. The mode spacing was 600 MHz, fixed by the 25 cm cavity length. The laser was forced to hop among these modes by the scanning grating. However, the grating's bandpass encompasses ~ 25 modes, and the laser was free to hop between any one of these 25 modes at any instant. Thus, when examined under high resolution, the laser tuning was unstable on a scan-to-scan basis. For example, when low-pressure spectra are acquired with the laser, the

absorption line heights fluctuate as the laser hits a line during one scan but misses it during the next.

The next chapter (Light Source Engineering II: Modeless External Cavity Diode Laser) will introduced an improved design. Many of the issues mentioned above are eliminated by this modeless operation.

2.3 Alternatives Strategies

Commercial methods for measuring spectra have been available for quite some time. Figure 2-6 diagrams the most basic scheme for obtaining a spectrum. Light from any source (light bulb, laser, diode) is directed through a test section and typically collected into a fiber. The fiber then brings the light to the commercial device. The main idea of these devices is that the light hits a diffraction grating and either a camera or an array of detectors then identifies the spectrum. Figure 2-6 is one basic form of a class of a grating spectrometer, or optical spectral analyzers (OSA).

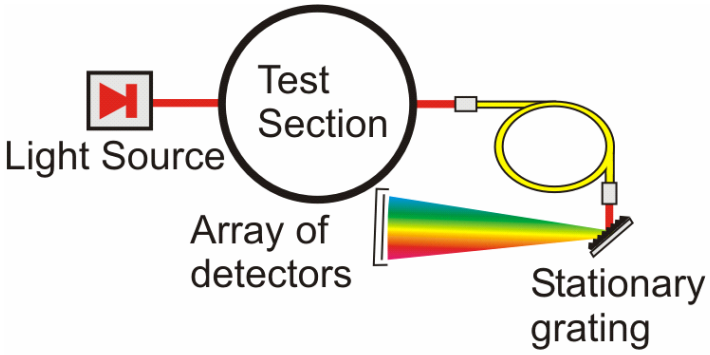

Figure 2-6 – Optical spectral analyzer configuration.

OSA's are convenient because of their commercial availability. They also generally have superior spectral resolution. They are currently too slow to acquire spectra at a meaningful rate in environments such as an engine. Also, the spectral resolution of the measurement is compromised if large fibers are used to collect the light. This could be a problem in measurements such as piston/cylinder engines where there is a high level of beam steering. On one hand, large fibers may be the only way to collect sufficient light; on the other hand, the resolution may be too poor to derive any useful information from the spectrum. This problem is studied in detail in Chapter 6.

Figure 2-7 is a plot of 50 temperature profiles taken in a firing HCCI engine under steady conditions. The measurements were taken after the engine had sufficient time to warm up. In this case, there is less cycle-to-cycle variations than Figure 2-1. It may be possible to use commercial grating spectrometers in steady conditions by employing advanced averaging schemes, such as phase locked cycle-to-cycle averaging.

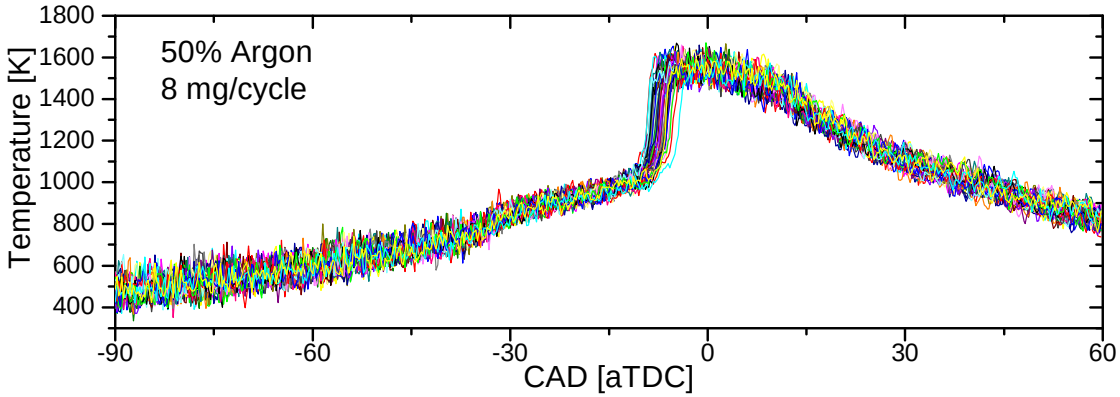

Figure 2-7 – 50 temperature profiles taken in a firing HCCI engine under steady conditions. The measurements were taken after the engine had sufficient time to warm up.

3 Light Source Engineering II: Modeless External Cavity Diode Laser

The previous chapter introduced the motivation and a brief history of wavelength-agile light sources. This chapter describes an external cavity laser that was designed to measure temperature in an HCCI engine. This source was ultimately out-performed by another (as described in the next chapter). The process of designing the light source by developing novel software to optimize the configuration led to interesting results. "Modeless" configuration may alleviate some issues associated with wavelength-agile sources.

3.1 Modeless Operation

Laser designs generally incorporate laser cavities, which in turn generally define cavity modes. The cavity modes tend to enforce lasing at specific "resonant" wavelengths. For this reason, cavity modes tend to narrow the spectral width of the laser output. Narrow spectral width is a common laser characteristic, and is considered useful in some applications, including interferometry and high-resolution spectroscopy.

Lasers that can be scanned over a broad wavelength range are becoming increasingly popular for a variety of applications [see for example, [35]]. In a common tunable laser design, single-mode operation is maintained by increasing the cavity length as the laser wavelength is increased so that a fixed number of wavelengths precisely fill the cavity.

Unfortunately, as the tuning speed is increased, the ability to maintain precision cavity lengths and single-mode operation becomes increasingly challenging. In applications such as wavelength-agile absorption spectroscopy [28] and optical frequency-domain imaging [36],

broad wavelength scans (> 5% of the center wavelength) in short times (< 50 μs) are particularly useful. At these tuning rates, one approach is to abandon the precision cavity length adjustment and allow multimode laser operation. Example multimode lasers include [28, 37, 38]; such lasers tune by "hopping" among cavity modes. A simplified picture is as follows. A large number of laser modes (typically of order 10^5) exist in the laser's tuning range. The tuning element, which is typically a vibrating or rotating mirror paired with a diffraction grating, promotes lasing among some narrow distribution of these modes at any instant. The center wavelength of the distribution is swept by the tuning element. Such multimode lasers are relatively simple to construct, and tuning speeds may be limited only by the tuning element itself.

Compared to the single-mode approach, the multi-mode option presents at least three possible drawbacks. First, the output no longer actually scans in wavelength, but rather "hops" among available modes in some fashion. Second, the details of the spectral behavior of each scan are generally different, because of the stochastic distribution of laser power among available modes. Finally, the instantaneous spectral width of the output is generally broader than in the single-mode case. The novel laser design presented here attempts to resolve the first two issues above by eliminating laser modes altogether. Figure 3-1 diagrams the basic configuration of this new modeless laser design.

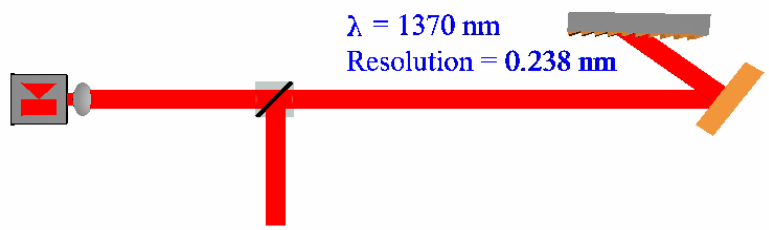

Figure 3-1 - Single pass wavelength agile, modeless, external cavity diode laser. The mirror on the far right vibrates sinusoidally.

Reduction of mode build-up has been previously reported using frequency-shifting elements within the cavity [39, 40]. Typically, an acousto-optic modulator (AOM) is used to constantly shift the feedback frequency of the circulating light, so that a single mode no longer resonates. This approach works even for fixed-wavelength lasers; for example Lim [39] demonstrates the linewidth broadening occurring in a fixed-wavelength laser when the AOM is turned on. Yoshizawa [40] characterizes such "frequency-shifted feedback lasers" (FSFLs) in terms of the ratio of the frequency shift (Δf) encountered in one optical pass to the cavity free spectral range (FSR). We term this ratio "*R*", and below discuss the performance of our design in terms of an analogous ratio. Yoshizawa studies *R* ranging from 0.21-1.4; the laser discussed in this paper encompasses *R* values of 0-0.85.

The primary goal for the present laser design is to eliminate the effect of cavity modes. In a fashion analogous to FSFLs, this occurs in our laser by rapidly modulating the cavity length to prevent resonance of preferential wavelengths within the cavity. Because of the arrangement of the grating shown in Figure 3-1, the wavelength scanning is accompanied by cavity length change. The speed (*V*) is the instantaneous time derivative of the cavity length. Because the

mirror vibrates sinusoidally, V varies in an approximately sinusoidal fashion as well. Figure 3-1 also shows ΔL, the instantaneous change in cavity path length occurring in the optical round-trip time (τ).

In reference [40], the R is defined in terms of the frequency shift of light occurring in one round trip due to the AOM, Δf, and the cavity free spectral range (FSR) as

$$R = \frac{\Delta f}{FSR} \qquad 3.2\text{-}1$$

If the acoustic waves in the AOM were truly decreasing the cavity length at speed V, then we could express Δf as:

$$\Delta f = \frac{V}{c} f = \frac{V}{\lambda} = \frac{\Delta L}{\tau \lambda} = \frac{\Delta L \cdot c}{2L\lambda} \qquad 3.2\text{-}1$$

and thus R as

$$R = \frac{\Delta f}{FSR} = \frac{\Delta L c / 2L\lambda}{c / 2L} = \frac{\Delta L}{\lambda} \qquad 3.2\text{-}3$$

Thus the AOM and variable-length cavity, though different means of eliminating laser modes, can be characterized by analogous R values. The ratio of ΔL to the wavelength, termed R in this paper, is an important parameter because it governs the suppression of laser modes. With $R \approx 0$, the laser behaves as an ordinary multimode tunable laser.

3.2 Laser Design

Based on the need for a wavelength-agile laser cavity with well-behaved wavelength tuning, a new “modeless” laser configuration was developed. The design was first optimized using a

computer animation, the details of which are provided in the next section. The actual laser was then assembled and tested to confirm the predicted results.

3.2.1 Computer animation

Before the laser was constructed, the configuration and specifications were optimized using a computer simulation. The simulation was facilitated by an imaging program (Persistence of Vision – Ray Tracer, 'POV-Ray') used to animate the path of the light as well as calculate the instantaneous lasing wavelength and theoretical spectral resolution. The code modeled the inputs as grating grooves per millimeter, beam diameter, grating angle, and other cavity geometries. Cavities employing both single (Figure 3-1) and double (Figure 3-2) passes off the grating were studied. The factors used to determine the optimal set-up were the spectral resolution, maximum speed of the cavity length change (V_{max}), maximum R, total cavity length, and ease of construction. A summary of representative simulation results are shown in Table 3-1. For typical application in an HCCI engine [28], high resolution is desirable for monitoring gas absorption features, particularly at low pressure. Short cavity lengths are desired to facilitate rapid scanning: if the cavity is too long, there are too few optical round trips before the spectrum fed back from the grating changes appreciably, and the laser performance degrades (see discussion section). High cavity speed is desired to for increased suppression of laser modes. Designs involving a double-pass off the grating (defining the end of the cavity with a mirror after the grating rather than the grating itself, as shown in Figure 3-2) were rejected because of marginal improvement in spectral resolution for the increased complexity, as well as longer total cavity lengths. The single pass geometry (Figure 3-1) was therefore chosen because it represented the simplest version that met our needs.

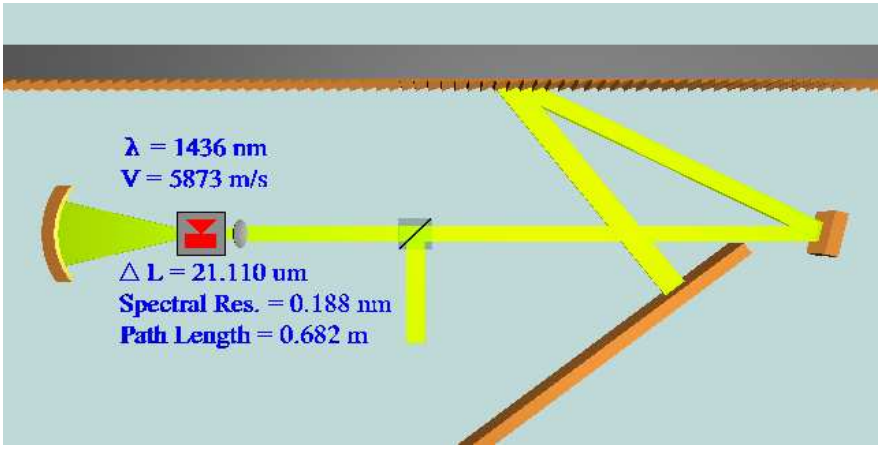

Figure 3-2 - Double pass external cavity diode laser design with instantaneous cavity speed (V), change in cavity length in an optical round trip (ΔL), spectral resolution, wavelength (λ), and total path length using a 1050 grooves/mm grating.

Grating Passes	Available Grating [grooves/mm]	Spectral Resolution (max) [nm]	V_{max} [m/s]	R_{max}	Path Length (ave.) [m]	Grating Width [cm]
Single	1200	0.287	662	0.85	0.27	2
Single	1050	0.429	241	0.31	0.27	2
Single	950	0.501	143	0.18	0.27	2
Single	750	0.661	59	0.07	0.27	2
Double	1200	0.136	39,000	150	1.48	90
Double	1050	0.188	5,873	14.8	0.63	9
Double	950	0.228	3,553	8.27	0.59	5
Double	750	0.314	1,122	2.24	0.57	2

Table 3-1 - Results from computer simulations, where single pass geometry is shown in Figure 3-1, and double pass is shown in Figure 3-2.

3.2.2 Laser Construction

The details of the final (single pass) design shown in Figure 3-1 are as follows. A broadband semiconductor pump chip (developed at the Ahura Corp., part number 102D) was used as the gain element. This element was angle-faceted to eliminate the possibility of forming additional

cavities within our designed cavity. A high quality spherical mirror (Optosigma 035-0150, λ/4 sphericity) formed one end of the laser cavity. However, this spherical mirror was only ~ 10% efficient in coupling light back into the semiconductor waveguide, thus in future designs we are pursuing angle-flat chips with the flat surface defining this end of the cavity. The gain element was mounted in a fixed location. The spherical mirror and lens were each mounted on high-sensitivity XYZ stages (Thorlabs MDT616). The collimated light was directed at the resonant scanner (Electro-Optical Systems, Inc, SC30, 3mm x 3mm plane mirror, 15.54 kHz resonant frequency), set on a four-axis stage (New Focus 9071). The amplitude of the mirror oscillation was adjustable, but the frequency was not. The light from the vibrating mirror was then directed at the plane ruled diffraction grating (Edmund Scientific, NT55-263, 1200 g/mm), mounted on a kinematic mount that allowed for rotation of the grating grooves (New Focus 9481). A 50:50 beamsplitter cube (Edmund Scientific R47-235) was used to extract the laser beam. Two beams emerge from the cube, but we only use the one shown, because the other one could be contaminated by amplified spontaneous emission (ASE) that is not rejected by the grating. Note that light also leaks out the cavity from the zeroth-order diffraction from the grating, but in addition to possible ASE contamination, this light scans in space and is therefore not easily usable. The beam extracted at the beamsplitter cube is coupled into a single-mode fiber for delivery to the end-use.

The average cavity length (L) was 0.27 m, corresponding to a free spectral range of 553 MHz. The average output power was 5 mW, and the measured instantaneous linewidth was 0.3 nm, determined by comparing a measured and simulated atmospheric-pressure H_2O vapor spectra.

Note that the measured linewidth is approximately 1.3 times larger than the calculated spectral resolution, possibly because of imperfect alignment of the beam in the cavity.

3.2.3 Modeless operation observations

Figure 3-3 illustrates several important features of the laser. The bottom panel presents the output power versus time for the laser shown in Figure 3-1. The large variation during tuning shown on the bottom panel of Figure 3-3 is an effect of the finite bandwidth of the gain element. The maximum gain of the element occurs roughly at 1430 nm, and there is simply less gain at the endpoints of the scan. The maximum change in cavity length speed is 1190 m/s, corresponding to ΔL of 2.1 μm, an R of 0.85, and λ_1-λ_2 from 1370-1464 nm. R passes through zero at the edges of the scan because of the sinusoidal motion, but in the bottom panel, transition to ordinary multimode behavior is not observed. The middle panel shows that when the mirror vibration amplitude is decreased (λ_1-λ_2 = 1398-1441 nm) slowing the maximum V to 587 m/s, evidence of cavity modes are occasionally seen at the extremes of the scans, where R passes through zero. Finally, the top graph shows a very slow change in cavity length (V_{max} = 13.6 m/s, λ_1-λ_2 = 1418.5-1419.5 nm). Here, the laser scan is strongly affected by laser modes. The laser exhibits a stronger and cleaner signal when cavity modes prevail. Although the “modeless” operation is “noisier”, it is preferred because of the spectral behavior during the scan. Based on the results shown in Figure 3-3, when $R \approx 0.005$ or lower, it is possible for the laser to develop cavity modes.

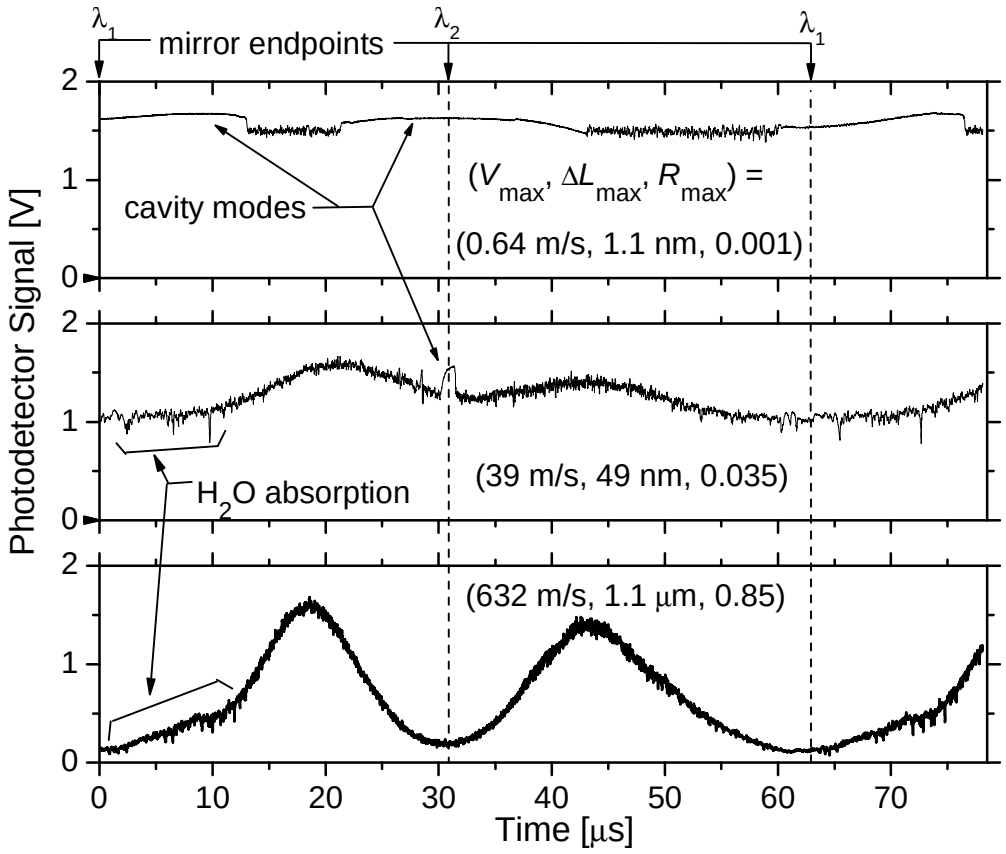

Figure 3-3 - Elimination of cavity modes. The bottom panel is the laser signal as set up for Figure 3-1 (λ_1-λ_2 is 1370-1464 nm). The middle panel shows a slower mirror oscillation, with λ_1-λ_2 = 1398-1441 nm. Finally, the top panel shows a very slow change in cavity length, and the cavity mode effect (λ_1-λ_2 = 1418.5-1419.5). Corresponding V_{max}, ΔL_{max} and $R_{\max}$ values are given.

Careful examination of Figure 3-3 reveals some non-ideal aspects of the laser performance. First, there is the intensity noise during the scan, as mentioned above. Second, the intra-cavity water absorption features visible in Figure 3-3 are not symmetric in blue-to-red and red-to-blue scan directions. Both of these issues are associated with fiber-coupling the laser light extracted

from the cavity. If a large multimode fiber is used, rather than the single-mode fiber used to collect the data shown in Figure 3-3, these issues disappear. Therefore we believe the circulating beam contains multiple spatial modes. It is expected that using a single-mode fiber coupler rather than a beamsplitter cube to extract light from the cavity would force the circulating light to be single-mode at the extraction point and therefore improve the situation. An alternative would be to simply use multimode fiber to deliver the extracted light to the end use; however, our application suffers from a "fiber mode noise" in this configuration [28]. Therefore, the present solution is to couple into a single-mode fiber and correct for the intensity noise with a reference detector.

3.3 Sample Results

A H_2O vapor spectrum was measured in a high pressure (7 bar), room temperature cell, with ~0.63% mole fraction concentration of water vapor. The raw data is shown in Figure 3-4. This data is obtained as follows. The fiber-coupled light from the laser cavity is separated using a 90/10 fiber splitter, such that 90% of the light is directed through the high pressure cell, and 10% is coupled directly to a reference photodetector (I_o). The light directed through the test cell is then coupled into a 62.5μm multimode fiber which is connected to a separate photodetector (I). A single-mode coupler in the path through the cell was decoupled to balance the signal powers. Care was taken to balance the length of the light paths leading to the I and I_o photodetectors so that the signals were synchronized.

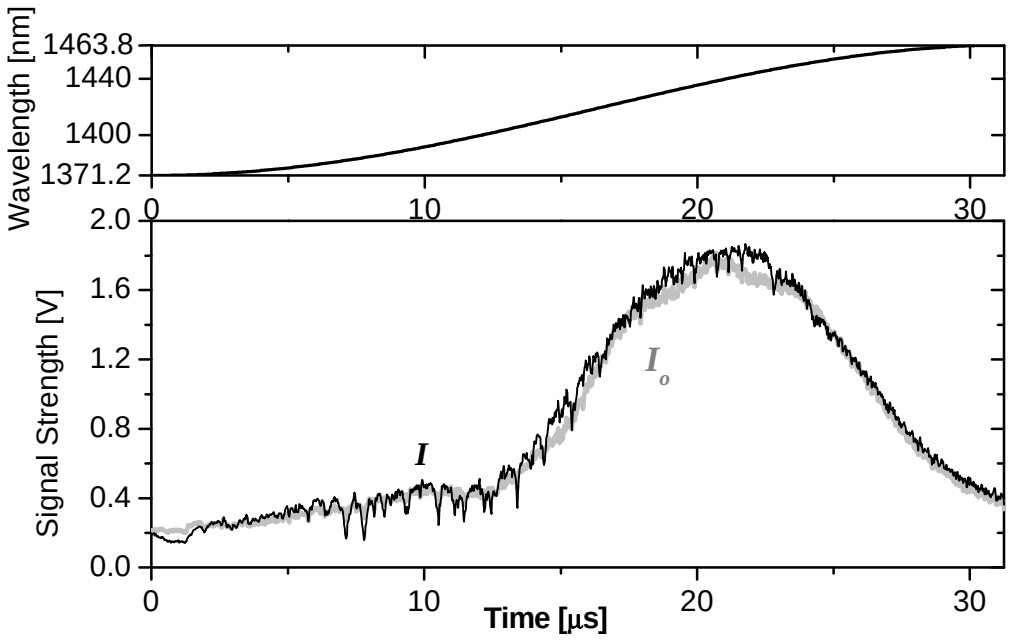

Figure 3-4 - Raw data signals taken from a high pressure (7 bar) cell at room temperature. *I* is the signal recorded after the cell, and I_o is the signal directly out of the laser. A fiber splitter was used to record *I* and I_o simultaneously. The upper panel correlates time with wavelength.

Figure 3-4 can be converted into an absorption spectrum (Figure 3-5) using Beer's Law and a baseline fit as described in Chapter 8, and converting time into wavelength based on the sinusoidal mirror motion.

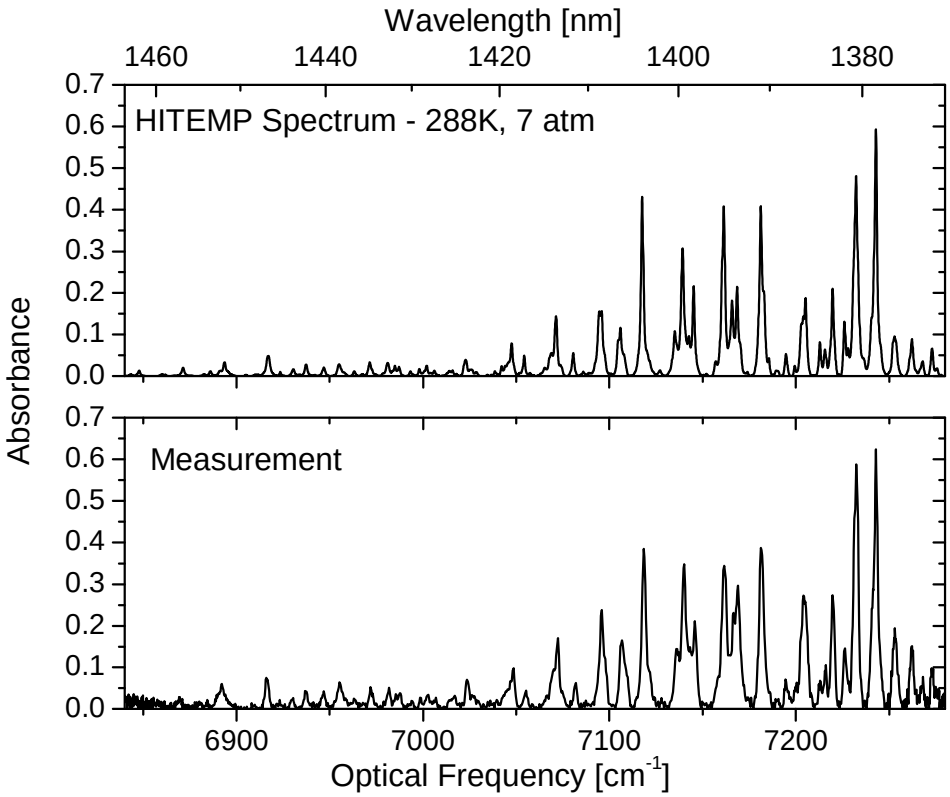

Figure 3-5 - A sample water spectrum measured in a high pressure cell at room temperature. The top panel shows the corresponding spectrum generated from the HITEMP database.

3.4 Discussion

In this paper the cavity length changes by as much as 85% of the wavelength in an optical round trip (R = 0-0.85). R can be adjusted in future designs in many ways. For example, a simple lengthening of the cavity increases R (by increasing the round trip optical travel time, thus increasing ΔL). Unlike the frequency shift associated with an AOM, the cavity length changes here can be easily varied with cavity geometry. For example, achievement of much larger R values (say $R \sim 10$), or achievement of similar R values in a shorter cavity, should be straightforward. By increasing the size of the grating and the distance from the grating to the scanning mirror, the effective cavity speed can be dramatically increased. The laser presented in

this chapter tunes at a maximum rate of 4.6 nm/μs, corresponding to a wavelength change of 0.3% per microsecond. This tuning rate represents an approximate upper limit using available resonant scanning mirrors.

Because the laser output is modeless, it is of random phase, in contrast with traditional laser output. This feature may also be of use in some applications. For example, in some imaging applications, an undesirable "speckle" is caused by the phase coherence of the illuminating laser. If the laser described in this paper were used for imaging, we expect that such speckle would be reduced or eliminated.

This chapter introduced a swept-wavelength laser that features mode-free spectral output. The longitudinal cavity modes are suppressed by rapid cavity length changes that accompany the rapid wavelength scans. The modeless nature permits continuous wavelength scans with reliable instantaneous spectral structure. The laser was designed for high-speed absorption spectroscopy but may be useful in many other high-speed measurement applications as well. The cavity design should be transferable to other types of lasers, such as external-cavity dye lasers. Compared with previous external-cavity laser designs based on precision length adjustment or AOMs, the cavity-length modulation approach described here is relatively simple and cost-effective.

4 Light Source Engineering III: Fourier-Domain Mode-Locking Laser

Although significant effort was invested in creating an acceptable ECDL, there were several issues inherent to ECDL's that would always cause problems. Specifically, the vibrating mirror was difficult to work with because it had a "wobble" in the vertical direction. This made the lasing unsteady. Also, since the laser was designed in the free space, it required purging. The easiest way to purge was to flood the laser's housing with nitrogen. When the nitrogen flowed into the housing at a high enough rate to eliminate normal humidity, the nitrogen flow would create beam steering which caused unstable scan to scan intensities. Finally, due to the nature of the diffraction grating, spectral resolution was a function of wavelength. These problems generally complicated measurements and calculations.

While working on improvements to the wavelength-agile ECDLs, Prof. Fujimoto and Dr. Huber at Massachusetts Institute of Technology (MIT) were developing a Fourier-Domain Mode-Locking laser for use in optical coherence tomography [41]. This laser ultimately outperformed the ECDL sources, and was chosen to be used to complete the HCCI temperature measurement project. The laser scans 1330-1380 nm in 5 μs with 0.1 nm resolution. Much better resolution can be achieved at smaller bandwidths. Specific details about the laser can be found from several references by Fujimoto and Huber [33, 41-43]. This chapter will not attempt to re-write their references, it will simply provide a brief overview of the laser's operation as it pertains to wavelength-agile absorption spectroscopy measurements, and an outlook for laser improvement.

4.1 FDML Operation

The FDML is completely fiber based, making it robust and easy to transport. The light source for the system is a fiber coupled semiconductor optical amplifier (SOA, from InPhenix, Inc.). The light is optically tuned with a piezoelectric transducer actuated fiber Fabry-Perot tunable filter (FFP-TF from Micron Optics, Inc.). There are also two isolators (before and after the SOA) to ensure unidirectional lasing, a 70:30 beam splitter that removes 30% of the light from the cavity for use, and a polarization controller. The FFP-TP is tuned in resonance to the roundtrip time in the cavity. A big advantage to this laser compared to previously described ECDL's is that lasing does not have to build up repeatedly from amplified stimulated emission while the filter is tuned in wavelength. Instead, the SOA is seeded by light from previous frequency sweeps [42].

Figure 4-1 diagrams the initial process of the FDML. The initial steps are outlined below:

A. Light off. Grey lines symbolize fibers, the top 2 parallel rectangles symbolize the FFP-TF, the bottom box symbolizes the SOA, and the right grey box is the beam splitter.

B. Broadband light is emitted from the SOA. Notice the space between the filter plates has expanded. This spacing is synchronized to the time of flight of the light within the cavity.

C. Broadband light has reached the FFP-TF. The filter is at the maximum distance between plates.

D. As the light passes through the filter, only one color is allowed to pass. Because the FFP-TF is operating in a sinusoidal domain, the light is also being filtered in a sinusoidal domain.

E. The first light that passed through the FFP-TF makes it back to the SOA. This light will now cause amplified stimulated emission in the SOA, lasing the light.

F. Amplified light in the sinusoidal domain is initially emitted from the SOA.

G. Amplified light makes it to the filter. Assuming the frequency of the filtered light was correctly synchronized with the path length of the fiber, the light will pass through the FFP-TF.

H. Amplified light, seeded from the initial sweep, passes through the FFP-TF.

I. Amplified light makes it back to the SOA. The laser should now be at a steady condition.

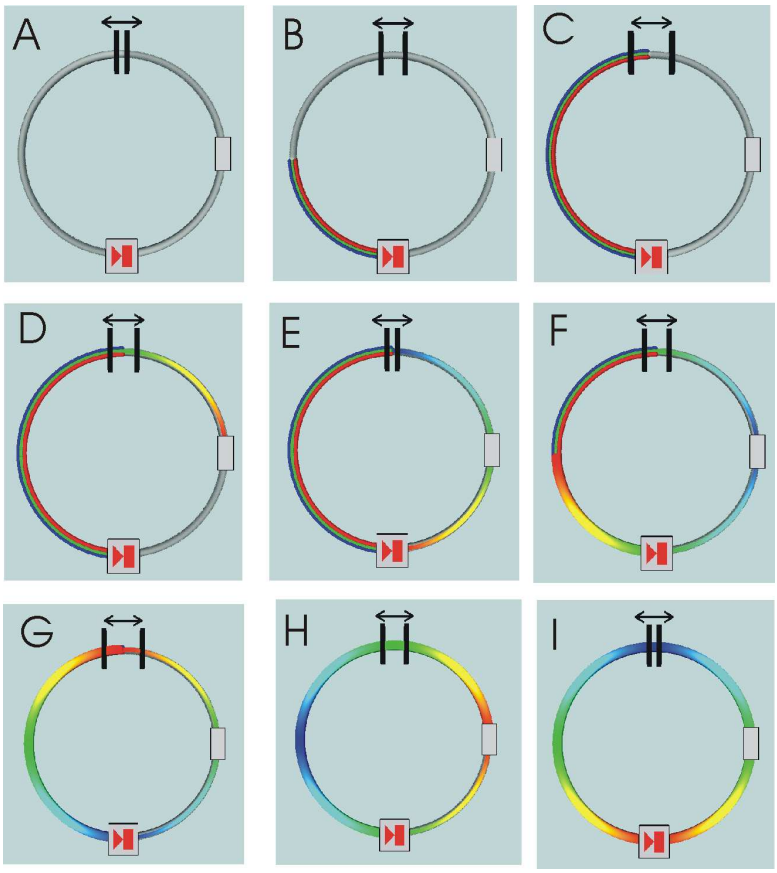

Figure 4-1 – Initial process FDML laser.

Figure 4-2 shows the FDML as it would operate during steady conditions. It includes the beam splitter to the right.

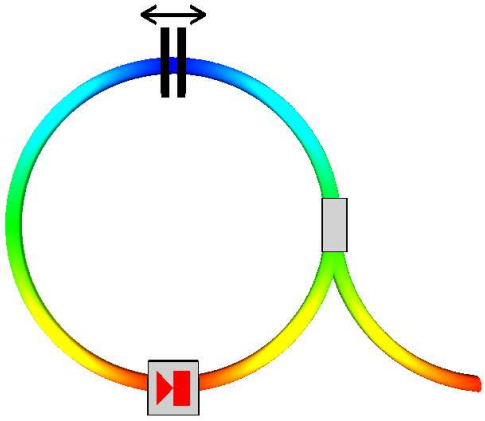

Figure 4-2 – Steady state diagram of FDML laser.

4.2 Improvements

The FDML laser offers improved quality and performance compared to similar wavelength-agile sources. There are, however, still some improvements that could be made. The SOA that is currently being used has very different characteristics depending on the polarization of the amplifying light. The fiber and other components are not polarization maintaining however. Over time, the laser begins to behavior differently because of these polarization issues. InPhenix is currently in the process of creating a SOA that does not have a polarization dependency. This new SOA may improve the overall performance of the system.

The other main issue that this laser has is that the laser has been observed to jump over wavelengths, very similar to the mode-hopping issues that were discussed in Chapter 2. The hypothesis for this behavior is that one color is building up slightly more power than surrounding colors. This will lead to the surrounding colors to be skipped during amplification for several

rounds trips. This mode hopping problem mostly compromises low pressure measurements, which will be discussed in Chapter 9. To fix the mode hopping, perhaps the polarized independent SOA will help. Also, optimizing the percentage of light that is removed from the cavity may help as well.

4.3 Outlook

Overall, the FDML laser is the most reliable wavelength-agile source to date. It is easy to change the SOA, allowing various wavelength ranges to be tested. For example, aside from the 1330-1380 nm range that is reported in this thesis, a SOA with a 1395-1455 nm range has been successfully tested. As fiber based SOA's are improved and their spectral ranges expanded, this laser's potential will also expand.

5 Harsh Environments I: Experimental Considerations

5.1 Introduction

This chapter will introduce some of the problems that arise when attempting to obtain absorption spectra in harsh environments. Further details will be described in the proceeding chapters concerning beam steering and thermal emissions. Along with the introduction of potential issues with harsh combusting environments, a description of three experiments performed in separate harsh environments will be presented: HCCI piston engine, gas turbine combustor, and shock tube. The specific challenges involved with each of the setups will be covered.

5.1.1 Beam Steering

Beam steering is the wander and dispersion of laser light due to index of refraction gradients. Since the index of refraction is a function of density, turbulent fields, especially with temperature and pressure gradients, will cause some amount of beam steering. The main issue with beam steering in absorption spectroscopy experiments is an overall loss of transmission. The next chapter (Harsh Environments II – Beam Steering) will thoroughly discuss the process to optimize the choice of pitching and catching lenses to accommodate severe beam steering. There is also a method presented to consider the optimal overall process based on the projected, or measured, amount of beam steering.

5.1.2 Thermal Emission

Just as molecules absorb light at specific wavelengths, they also emit photons at specific wavelengths when they transition from a higher energy state (such as if they were heated) to a lower state. Chapter 7 (Harsh Environments III – Thermal Emissions) will discuss emission in

more detail, and include several methods on how to eliminate measured emission, and how to deal with emission once it is measured.

5.1.3 Timing

Many harsh environments require sufficiently rapid measurements in order to be meaningful. Single-scan 5μs measurements using the current FDML are subject to fluctuations of the laser intensity [44]; however, averaging multiple spectra before computing temperature significantly improves both the temperature precision and absolute accuracy. The engine and shock tube are inherently unsteady, making direct averaging difficult. Phase-locked cycle-to-cycle averaging in the engine environment can be implemented; however, opportunities for averaging in the shock-tube environment are severely limited because the events are short (~1 ms) and singular (each shock takes several hours to prepare). Anticipated reductions in the intensity noise of the laser should enable high-quality single-scan (no required averaging) measurements.

5.1.4 Non-Homogeneous Conditions

When a beam travels through segregated zones which contain different gaseous conditions, such as temperature, pressure, concentration or path lengths, the beam will accumulate the spectrum as a path integration average ("line-of-sight"). For example, if a beam traveled through the 4 discrete conditions presented in Figure 5-1, it would accumulate the spectra shown in the bottom 4 panels of Figure 5-2. The resulting spectrum (top panel of Figure 5-2) is simply a summation of all of the spectral conditions. When a temperature is calculated from such a spectrum, it is generally biased cold, mostly due to the effect of number density. As an example, if the conditions were averaged using Eqn. 5.1-1, the path integrated temperature of Figure 5-1 would be 1787 K assuming ideal gas behavior, whereas the measured spectrum determines 1764 K.

$$\overline{T} = \frac{\sum_{i}^{N} T_i n_i}{\sum_{i}^{N} n_i} = \frac{\sum_{i}^{N} T_i L_i X_i}{\sum_{i}^{N} L_i X_i} = 1787K \qquad \text{Eqn. 5.1-1}$$

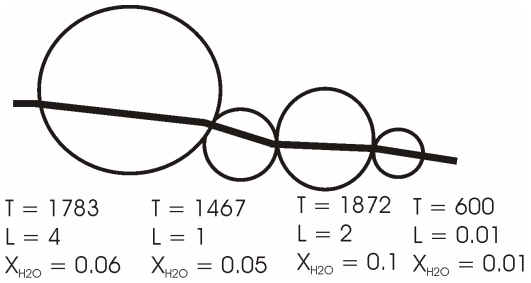

Figure 5-1 – Example of a non-homogeneous condition where $N = 4$. Notice that the beam bends depending on the angle of incident and the difference in density.

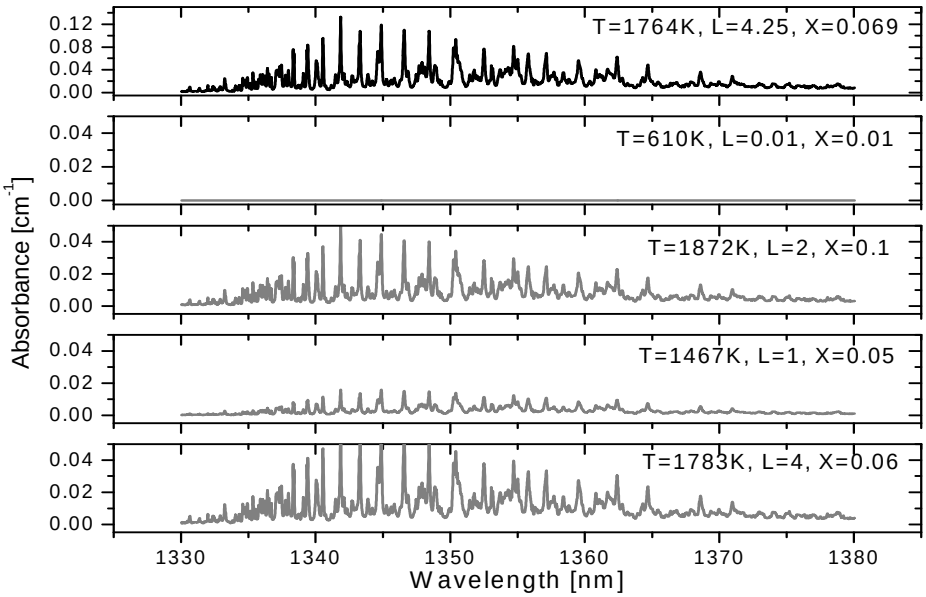

Figure 5-2 – The bottom 4 panels represent the spectra that the beam in Figure 5-1 would experience. The top panel is the summation of all the 4 spectra. The calculated temperature based on the top panel's spectrum is 1764 K.

For this reason, it is important to consider the effects of non-homogeneities on the calculations. Perhaps the environment is homogeneous throughout most of the experiment, but at other times cold boundary layers are significant. This may mean that there are areas within the experiment in which the measurements are very uncertain. One way to determine if the results will be compromised by excessive segregated zones is to have a basic understanding of the physical problem that is being studied. Most likely, wavelength-agile spectral measurements to determine temperature will not be appropriate for diesel combustion during the spray phase for example. There are simply too many separate conditions present. Another way to determine the homogeneity of the measured gas is to look at beam steering. Figure 5-1 shows that the beam will bend depending on the angle of incident and the difference in density. Roughly, the amount of beam steering can qualitatively indicate how much segregation there is. If a significant amount of beam steering is measured, the measurement may be too uncertain because of the non-homogeneity to be useful. Beam steering can be quantified by averaging the measured absorption where water does not absorb. Figure 5-3 shows one example where temperature has been calculated from absorption spectroscopy measurements in a firing HCCI engine. The shaded boxes represent areas where a significant amount of beam steering is observed. These correspond to areas in the combustion cycle which are not likely suitable for path-integration measurements. The first zone because the combustion is known to not be perfectly homogenous, the second zone because cold boundary layers are becoming more prominent.

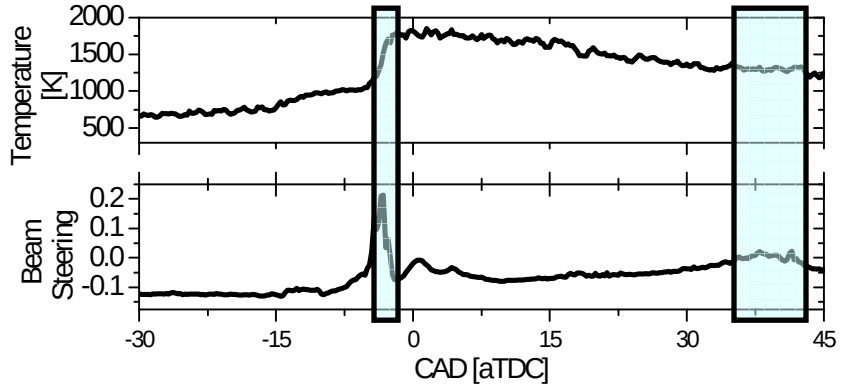

Figure 5-3 – *Top panel*: Temperature measured in a firing HCCI engine. *Bottom panel*: Beam steering as measured by an average of measured absorption taken where water does not absorb. The boxes represent areas in which beam steering is relatively high, and therefore the measurements may be too uncertain because of the non-homogeneity to be useful.

It is also not always possible to measure only the combustion zone, even if combustion is homogeneous. For example, it may be difficult to pitch and collect the light directly at the optical access windows. A typical problem is that the light must travel though a section of room air. If there is any humidity, this will compromise the results. The easiest way to avoid room air contamination is to surround the room air path of the beam with a nitrogen purge. In other cases, such as the gas turbine rig described below, there are distinct thermal zones (see Figure 5-9). If these conditions are present, it is important to either try to measure the sections separately, or make an educated guess on the temperature and water content. If that is possible, a spectrum with the proper temperature, concentration, and path length can be subtracted out of the measured spectrum. Otherwise, the measured spectra will be biased as indicated by the path integrated average.

5.2 HCCI Engine

The engine used for the HCCI studies was a GM Research “Triptane Base 4” block design with an overhead valve setup. A spacer ring with wedged sapphire windows was installed in between the block and head to gain optical access. The piston crown was recessed into the piston cap to give the combustion chamber a “double pancake” shape. Further details concerning the engine, including specifics on the coolant and lubrication systems, dynamometer, air and fuel handling systems can be found in several papers. Two documents with especially high detail are written by Younger [45] and Bright [46]. The engine was run in HCCI mode using a matrix of engine conditions. The fuel (n-heptane) was mixed with the intake air approximately 1 meter upstream of the intake valve to assure a homogeneous air-fuel mixture. The engine was run at 600 rpm, and the compression ratio was 9.6:1. Intake air was preheated and maintained at 363 K, and intake pressure was maintained at atmospheric pressure. The cylinder pressure was measured during operation with a Kistler 7063 pressure transducer and Kistler 5004 charge amplifier, calibrated with a dead weight tester. Finally, the inner diameter of the cylinder (and therefore the optical path length) was 9.5 cm.

5.2.1 Experimental Setup

An InGaAs 350MHz balanced detector (Thorlabs, PDB150C) was used, which detects 2 light signals and outputs a voltage proportional to the difference in instantaneous intensity of those signals. The FDML output was split using a 50:50 coupler; half going through the engine (I), and the other half directly to the detector (I_o). Care was taken to assure that the optical path delays for both signals were identical, therefore eliminating common-mode relative intensity noise originating from the laser itself, as well as minimizing oscilloscope bit noise. If the signal became unbalanced, for instance if the windows became dirty, or there was significant beam

steering or thermal emission, additional noise (laser noise and bit noise) would be introduced. Usually, this additional noise did not significantly affect the results, although careful balancing was always attempted for the best overall results.

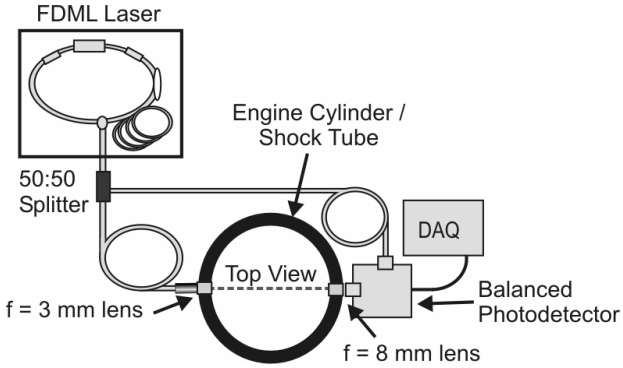

Figure 5-4 - Schematic of experimental set-up. Light from the FDML laser is split such that half travels directly to the balanced detector and the other half is pitched through the engine or the shock tube.

The light directed through the engine was emitted from a single-mode 9 μm core diameter fiber using a 3.3 mm focal length aspheric lens to collimate the beam. It was collected from the engine directly into the detector using an aspheric lens with an 8 mm focal length. These focal lengths were carefully chosen to help minimize the loss of transmission due to beam steering caused by turbulence during combustion following a published recipe [47]. The pitching fiber and lens as well as the collection lens and detector were mounted directly to the engine. A nitrogen purge was supplied to the spaces between these optics and the sapphire windows in the engine. This set-up is diagramed in Figure 5-4.

5.2.2 Specific Challenges

The specific challenges faced with obtaining absorption spectra in a firing engine are mainly timing, beam steering, and window fouling. Combustion events in the engine are repeatable on a cycle to cycle basis, but in order to track events, the acquisition must be resolved such that the combustion events are considered frozen. This is one of the fundamental reasons that the light sources were designed to scan at such a fast rate. A discussion on single cycle measurements compared to cycle-to-cycle averages will be presented in the Chapter 9 (Accuracy and Precision). Due to the rapidly changing conditions within the cylinder, varying degrees of beam steering are encountered. During interesting parts of combustion, beam steering is quite severe. The amount of thermal emissions generated during combustion wasn't insignificant, however it was manageable, as will be discussed in the Chapter 7 (Harsh Environments III – Thermal Emissions). This system allowed for a fair amount of window fouling before cleaning was required (which required the engine to be shut-down and some disassembly). For the richer conditions, the engine could be fired for over an hour before the transmitted laser signal would be noticeably reduced. Lower equivalence ratios require cleaning more often.

5.3 Shock Tube

Assessing the absolute accuracy of wavelength-agile thermometers is difficult. Initial experiments performed in the Wisconsin Shock Tube Laboratory (WiSTL) [48] aimed at assessing sensor accuracy were performed. These measurements essentially form a global check on the accuracy of the HITEMP database in the R-branch of $\nu_1 + \nu_3$ H_2O band. A Mach 2.46 shock and a Mach 1.3 shock were propagated into low pressure (97.5 kPa) air containing ambient humidity. Using gas dynamics, this allowed 4 absolute accuracy measurements (each shock included measurements of the primary shock and the reflected shock).

5.3.1 Experimental Setup

The laser was kept in a separate room, and a fiber was strung to the room with the shock tube. The InGaAs 350MHz balanced detector (Thorlabs, PDB150C) was once again used, however only one channel was utilized. Common mode noise was therefore not eliminated. The measured spectra still had an acceptable signal to noise ratio, simplifying the collection scheme, which will be discussed in Chapter 9 (Accuracy and Precision). The experimental set up was similar to that used for the engine experiments (see Figure 5-5). Spectra were measured 15 cm from the end wall of the tube, allowing measurements behind the incident as well as the reflected shock. Since the beam was pitched and collected from the same window, the path length was conveniently long, measuring 50 cm.

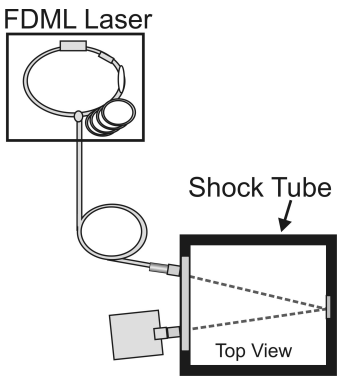

Figure 5-5 - Experimental configuration for shock tube.

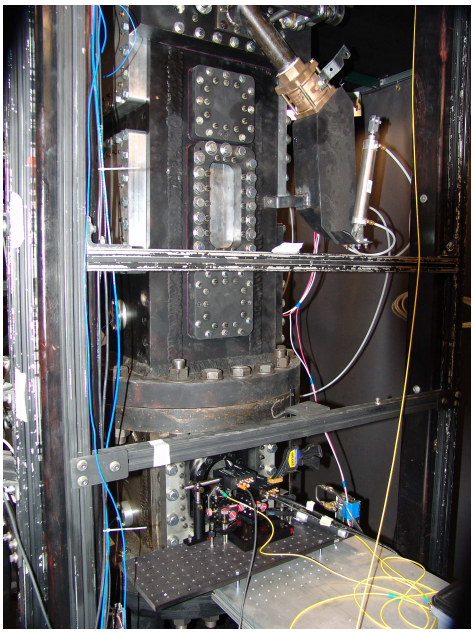

Figure 5-6 – Photograph of shock tube setup.

5.3.2 Specific Challenges

Each shock required approximately 4 hours of preparation time, and required at least 3 graduate students in the Wisconsin Shock Tube Laboratory. Because of the expensive nature of this experiment and the fact that the shock would be a singular event, it was important to obtain good spectra on the first attempt. Numerous practice runs were performed before the experiment to assure the triggering process was correct. Aside from timing, thermal emissions were detected but manageable. Beam steering was extremely severe as the shock passed. It was so severe that no light aside from the thermal emission was detected. Once the shock had passed however, little beam steering was observed.

5.4 Gas Turbine Combustor

Gas-temperature measurements in the combustion zone of a gas-turbine-combustor sector rig installed in the AFRL High-Pressure Combustor-Research Facility located at Wright-Patterson

Air Force Base were made using wavelength-agile absorption spectroscopy. The High-Pressure Combustor-Research Facility (HPCRF) at Wright-Patterson Air Force Base (WBAFP) was designed for the experimental exploration of advanced combustor concepts under conditions simulating actual gas-turbine-engine operation. The facility can accommodate a range of test articles from single-cup test rigs to multi-dome 60-degree combustor sectors. It comprises two separate flow-paths that provide air to either a sector combustor test article or a single-nozzle combustor as shown in Figure 5-7. The sector leg is designed for combustor pressures from 13 kPa to 2200 kPa, with inlet air temperatures to 922 K and air flows to 11 kg/s. The main combustion air fed to the facility is provided by two Ingersoll-Rand centrifugal-type air compressors, which can produce 7.7 kg/s airflow at 5100 kPa each for a total air-flow capability of 15.4 kg/s. The test-rig cross section is shown in Figure 5-8.

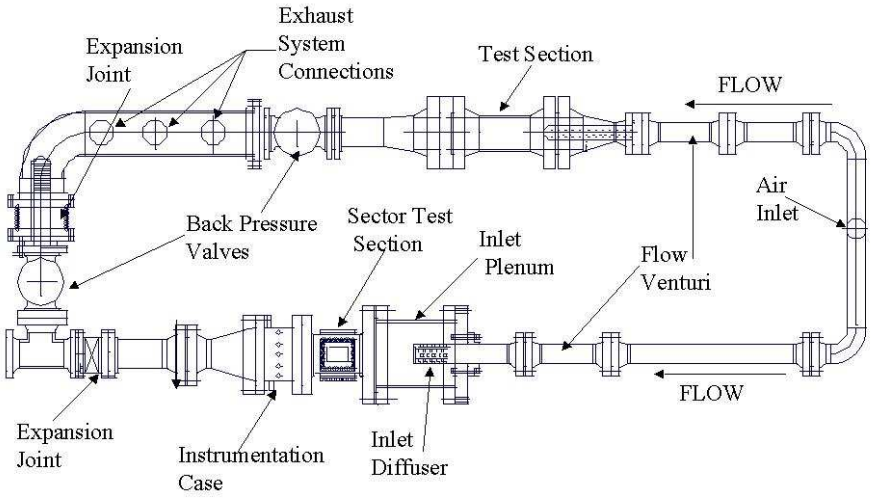

Figure 5-7: High-Pressure Combustor-Research Facility at WPAFB.

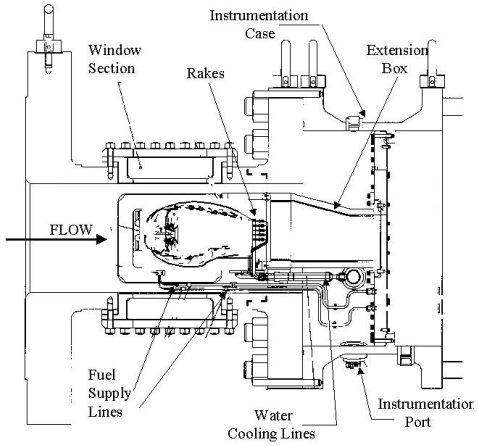

Figure 5-8: HPCRF test-rig cross section.

5.4.1 Experimental Setup

Figure 5-9 diagrams the overall setup used to obtain H_2O absorption spectra. The launching and collecting lenses were chosen to reduce the amount of light lost due to beam steering (light deviating from the intended path due to index-of-refraction gradients, generally caused by turbulent boundaries) [47]. A neutral-density (ND) filter (optical density = 0.9) and iris were used to limit collection of thermal emission. For simplicity, spectral filtering was not used to further limit thermal emission. This choice was based in part on previous experience. In most previous experiments in which, hot H_2O vapor was the dominant source of thermal emission. In these cases, spectral filtering is not particularly helpful, because the sensor is designed to monitor the entire R-branch of the H_2O band. Thus, the ideal spectral filter will reject the P-branch and thereby reduce the measurement background by only a factor of approximately two. However, in this test rig, significant broadband thermal emission from solids contributes, and in hindsight, spectral filtering would have been very helpful.

The photo detector was chosen to balance effects of beam steering (demanding larger collection area), as well as thermal emission and response time (both of which demand smaller collection area). The minimum required bandwidth to measure H_2O lines at atmospheric pressure with the 200-kHz-scanning-frequency FDML laser is approximately 500 MHz. A Thorlabs (PDB150C), 350-MHz, 0.3-mm-diameter InGaAs detector was chosen as a suitable compromise among the many constraints.

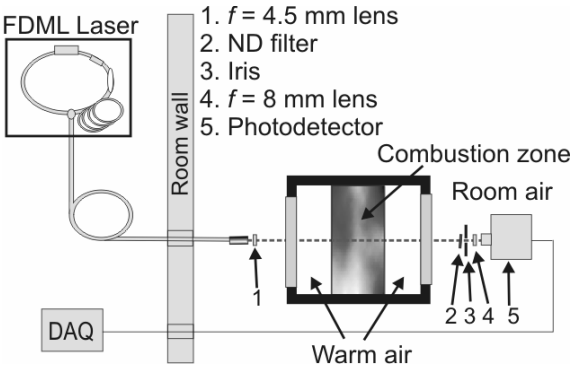

Figure 5-9 - Experimental configuration for gas turbine rig. The laser and data acquisition system were located in an adjacent room.

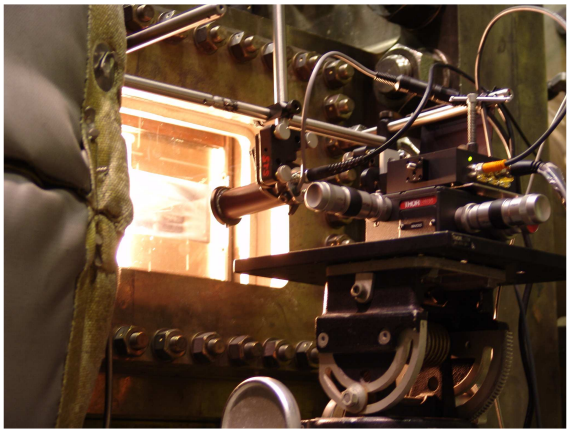

Figure 5-10 – Photograph of light collection scheme for the gas turbine rig.

5.4.2 Specific Challenges

The gas-turbine-combustor sector rig is relatively steady and continuous, allowing for straightforward averaging. 1000 scans were averaged for each data point at each condition. Beam steering was noticeable, both because of the large path length spanning a highly turbulent region, as we as the heavy spatial filtering (iris) and small detector (see Figure 5-9). The beam steering was however manageable. The main challenge was the generated thermal emissions. The emission observed in the gas-turbine-combustor test was significantly higher than levels observed in piston engine and shock tube, even at similar values of measured gas temperature. Soot created during combustion, deposits accumulated on the windows, emission from the windows themselves, and the possibility that the detector can view other hot surfaces such as combustor walls can all contribute to the relatively high emission. While collecting H_2O absorption spectra, we simultaneously recorded emission spectra with an optical spectrum analyzer (OSA). These spectra showed significant broadband emission, completely overpowering any H_2O emission features, implying substantial emission from sources such as those mentioned above.

To deal with the emission, both a neutral density (ND) filter and an iris were used to reject emission while retaining sufficient signal, even in the presence of beam steering. A detector with a small active area (diameter = 0.3 mm) was also chosen to reduce the collection of emission. The optical beam path was placed 6 cm downstream from the hottest (most strongly emitting) section. As with the HCCI engine and the shock tube, the detector voltage measured when the laser was briefly turned off at the start of each scan was subtracted from the measured signal. Figure 5-10 shows the extent of the visible emissions.

The final significant difference between this experimental environment and previously successful experiments is the existence of absorbing H_2O outside the combustion region of interest (as can be seen in Figure 5-9, see "Combustion zone," "Warm air," and "Room air"). In the turbine experiment, three distinct conditions exist along the laser line of sight: the room air, the warm air, and the combustion zone. In addition to these primary sections, thermal boundary regions at each window surface contribute to uncertainties in the measurements. The warm air (on either side of the combustion area) is expected to have sufficiently low H_2O mole fraction to have impact on these measurements; therefore, we ignored this section in our calculations. Room-air corrections were accomplished. Direct fiber coupling to the combustor in future measurements will address these concerns.

5.5 Conclusions

It does not matter if one has the world's best wavelength-agile laser and a perfect system to calculate temperature if experimental conditions are not taken into account when measurements are performed. In this chapter, various considerations concerning absorption spectrum measurements specifically in harsh, combusting environments were presented. The methods for dealing with those conditions were presented for three systems, the HCCI engine, a shock tube, and a gas turbine rig.

6 Harsh Environments II: Beam Steering

This chapter expands on the previous chapter's explanation of the phenomenon of beam steering, and offers a method for minimizing the sensitivity of transmission-based sensors to beam steering without quantitative prediction of the severity of the beam steering field. This can therefore lead to improvements in either spectral resolution or response time.

6.1 Introduction

Lasers and laser-like sources such as broadband superluminescent devices have become an important part of many measurement techniques due in large part to recent advancements in photonic technologies. These improvements include increased optical power, coverage of more wavelengths, and increased convenience (e.g., through fiber optics). Laser light can be used to measure temperature [22], composition [49], pressure [50], and velocity [51] of gases non-intrusively via absorption spectroscopy, a method especially useful in harsh environments such as internal combustion or turbine engines. In order to maximize the potential in practical applications, issues arising from beam steering – the wander and/or diffusion of laser light due to refractive index gradients – must be understood. Certain experimental configurations such as wavelength-agile spectroscopy [27], wavelength-modulation spectroscopy, and FM spectroscopy [52] are often able to accommodate a limited amount of beam steering, but all configurations will suffer to some degree when encountered with beam steering (generally a simple loss of intensity makes measurements more difficult and less precise).

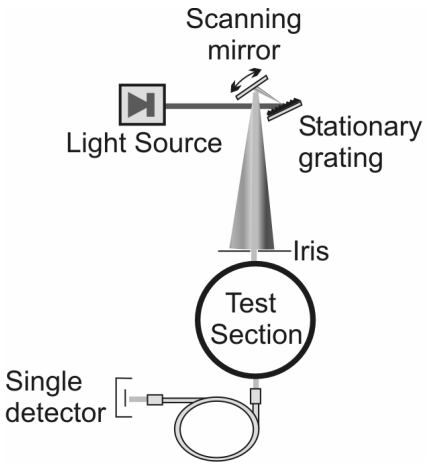

Figure 6-1 – “Scanner” - Wavelength-agile absorption spectroscopy schematic.

Figure 6-1 diagrams a scanning wavelength absorption spectroscopy setup (“scanner”) which has been used to measure gas temperature in a piston engine [27]. A broadband light source is aimed at a diffraction grating which in turn disperses the light according to wavelength. An oscillating mirror directs the dispersed light through an iris into the test section, so that the transmitted light is a continuous scan of wavelengths. The scanning wavelength source is then pitched into the engine, and a single detector is used to measure the intensity of the transmitted light.

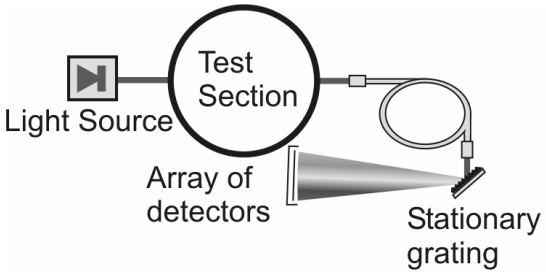

Figure 6-2 – “OMA” – Optical Multichannel Analyzer - absorption spectroscopy schematic.

Figure 6-2 shows another basic option for absorption spectroscopy, using the same design found in commercial optical multichannel analyzers (OMAs). A broadband light source is aimed directly through the test section. A diffraction grating chromatically disperses the light transmitted through the test section, and an array of detectors is used to measure the transmission spectrum.

These two basic examples can be used to illustrate the importance of understanding the beam steering in an experiment. When the amount of beam steering is negligible, the OMA technique will always be superior because of its inherently better transmission (the iris in the scanner setup discards most of the light, whereas no light is thrown away in the OMA setup). Increased amounts of beam steering can reduce the intensity of the transmitted light in the scanning configuration (Figure 6-1), but with appropriate light collection techniques (a large fiber and detector) this reduction can often be minor. The OMA method (Figure 6-2) is often impacted more severely by beam steering. Since the extent of the exiting light is increased by beam steering, the spectral resolution of the OMA is compromised. This is because the diffraction grating in the OMA differentiates colors by diffracting them at different angles, and there is less differentiation when the light incident on the diffraction grating already encompasses many angles. A small collection fiber or slit could be used to preserve the spectral resolution of the OMA, but only at the cost of reduced transmission through the test section due to beam steering. When the beam steering is severe and high spectral resolution is required, the scanner technique prevails for this reason. Thus, the spectroscopist must understand beam steering and its effects on such experiments in order to choose the best optical setup.

In this chapter a framework for optimizing the design of the experimental setup without requiring *a priori* knowledge of the beam steering field is developed. The general framework should be useful to those designing absorption-based sensors and might also be valuable in other optical analyses, such as laser induced fluorescence.

6.2 Beam Steering Background

In order to determine the optimum experimental configuration for absorption spectroscopy, this chapter begins with a basic discussion and theoretical model of beam steering. A review of the concept of optical extent is then presented because it is useful for characterizing beam steering and its effects on optical experiments.

6.2.1 Beam Steering Overview

In this chapter, beam steering is defined as the deviation of light from its intended path due to propagation through a field of non-uniform refractive index: typical applications of interest are shock tubes [53] or internal-combustion engines [28]. Beam steering has been studied in great detail in the aerospace sciences, and is referred to in those contexts as aero-optics [54]. Aero-optics generally deals with atmospheric studies, for example transmission of laser beams through turbulent boundary layers on aerodynamic surfaces. The goal of aero-optics is often to develop an adaptive optic scheme to correct beam steering (reproducing a collimated beam), a more ambitious goal than simply managing beam steering as attempted in this paper. The preferred approach in aero-optics is wavefront tracking. In gasdynamic experiments, we expect a ray-tracing approach to be sufficient, and adopt ray-tracing rather than wavefront tracking for the remainder of this paper. Optical design in beam steering environments, even when the goal is simply improved transmission, is a potentially vast topic. This chapter only scratches the

surface, essentially applying previous studies to a specific experimental configuration. As noted below, several assumptions are made which may be inappropriate in certain experiments.

Changes in refractive index (Δn) bend light at different angles, and cause the light wandering effect seen in beam steering. Toward understanding how these changes come about, a review for calculation of refractive indices of gases is presented. Wavelength-dependent refractive index values for gases at standard temperature and pressure (STP) can be found in the literature [55]. Such data are useful for evaluating effects of gas composition, as in combustion events, on refractive index. As an example, pure butane vapor at standard atmospheric conditions has a refractive index of 1.00139 compared to air at 1.00027 [55]; consequently, flows in which butane and air are made to mix are useful for simulating beam steering in laboratory setups. For fully-mixed gases, the mole-fraction-weighted average of the composite values will give a mixture refractive index at STP [56]. The refractive index of the gas mixture at higher temperatures and pressures can then be estimated using the following equation:

$$(n_o - 1) = (n_{STP} - 1)\frac{\rho_o}{\rho_{STP}} \qquad 6.2\text{-}1$$

Where n_o stands for the refractive index at some desired condition and ρ_o stands for the gas density at that condition. Note that 6.2-1 is not exact because it ignores the temperature dependence of internal energy level populations within the gas.

Now consider a gas of uniform mixture composition but nonuniform refractive index owing to temperature or pressure nonuniformities. If n_o is defined as the average refractive index, the deviations Δn about n_o also scale directly with deviations in density ($\Delta\rho$) according to 6.2-2:

$$\Delta n = (n_o - 1)\frac{\Delta\rho}{\rho_o} \qquad 6.2\text{-}2$$

Consider n_o as an average over some volume, and Δn to be the local deviation from n_o in that volume. Therefore, for nonzero Δn, a collimated laser beam projected through the volume stands to emerge with increased size and divergence.

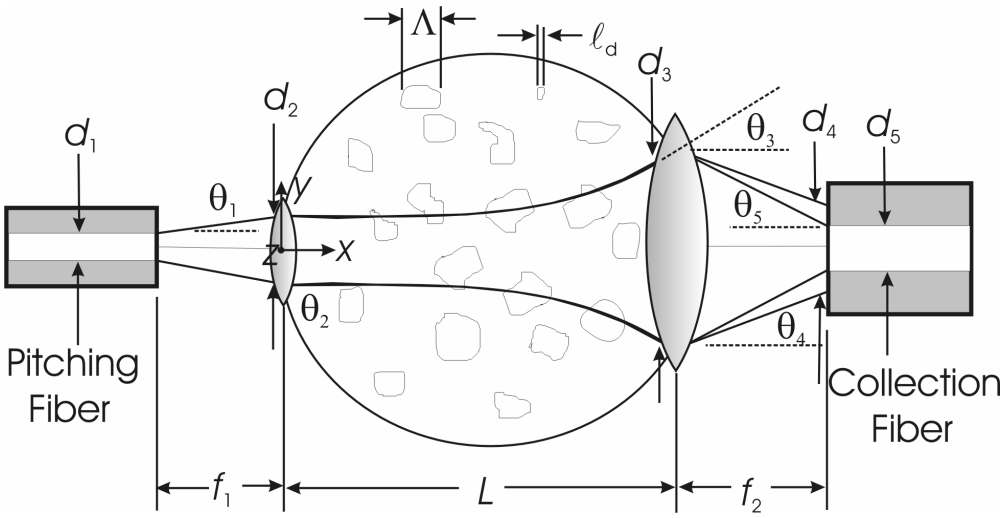

Figure 6-3 - Schematic for line-of-sight optical access to a turbulent fluid flow test section of length L, with the integral length scale Λ, and Kolmogorov length scale ℓ_d.

Figure 6-3 outlines the treatment of beam steering throughout most of this chapter. Laser light enters a test section of fixed geometry from an input fiber with a core diameter d_1 and acceptance half angle θ_1. The light passes through a pitching lens with a focal length of f_1, collimating the light to a diameter d_2 and divergence angle θ_2. By placing the fiber in the focal plane of the lens, the input is collimated such that θ_2 is very small. Beam steering in the turbulent medium can cause the light to expand as shown. Light is collected by a lens with focal length f_2 and focused onto a collection fiber with a core diameter d_5 and acceptance half angle θ_5 positioned f_2 from the

collection lens. The goal is to collect as much light as possible into this collection fiber. The lenses in Figure 6-3 are specified by their diameter and focal length. The actual lens diameters are somewhat flexible: lenses larger than the local size of the light beam (specified by d_2 and d_3) will suffice. The focal lengths depend on several factors. The focal length of the pitching lens (f_1) can be calculated by geometry:

$$f_1 = \frac{d_2 - d_1}{2\tan(\theta_1)} \qquad 6.2\text{-}3$$

If the focal length of the collection satisfies:

$$f_2 = \frac{d_5}{2\tan(\theta_3)} \qquad 6.2\text{-}4$$

then all light focused by the collection lens will strike the core of the collection fiber. d_4 and θ_4 represent the size and angle of transmitted light incident on the collection fiber. d_4 and θ_4 as shown in the figure result in less than 100% transmission because the fiber is overfilled.

The fractional transmission (T) is a ratio of the area and acceptance angle that the collection fiber can collect to the area and collection angle that is actually produced by the collection lens. Since both area and acceptance angle of the fiber are relevant, three cases of transmission can be envisioned (^ represents the Boolean 'and'):

$$\begin{aligned} T &= \frac{d_5^2 \sin^2(\theta_5)}{d_4^2 \sin^2(\theta_4)} \{d_5 \le d_4 \wedge \theta_5 \le \theta_4\} \\ T &= \frac{d_5^2}{d_4^2} \{d_5 \le d_4 \wedge \theta_5 > \theta_4\} \\ T &= \frac{\sin^2(\theta_5)}{\sin^2(\theta_4)} \{d_5 > d_4 \wedge \theta_5 \le \theta_4\} \end{aligned} \qquad 6.3\text{-}3$$

In the absence of beam steering, the output diameter and divergence angle (d_3, θ_3) can be determined from raytracing (diffraction effects can be included if necessary). Without beam steering in the test section, the output diameter d_3 would be only slightly larger than d_2, and θ_3 would be essentially unchanged. The situation changes when a nonuniform refractive index field is present in the test section. In this case, the beam can spread out or diffuse, primarily because of small-scale steering structures. The beam can also wander – emerge with a new mean position and mean pointing angle – owing to larger-scale steering structures. In practice, a transmitted beam experiences both diffusion and wander. Furthermore, the nonuniform refractive index field is typically fluctuating in time, so that the diffusion and wander are time-varying as well. The time-average of the diffusion alone will behave in a way similar to the instantaneous diffusion. Assuming the wander is isotropic, the time-average of the wander will also behave as diffusion. This is the case we treat in this paper – pure diffusion – and we expect that our approach will perform well, to first-order, in many experimental configurations. Large-scale steering structures often steer the beam in a preferred direction [57] and thus the wander does not average away to a pure diffusion. In such cases, our treatment might be combined with a raytracing-based treatment of the bulk beam steering effects.

The final result for the diffusion treated here – whether it is from average isotropic wander, instantaneous diffusion, or average diffusion – is that light exiting the test section will have a significantly larger effective diameter (d_3) and divergence angle (θ_3) due to beam steering. Further mentions of averages throughout the paper will imply spatial averages, although interpretation as time averages and time/space averages may be appropriate as well.

6.2.2 Beam Steering Model

For simplicity, the beam steering was modeled as a diffusion of light through the test section. Much more detailed methods for modeling of beam steering exist [54]. In this chapter, the beam steering model used the approach derived by Sutton [58]. Sutton used Snell's law and geometric optics to describe the rate of change of the diffusing angle as equal to the normal gradient of the refractive index, as in:

$$\frac{d\theta}{ds} = \nabla n \tag{6.2-5}$$

where ds is a differential length along the light path, and $d\theta$ is a differential diffusion angle. If the change in the path length is assumed to be significant in only the traversing direction ($s \approx$ the x-coordinate of Figure 6-3), then 6.2-5 can be written as:

$$\frac{\partial \theta_y}{\partial x} = \frac{\partial n}{\partial y}; \frac{\partial \theta_z}{\partial x} = \frac{\partial n}{\partial z} \tag{6.2-6}$$

For small changes in z and y, the mean-squared scattering angle $\left\langle \Delta\theta_y{}^2 \right\rangle$ is some function of the mean-squared local refractive index deviations $\left\langle \Delta n^2 \right\rangle$ (symbolized here by K) and distance that the light has traveled [58]:

$$\left\langle \Delta\theta_y{}^2 \right\rangle = \left\langle \Delta\theta_z{}^2 \right\rangle = \mathrm{K}x \tag{6.2-7}$$

K is defined as the "beam steering coefficient", a measure of the severity of the refractive index variations in a flow from the perspective of a transmitted laser beam. Sutton's model of K for a homogeneous, isotropic turbulent flow (Re > 100) with turbulent integral length scale Λ, Kolmogorov length scale ℓ_d (refer to Figure 6-3), and mean-square deviations in the refractive index $\left\langle \Delta n^2 \right\rangle$ is given as:

$$\mathrm{K} = \frac{3.8\left\langle \Delta n^2 \right\rangle}{\Lambda}\left(\frac{\Lambda}{\ell_d}\right)^{1/3} \qquad 6.2\text{-}8$$

Often a flow's characteristics are not sufficiently well-known to obtain a reliable estimate of K from Eqn. 6.2-8, but order-of-magnitude estimates are usually possible. For example, in the piston engine application, literature values are used for typical turbulent length scales in internal combustion engines, Λ = 2 mm and ℓ_d = 0.1 mm [59], along with an estimated $\left\langle \Delta n^2 \right\rangle$ of 0.1% to calculate a K of ~ 0.0001 m^{-1} using Eqn. 6.2-8. Later, approximate measurements of K ('K_{meas}' - discussed in Section 6.3.1) revealed a K_{meas} of ~ 0.0004 m^{-1} in a piston engine near top dead center (TDC). Throughout this chapter, when beam steering behavior is simulated and requires a K value, the measured value is used. However, simulations based on calculated K still provided useful information. Fortunately, a large portion of the optical design strategies presented here require neither calculated nor measured K values. For example, a two-fiber transmission system like the one shown in Figure 6-3 can be optimized for minimum sensitivity to beam steering without any estimate of K at all, as we discuss below.

For simplicity, we approximate the maximum divergence angle of a transmitted laser beam (in radians) as:

$$\Delta\theta_{\max} \approx \sqrt{\left\langle \Delta\theta^2 \right\rangle} = \sqrt{\mathrm{K}x} \qquad 6.2\text{-}9$$

where $\Delta\theta_{\max}$ is essentially the root mean squared 'average' of the divergence angle, and as mentioned above it could refer to either temporal, spatial, or combined averages. The maximum angle of the light anywhere in the beam steering field, θ, is therefore simply:

$$\theta \approx \theta_2 + \Delta\theta_{\max} = \theta_2 + \sqrt{\mathrm{K}x} \qquad 6.2\text{-}10$$

where θ_2 is the input angle of the light (see Figure 6-3). The diameter d of the light anywhere in the beam steering field is also of interest. Geometry shows that for small angles:

$$\frac{d}{dx}(d) = 2\theta \qquad 6.2\text{-}11$$

Substituting in 6.2-10 into this equation, separating variables, and integrating gives (with regard to Figure 6-3):

$$d = d_2 + 2\left[\theta_2 x + \sqrt{\mathrm{K}}\left(\frac{2}{3}x^{1.5}\right)\right] \qquad 6.2\text{-}12$$

Eqs. 6.2-10 and 6.2-12 are important because they show how d and θ grow together in a beam steering field as a function of x. d_3 and θ_3 can be calculated by substituting the test section length (L) in for x. For reference, Figure 6-4 shows how beam diameter d and dispersion angle θ change throughout a representative flow field. Figure 6-4 was generated using $\mathrm{K}_{\mathrm{meas}}$, a pitching lens with a 4.5 mm focal length, and a single mode 9μm, 0.09 NA pitching fiber. The speed of the growth depends on K, but the form of the growth does not; the angular growth due to beam steering behaves like $x^{1/2}$ and the diameter growth due to beamsteering behaves like $x^{3/2}$, so that the diameter always grows like the cube of the angle. This fact ultimately enables the optical designer to optimize a system for minimum sensitivity to beam steering without actually quantifying K.

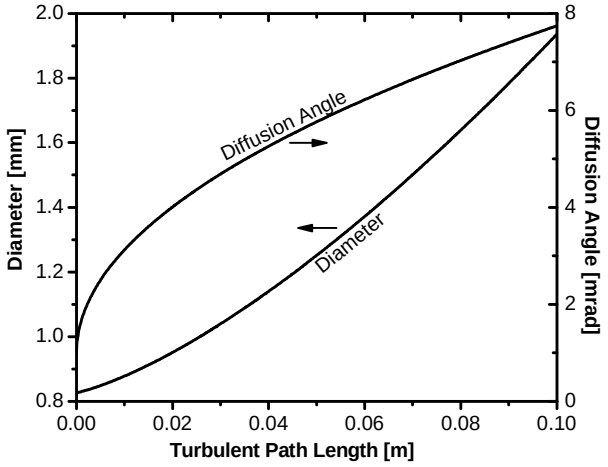

Figure 6-4 – Diameter and divergence angle of laser light as a function of distance through a turbulent flow field. Assumptions: K = K_{meas}, f_1 = 4.5 mm, 9μm diameter, 0.09 NA pitching fiber.

In this simplified model of beam steering, a homogeneous spreading of the light as it travels through the turbulent field is assumed. In particular, it assumes that along any line dissecting the light beam at a right angle to the propagation direction, individual photons have divergence angles θ that are uniformly distributed over $\pm\Delta\theta_{max}$. In practice, photons near the edge of the beam are expected to have higher angles and photons near the center to have smaller angles, but uniform distribution is assumed for simplicity in this chapter. Note that the assumption is particularly crude for beams entering the test section with large values of θ_2.

6.2.3 Extent

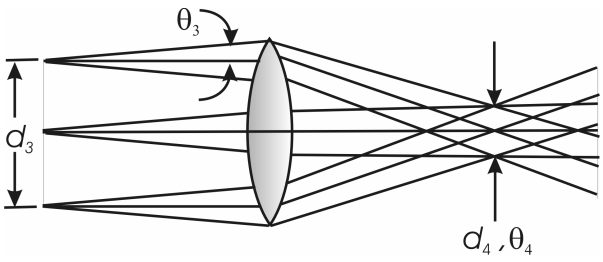

Figure 6-5 - Example of optical extent conservation. The lens can reduce the diameter of the light (from d_3 to d_4), at the expense of the dispersion expansion half angle (from θ_3 to θ_4).

The concept of optical extent (also called etendue, Lagrange Invariant, beam parameter product, or beam quality, heretofore referred to as 'extent') is particularly useful for analyzing beam steering. Extent is covered in many optics texts [56, 60-62]; here a treatment formerly presented in Applied Optics [63] is followed. Extent may be defined at any position in an optical system as a product of the square of the spatial and angular parameters of the light at that position. In optics, it is common for the sine of the half angle (θ) to be referred to as the numerical aperture (NA). Therefore,

$$Extent \equiv 2\pi^2 d^2 \sin^2(\theta) = 2\pi^2 d^2 NA^2 \qquad 6.2\text{-}13$$

Figure 6-5 details how extent is conserved in a simple ray trace. Starting with a given diameter (d_3, to follow the scheme in Figure 6-3) and divergence angle (θ_3), a lens can transform light to d_4 and θ_4 while conserving extent. At best, extent is conserved as light passes through an optical system. Non-ideal effects such as lens aberrations, vibrations, and scattering from imperfect surfaces or dust tend to increase the extent as light propagates. Beam steering can drastically increase extent, as is shown in this chapter.

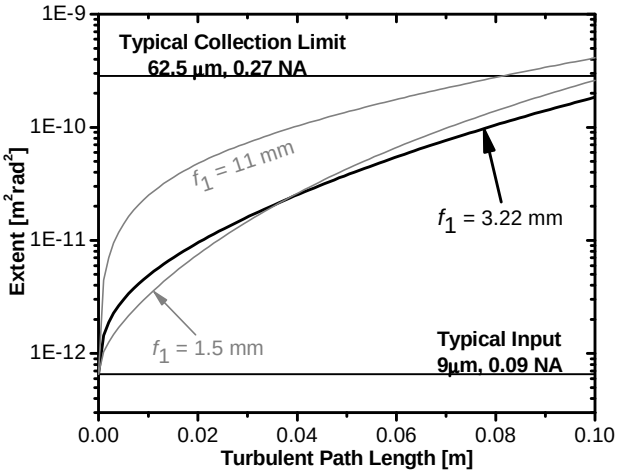

Figure 6-6 – Growth of optical extent in a turbulent flow field. Extent values set by common fibers are shown. Assumptions: K = K_{meas}, 9 µm diameter, 0.09 NA pitching fiber.

The extent of the beam can be calculated using the following equation (combining 6.2-10, 6.2-12, and 6.2-13, and using the small angle approximation):

$$Extent = 2\pi^2\left[\left(d_2 + 2\theta_2 x + \frac{4}{3}\sqrt{\mathrm{K}}x^{3/2}\right)\left(\theta_2 + \sqrt{\mathrm{K}x}\right)\right]^2 \qquad 6.2\text{-}14a$$

$$Extent = 2\pi^2\left\{\left[d_1\left(1+\frac{x}{f_1}\right) + 2f_1\theta_1 + \frac{4}{3}\sqrt{\mathrm{K}}x^{3/2}\right]\left[\frac{d_1}{2f_1} + \sqrt{\mathrm{K}x}\right]\right\}^2 \qquad 6.2\text{-}14b$$

Eq. 6.2-14a shows that the way in which extent grows depends on both d_2 and θ_2, which are both determined from the pitching fiber and lens. Eq. 6.2-14b uses the focal length of the lens rather than d_2 and θ_2. In this equation then, the only unknowns are K and f_1 assuming the pitching fiber is known (d_1, θ_1). Note that for $x = 0$ (at the input to the turbulent field), the extent will always be $(d_2\theta_2)^2$, within the small-angle approximation. Figure 6-6 shows how extent increases

throughout the turbulent field using K_{meas} as described above. Common input and collection extent limits from standard optical fibers are also shown for reference. These limits are based on a typical single mode fiber (9 μm, 0.09 NA – both on a $1/e^2$ basis) for an input fiber and a multimode 62.5 μm, 0.27 NA collection fiber. Three extent growth curves are shown; the only difference between these curves is the focal length of the pitching lens used. By necessity, all three start (at $x = 0$) with an extent equal to that of the pitching fiber, and grow from there. After propagating through a turbulent medium of length x, the optical designer would like the extent of the output beam to be smaller than the extent of the collection fiber. In this case, 100% transmission is possible. For example, the f_1 = 11 mm pitching lens allows 100% transmission into the 62.5 μm fiber for $x < \sim 0.08$ m; at further distances, transmission will be sacrificed.

6.3 Experimental design to accommodate beam steering

Considering the ubiquity of beam steering issues in high temperature, high pressure, and unsteady environments, a relatively small body of work has been published addressing optimization of experimental parameters in order to accommodate the effects of beam steering in transmission measurements [22, 53, 64-67]. In this section, a method to design a light collection scheme optimized for maximum toleration of beam steering is presented. This design process does not require knowledge of the K factor discussed in Eq. 6.2-7.

6.3.1 Lens Optimization

The primary effect of beam steering on transmission measurements is that the emerging beam may not be fully collected by a photodetector or fiber positioned at the output; with this paper we hope to make strides toward a detailed understanding of this problem. A well-designed light collection scheme can compensate for a limited amount of beam steering. This section assumes

that the experiment is set up as in Figure 6-3, where lenses are placed one focal length away from fibers at the edges of the turbulent medium (one pitching fiber, one collection fiber). The source light could also be a free-space beam, which could be collected into a free-space detector without changing the methodology we present in this paper. Fibers were chosen here because of their experimental convenience as well as their convenient definitions of size and acceptance angle.

Clearly, choosing the largest collection fiber accommodates the most beam steering. However, large fibers may not be acceptable. For example, in the scanner configuration, a high speed (and consequently small area) detector is often required, limiting the size of the collection fiber. For reference, Table 6-1 lists some commercial photoreceivers and shows the relationship between time response and collection area. For the OMA method, large fibers typically result in poor spectral resolution. For example, commercial optical spectrum analyzers (e.g., Ando model #AQ-6315A/B) have spectral resolutions that behave approximately as:

$$d\lambda = d_5\left(6.2E-6\right) \tag{6.3-1}$$

In 6.3-1, $d\lambda$ is the spectral resolution and d_5 is the core fiber diameter at the input to the optical spectrum analyzer ($d\lambda$ and d_5 must have identical SI units).

Manufacturer	Part #	Size	Time Response
New Focus	2317	5 mm (dia)	796 ns (estimated)
ThorLabs	PDA255	1x1 mm^2	3.2 ns (estimated)
New Focus	1592	0.0625 mm (dia)	115 ps
Hamamatsu	G7096	0.2 x 0.2 mm^2	40 ps (rise), 120 ps (fall)

Table 6-1 - Sample commercial photodetectors (InGaAs: appropriate for detection of ~ 900 – 1650 nm wavelengths)

The collection fiber NA (NA = sin (θ_5)) is also relevant to its effective "size". The maximum acceptance angle (or NA) can be set by the NA of available fibers, the reflectivity of the photodetector surface as a function of incidence angle, or the size of the optics in the OMA. In any case, the design process typically begins with finding the maximum collection fiber size (diameter and NA) that can be accommodated by the OMA or detector used. The maximum extent of the collection scheme is then readily calculated (Eq. 6.2-13). The experimental designer can work from this known constraint on collection extent backwards to design the optical system.

Returning to Figure 6-6, short focal length pitching lenses are best for short turbulent paths (of the three cases shown, the f_1 = 1.5 mm pitching lens gives the lowest extent in the first ~ 0.03 m). Long focal length pitching lenses are preferred for longer turbulent paths. One can then take the derivative of *Extent* with respect to f_1 (from Eq. 2-14b), set it equal to zero, and subsequently determine the optimal pitching lens for a particular test section length and K. Equation 6.3-2 represents the resulting equation (using the small-angle approximation) which is used to calculate an optimum pitching lens:

$$0 = \left(\frac{d_1^2 L}{f_1^3} + \frac{5 L d_1 \sqrt{\mathrm{K}L}}{3 f_1^2} - 2\theta_1 \sqrt{\mathrm{K}L} \right) \qquad 6.3\text{-}2$$

Using this equation, only pitching fiber properties (d_1, θ_1), test section length (L), and K are required for finding f_1, and Eq. 6.2-3 can then be used to determine d_2. For a 10 cm test section, with the measured 0.00042 m^{-1} K value, the optimal pitching lens has a focal length of 3.2 mm, and at least a diameter of 0.59 mm (assuming a 9 μm, 0.09 NA pitching fiber). A pitching lens with any focal length other than 3.2 mm will produce light with a larger extent at x = 0.1 m. With the optimal f_1 = 3.2 mm pitching lens, the turbulent field represented in Figure 6-4 produces light that can be collected into a fiber slightly smaller than the 62.5 μm, 0.27 NA fiber shown, in fact at x = 0.1 m, Figure 6-6 determines that it can be collected into a 50.3 μm, 0.27 NA fiber. This results in a spectral resolution of 0.312 nm in the OMA method (Eq. 6.3-1) compared to 0.388 nm with the 62.5 μm, 0.27 NA fiber. This marks a 24% improvement in spectral resolution due to careful lens selection.

Now assume that a pitching fiber and a collection fiber have been chosen and the test section has a known fixed length (L). Using this information, the ideal pitching and catching lens parameters (f_1, d_2, and f_2, d_3) can be determined using equations found throughout this chapter, summarized in Table 6-2.

Equation		Unknowns
$f_1 = \frac{d_2 - d_1}{2\tan(\theta_1)}$	(6.2-3)	f_1
$d_1^2\theta_1^2 = d_2^2\theta_2^2$	(6.2-13)	d_2
$f_2 = \frac{d_5}{2\tan(\theta_3)}$	(6.2-4)	θ_2
$d_5^2\theta_5^2 = \left\{\left[d_1\left(1+\frac{L}{f_1}\right) + 2f_1\theta_1 + \frac{4}{3}L^{3/2}\sqrt{\mathrm{K}}\right]\left[\frac{d_1}{2f_1} + \sqrt{\mathrm{K}L}\right]\right\}^2$	(6.2-14b)	d_3
$d_3 = d_2 + 2\left[\theta_2 L + \sqrt{\mathrm{K}}\left(\frac{2}{3}L^{1.5}\right)\right]$	(6.2-12)	θ_3
$\theta_3 = \theta_2 + \sqrt{\mathrm{K}L}$	(6.2-10)	K
$0 = \left(\frac{d_1^2 L}{f_1^3} + \frac{5Ld_1\sqrt{\mathrm{K}L}}{3f_1^2} - 2\theta_1\sqrt{\mathrm{K}L}\right)$	(6.3-2)	f_2

Table 6-2 - Assuming a known pitching fiber (d_1, θ_1), a known collection fiber (d_5, θ_5), and test section length (L), the problem can be reduced to 7 equations and 7 unknowns.

The solution from Table 6-2 is based on finding the maximum K that can be tolerated without loss of signal (hereafter called $\mathrm{K}_{\max}$) by setting the extent at $x = L$ equal to the collection fiber extent (Eq. 2-14). Note that in practice, the actual K in the flow might be bigger or smaller than this $\mathrm{K}_{\max}$, and in particular is probably not known *a priori*. That fact, however, does not affect $\mathrm{K}_{\max}$. $\mathrm{K}_{\max}$ is still the largest K that can be tolerated without loss of signal. If, in practice, the beam steering is weaker than given by $\mathrm{K}_{\max}$, no light will be lost due to beam steering. If the beam steering is stronger than given by $\mathrm{K}_{\max}$, throughput will be sacrificed. This optimum solution can also be thought of as minimizing the generated extent to the system.

The diameter and focal lengths of the pitching and collecting lenses from the solution of Table 6-2 are the best set possible for accommodation of beam steering. This does not mean the lenses can manage arbitrary amounts of beam steering, only that they are the best choices for the chosen fibers. In an experiment, the actual K may of course be greater than K_{max}. However, it is not possible to redesign the lens system for the actual $K (> K_{max})$ and yield any increase in throughput (this is due to the fixed extent of the pitching and collection fibers). Thus, our approach is to design for K_{max} and consider the optical system to be optimized within the constraints of the experiment.

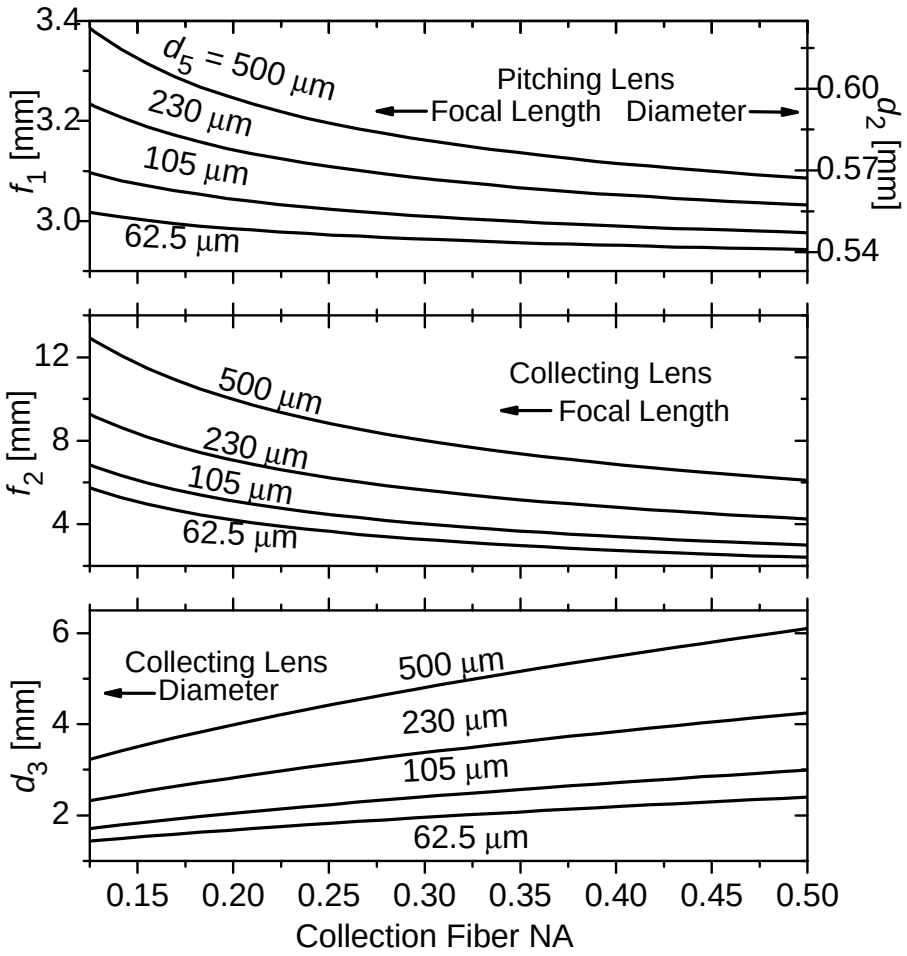

Figure 6-7– Optimum pitching and collection lens selection map. Assumptions: 9μm diameter, 0.09 NA, L = 10 cm.

An optimum lens selection map was developed as the calculations (from Table 6-2) were repeated for common fiber diameters over a range of NAs as shown in Figure 6-7. These figures might be directly useful to the optical designer; however, because they are based on a 10 cm test section and a 9μm, 0.09 NA pitching fiber, the designer may wish to generate a similar map particular to other parameters. To select catching lens parameters from Figure 6-7, the designer simply finds the d_3 and f_2 that correspond to the desired collection fiber parameters (d_5 and NA). Similarly, to select pitching lens parameters, the designer simply finds the d_2 (right axis of the

top panel) and f_1 (left axis of the top panel) that correspond to the same desired collection fiber parameters (d_5 and NA). There is a very important feature of Figure 6-7, or of any figure like it calculated for other test section lengths (L) or pitching fiber parameters (d_1, θ_1). Once the test section length and the parameters of the pitching and collection fibers (diameters and NAs) are chosen, the optimum lenses are determined, independent of K (as opposed to Figure 6-6, which required a known value for K). If K is zero (no beam steering), the lenses provide 100% transmission. If K is less than the K_{max} corresponding to the solution chosen from Figure 6-7, the lenses provide 100% transmission. If K is greater than that K_{max} value, transmission will be sacrificed, but no other choice of lenses would improve the situation (within the assumptions of our treatment). Thus, the following design strategy when designing optical access for an environment with an unknown severity of beam steering is recommended: choose the largest tolerable collection fiber (diameter and NA), use Figure 6-7 (or a source of similar information) to select pitching and collection lenses, and perform the experiment. A transmission of < 100% may be experienced. If that is the case, there are only two possible ways to increase transmission: either relax the largest tolerable collection fiber to an even larger one, or relax the assumptions of this chapter (such as the pure diffusion assumption) and incorporate a more appropriate design methodology.

6.3.2 Experimental Validation

In an attempt to validate Figure 6-7, an experiment was performed to measure the transmission for a single-pass through an optical engine operating in HCCI mode. The engine has a 9.5 cm cylinder bore (L), and was operated at 600 rpm with an equivalence ratio of 0.25. Additional information about the optical access and engine properties can be found in previous papers [27,

28]. The light was collected into a 62.5 μm, 0.266 NA fiber because expected efficient coupling into this fiber was expected to be challenging (in previous experiments using pitching and catching chosen without the aid of this paper fibers of ~ 500 μm diameter had to be used to accommodate beam-steering). Furthermore, coupling into such fibers is required for certain ultra high-speed absorption techniques under development [29]. Finally, with this fiber, the thermal emission collected from the combustion gases is negligible.

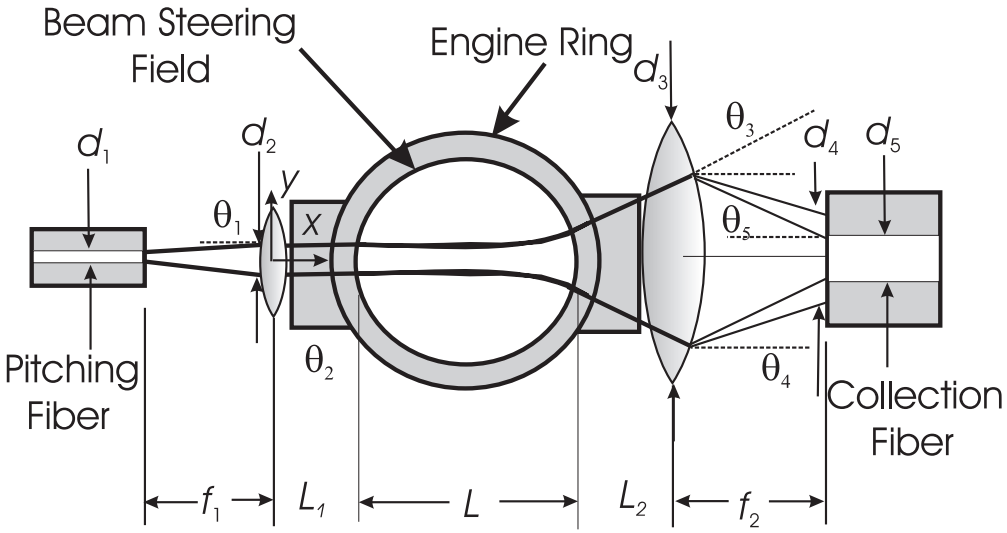

Figure 6-8 – New beam steering model to accommodate engine ring design. The path of the light is not to scale.

A single mode fiber (9 μm, 0.09 NA) and collimation lens were placed 5 cm from one side of the engine, and the collection fiber and lens were placed 5 cm from the opposite side (L_1 and L_2). This is the configuration that is used when the light is being pitched through the HCCI engine, using a ring placed between the engine block and head. Figure 6-8 diagrams the configuration that is used in many of the practical applications presented in this thesis. Note that this diagram

is not to scale, the actual path of the light would not be hindered by the engine ring. The equations were modified to account for these two areas where the light spread without beam steering. The equations from Table 6-2 were essentially the same for this new model. The main difference was the maximum diameter (d_3) and the optimization equation needed to include these sections before and after the beam steering field. Using the small angle approximation, the new equation for diameter was determined to be (to replace 6.2-12):

$$d_3 = d_1\left[1+\frac{L_1}{f_1}+\frac{L}{f_1}\right]+2f_1\theta_1+\frac{4}{3}L^{3/2}\sqrt{K}+2L_2\left[\frac{d_1}{2f_1}+\sqrt{KL}\right] \qquad 6.3\text{-}3$$

And the new optimization equation was determined from Maple to be (to replace 6.3-2):

$$\begin{aligned} 0 = &\left[2\left(d_1\left[1+\frac{1}{f_1}(L+L_1)\right]+2f_1\theta_1+\frac{4}{3}L^{3/2}\sqrt{K}+2L_2\left[\frac{d_1}{2f_1}+\sqrt{KL}\right]\right)\left(\frac{d_1}{2f_1}+\sqrt{KL}\right)^2\right] \\ &*\left[d_1\left(-\frac{1}{{f_1}^2}[L_1+L]\right)+2\theta_1-\frac{L_2d_1}{{f_1}^2}\right] \\ &-\left[\left(d_1\left[1+\frac{1}{f_1}(L_1+L)\right]+2f_1\theta_1+\frac{4}{3}L^{3/2}\sqrt{K}+2L_2\left[\frac{d_1}{2f_1}+\sqrt{KL}\right]\right)^2\left(\frac{d_1}{2f_1}+\sqrt{KL}\right)\left(\frac{d_1}{{f_1}^2}\right)\right] \end{aligned} \qquad 6.3\text{-}4$$

A modified optimum selection map for this special geometry (very similar to Figure 6-7) recommends a pitching lens with f_1 = 3.3 mm and a collection lens with f_2 = 4.4 mm. Among lenses readily available, the diameter specifications (minimum diameters: d_2 = 0.55 mm, d_3 = 1.6 mm) could easily be met, but the closest match to the recommended focal lengths was a 4.5 mm focal length for both the input and output lenses (5.5 mm diameter lens, Thorlabs F230FC-C). Use of these collimation packages resulted in a beam of 0.85 mm diameter entering the engine. For comparison, the transmission was measured with a collection lens further from the ideal recommended by the optimum selection map (Thorlabs F220FC-C with an 11 mm focal length

and 6.5 mm diameter). Figure 6-9 shows the transmission of the two measurements during the compression cycle of the engine, with a rough curve fit added for clarity. At TDC, when the most beam steering would be generated, there was approximately 72% transmission in the near-ideal case, and 26% transmission in the non-ideal case.

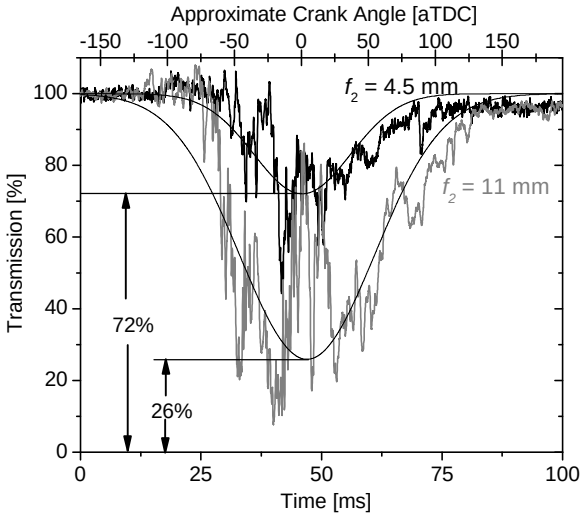

Figure 6-9 – Measured transmission during a single compression stroke of a firing HCCI engine. Data from two lens sets are shown: both have a 4.5 mm focal length pitching lens (f_1), but different collection lens focal lengths (f_2).

The above result lends some credence to Figure 6-7, but it is possible to go further toward actually validating this approach. Taking the 72% transmission (f_1 = 4.5 mm, f_2 = 4.5 mm) case, a measured K (K_{meas} = 0.0004m^{-1}) generated from the engine can be calculated (using equations 6.2-14 and 6.3-5). Using this K_{meas} (rather than the K_{max} used in Figure 6-7), it can be determined that with a collection focal length of 11 mm, one should observe 14% transmission. Since the measured ~26% is near this calculated 14%, the assumptions and models made in the approach retain the rough beam steering physics encountered in the engine.

6.3.3 Comparison of Approaches

Beam steering will have different effects on the two methods of absorption spectroscopy belonging to our case study. The only loss mechanism in the OMA method is caused by the beam being steered outside of the collection fiber's maximum area and NA (as in Eqs. 2-5). The overall transmission of the scanning method on the other hand depends on the amount of light that is lost at the iris, as well as any light that is lost due to beam steering sufficient to cause the output extent to exceed the collection extent. The key advantage of the scanning method is that the spectral resolution of the instrument is defined upstream of the beam steering; therefore beam steering can reduce the total transmission but cannot affect the spectral resolution. Because the spectral resolution is defined upstream, large collection fibers are acceptable to prevent any loss due to beam steering. In the absence of transmission losses due to beam steering, the fractional transmission of the scanning method is directly coupled to the required spectral resolution:

$$T = \frac{d\lambda}{\Delta\lambda} \qquad 6.3\text{-}4$$

(where $d\lambda$ = spectral resolution and $\Delta\lambda$ = bandwidth of source).

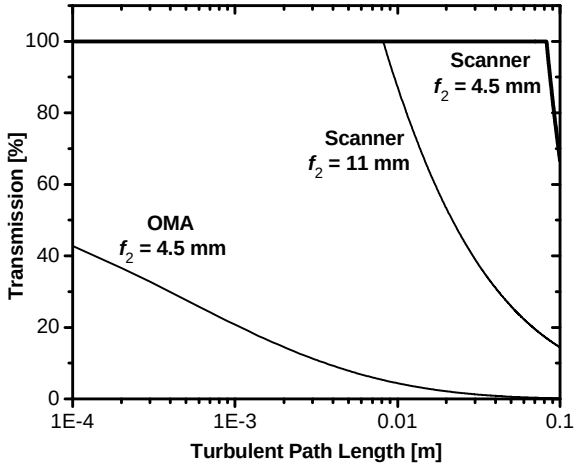

Figure 6-10 – Calculated transmission through a representative turbulent flowfield. The collection fiber in the OMA case is 9μm diameter, 0.09 NA. The collection fiber in the scanner cases is 62.5 μm, 0.27 NA. Assumptions: $K = K_{meas}$, pitching fiber is 9μm diameter, 0.09 NA.

Figure 6-10 shows how the two techniques differ in transmission for identical beam steering fields. The OMA is set to maintain the same spectral resolution as the scanning method by coupling the light back into a single mode fiber to produce 0.06 nm resolution. Figure 6-10 shows that the OMA method cannot handle even small amounts of beam steering unless very poor transmission is acceptable. All of the light in the scanning method can be collected if the light exiting the test section has a lower extent than the extent of the collection fiber. Once this is surpassed, the percentage of light making it to the detector is calculated as seen in Figure 6-10. In this figure, the light for the scanning method was calculated to have been collected into a 62.5 μm diameter, 0.27 NA fiber using the indicated collection lenses

In the remainder of this chapter, assume that for the scanning configuration, all of the light emerging from the test section is collected into a fiber with sufficiently large core diameter and NA, so that there is no transmission loss due to beam steering (T in equations 6.3-3 = 1 for the scanning technique). This assumption is made in order to simplify analysis; however it is often achievable, depending on the required temporal response of the experiment. Referring back to Table 6-1, it is evident that when very high-speed detectors are required and the beam steering is severe, this simplification may not be appropriate.

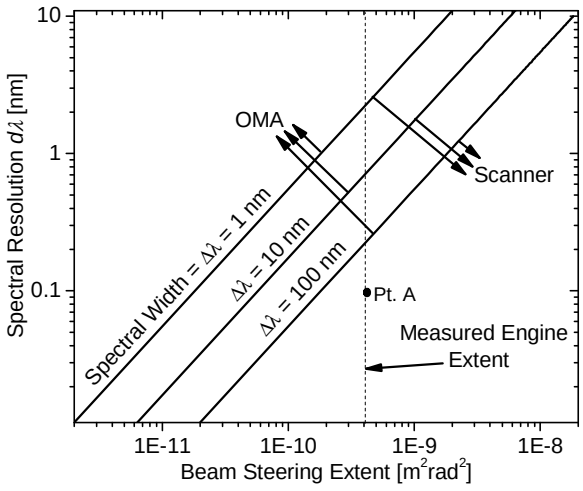

Figure 6-11 – Design guide for choosing between the scanner and OMA methods, showing which technique is preferred for maximizing transmission in beam steering environments. Assumptions: 9μm diameter, 0.09 NA pitching fiber.

Extent collection limits for typical OMAs are a function of their spectral resolution (as shown by combining 6.3-1 and 6.2-13). Setting the scanning transmission equal to the OMA transmission, it is possible to develop a design aid based on required spectral resolution. Figure 6-11 allows the designer to determine the optimal configuration based on specified spectral resolutions,

spectral widths, and amount of beam steering. Here "spectral width" means total spectral range monitored (the scanning range for the scanner method). Note that this figure requires knowledge of the actual K in a given experiment. K could be K_{meas}, or K could be estimated, for example using Eq. 6.2-8. Once the beam steering extent, spectral resolution, and spectral width have been determined and plotted on the graph, the method which will be least affected by the beam steering can be determined. For example, using K_{meas} the extent of our engine can be calculated and then plotted on the figure (as shown by the dashed line). It is possible to then plot a point where a required spectral resolution (say 0.1 nm) meets the engine extent (Pt. A). The figure shows for Pt. A, the scanning method will cause the least amount of overall transmission loss, at least for spectral widths of < 100 nm (in fact, for smaller spectral widths, the scanner becomes increasingly favorable because less light is discarded at the iris). Another example would be if we needed to monitor a spectral width of 10 nm with at least 0.5 nm resolution (in our particular engine), both the scanning and the OMA method would have the essentially the same overall transmission losses. Figure 6-11 shows that as higher spectral resolution is required or more beam steering is encountered, the scanning method is a generally a better choice, whereas opposite conditions would favor the OMA method.

Note that economic factors may need to be considered before selecting a method; a grating, scanning mirror and single detector is generally cheaper than an OMA. Also note that there are other scanning laser approaches capable of much higher spectral resolutions than the scanning case developed in this paper, such as commercial external cavity lasers. Furthermore, use of external cavity lasers in the type of experiments described here can eliminate the loss of light associated with the iris in Figure 6-1 [27]. This general framework might be useful to optical

designers wishing to compare or optimize configurations other than those represented by Figure 6-1 and Figure 6-2. As a simple example - if one wanted to compare the external cavity laser with the OMA method such as in the case study with the scanning method, the external cavity laser would always be favorable because there is no light thrown away at the iris and beam steering does not affect the spectral resolution. Another possibility for this type of study would be to characterize the excess *in-situ* spatial resolution degradation in laser-induced fluorescence measurements; presumably beam steering will degrade the resolution from that predicted by a typical calibration picture.

6.4 Discussion

The two most significant concepts introduced in this chapter are: a methodology for optimizing transmission without quantitative regard to the strength of the beam steering (Section 6.3.1 and especially Figure 6-7) and a framework for choosing an optimum approach for absorption spectroscopy when multiple approaches are available and beam steering is a deciding factor (Section 6.3.3 and especially Figure 6-11). It is hoped that these ideas will be useful to optical designers of future experiments, particularly experiments involving transmission measurements.

This chapter has shown that with a set of assumptions that is often reasonable in practical situations, the performance of an optical system applied in a beam steering environment can be enhanced. The approach delineated in this chapter reduced the collection fiber size from (550 μm, 0.22 NA) to (62.5 μm, 0.27 NA), sacrificing only ~ 28% in attenuation due to beam steering. For absorption spectroscopy measurements, this level of loss is acceptable; thus, from Table 6-1, measured signals can now be collected with a 115 ps time response rather than an earlier limitation of 3.2 ns. Other experimental techniques might also benefit from this type of

analysis. For example, one might be able to quantify or improve the spatial resolution of laser-induced fluorescence measurements in beam-steering environments following methodologies similar to those presented here.

7 Harsh Environments III: Thermal Emissions

Just as gases can absorb photons at specific energies, they can also emit specific energies if they transition from an excited energy state to a lower energy state. Typically, gases will reach an excited state because they are heated. The focus of this thesis is measuring high temperature H_2O absorption spectra. Emission from hot gases will compromise the measured absorption spectra, and potentially compromise the calculated temperature results. This chapter introduces three ways to eliminate issues that arise with thermal emissions in absorption measurements. The best way to eliminate the thermal emission measurements is experimentally. Another strategy is to correct for emission based on measured values, which will be considered real-time numerical correction. Finally, as a last resort, the emission can be estimated and post-processed out of the data.

7.1 Thermal Emission Effects on Absorption Measurements

Figure 7-1 shows the overall effect of emission and beam steering on measured spectra. When spectra were measured with high levels of emission in the engine, turbine and shock tube, they would also contain effects of beam steering. In order to see individual effect of emission, a measured spectrum taken early in an engine cycle (30^o before top dead center), containing no significant measured effects of beam steering or thermal emissions (panel A in Figure 7-1) is used as an example. Emission is artificially added to the measured signal in panel B by adding a constant value to the transmitted intensity (I). Notice that when the transmitted intensity is converted to absorbance ($-\ln(I/I_o)$), the overall spectrum changes shape and has an negative offset (additional measured light will appear as negative absorbance). Beam steering will cause the overall signal to be a fraction of the original signal. Panel C adds artificial beam steering by

multiplying the transmitted intensity by a fraction (in this case, 95% transmission). The effect of beam steering is that the entire absorbance spectrum contains a constant offset, but the overall shape does not change. Technically, beam steering has a weak function of wavelength. Therefore, extremely broad spectral ranges (such as with a super continuum source), beam steering cannot be considered a simple linear function of transmitted intensity. When extremely broad wavelength-agile sources are used, the method presented in section will break down because of the non-constant beam steering. For the FDML laser, this is not a problem. Panel D shows the effects of both thermal emissions and beam steering on a measured spectrum.

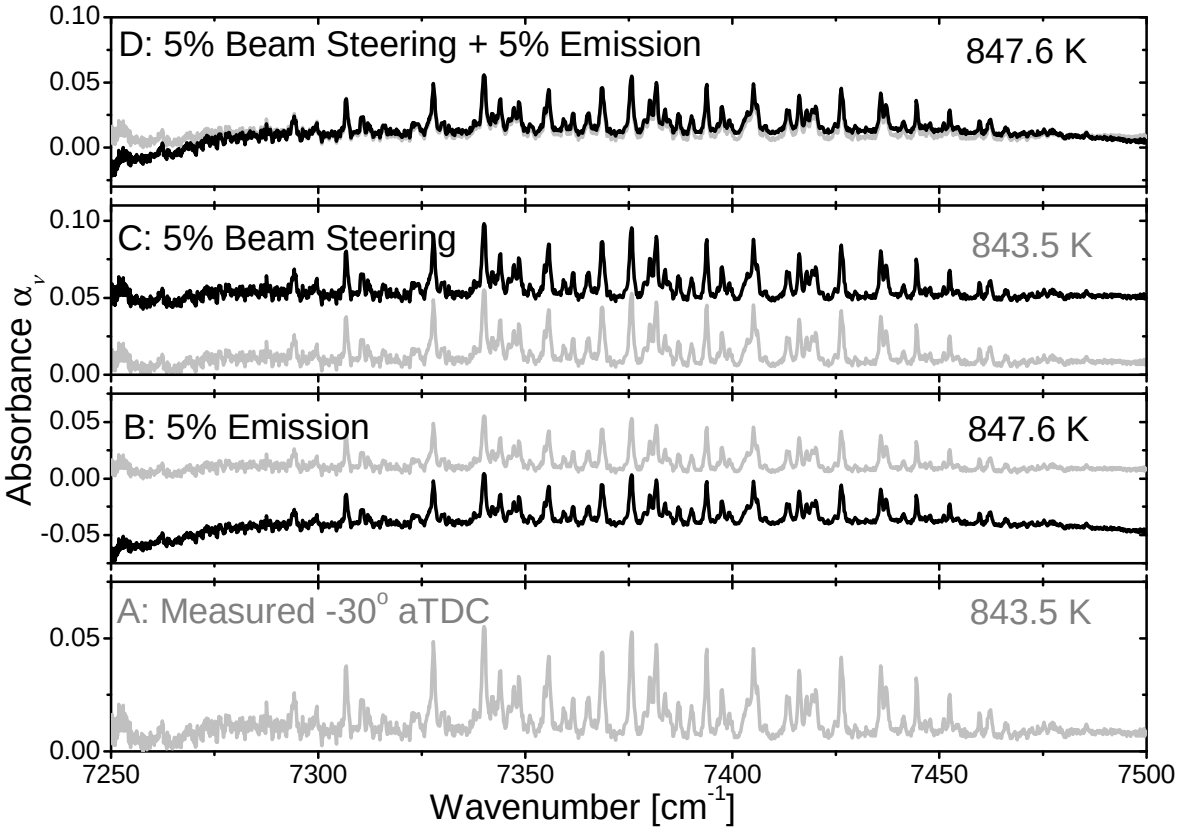

Figure 7-1 – ***A***: Measured spectra at -30 CAD aTDC. No significant emission or beam steering is present. HITEMP calculates 843.5 K from this spectrum. ***B***: 5% emission is artificially added

to the measured spectrum from panel *A*. HITEMP calculates 847.6 K. ***C***: 5% beam steering is artificially added to the measured spectrum from panel *A*. HITEMP calculates 843.5 K. ***D***: 5% emission and 5% beam steering artificially added to the measured spectrum from panel *A*. HITEMP calculates 847.6 K from this measured spectrum.

The upper right corner of each panel in Figure 7-1 contains the temperature calculated from the HITEMP database. For these small amounts of beam steering, temperature calculations are unaffected. The reason to try to eliminate beam steering as discussed in the previous chapter is to improve signal to noise ratios, as well as allowing smaller and faster detectors to be used. The effect of a small amount of thermal emission does somewhat effect the calculated temperature. Even though this condition only changed the calculated temperature less than 0.5%, it highlights the need to eliminate the effects of emission whenever possible.

7.2 Experimental Elimination

In general, using a wavelength-agile source will automatically reduce the effect of emission on absorption measurements compared to the more traditional light source + spectrometer techniques (for example, the OMA introduced in Chapter 6). At any instant, the wavelength-agile source is at one particular color, and is measured using a simple photodetector. Broadband emission will be evident as a uniform overall increase in the signal throughout the laser scan. Using a traditional light source + spectrometer technique, the emission will be detected like any other light. Since absorption and emission take place at the same spectral energies, this could seriously compromise the results.

Aside from using a wavelength-agile source, there are other experimental practices that can help to eliminate measured thermal emission. The phasing and direction of thermal emission is random. Therefore, thermal emission can be collected on the detector from any direction or angle. A small iris placed in front of the detector (or detector lens), at the width of the laser beam, will remove any stray light not originating from the path of the beam. This is considered spatial filtering.

Spatial filtering can be coupled with spectral filtering to further reduce the measured thermal emission. Bandpass filters are filters that allow only a select band of light to pass through. A bandpass filter that allows only the light in the same range as the wavelength-agile source can eliminate emissions that are originating from unknown emitters. A bandpass filter will not prevent H_2O emissions to be measured if H_2O is the measured absorbing species, since absorbing and emitting energies are the same. The bandpass filter will help when other sources of emission are present. Soot created during combustion, deposits accumulated on the windows, emission from the windows themselves, and the possibility that the detector can view other hot surfaces such as combustor walls can all contribute to the relatively high emission. If these emissions are high enough (for example, if the detector becomes saturated), the bandpass filter can be accompanied by a neutral density filter to further reduce the measured signals. The neutral density filter will reduce the laser signal as well, so it would only be appropriate under extreme conditions.

7.3 Measured Correction

Emission may still be measured even when all of the experimental practices described above are employed. A strategy can be implemented to correct for this measurement which is practically

real-time. All of the wavelength-agile lasers described in this paper have a favored scan, either red-to-blue, or blue-to-red. It is difficult to optimize any of the lasers for both scanning direction. This can actually be advantageous because the laser can then be turned off during the unused laser scan. With the laser off, the measured signal is the total effect of emission. Figure 7-2 shows the raw signal from an HCCI engine measurement. The black line is taken at TDC, where ~0.05 V of total emission detected when the laser is shut off. The grey line is -60 CAD aTDC. No significant amount of emission is detected at this crank angle. The hatched lines show where the signal is not used for any calculations. The first 200 data points are averaged to calculate the average emission measurement. The next section of data is not used. The average emission measurement is then subtracted from each point in the useful scan before the signal is converted into absorbance.

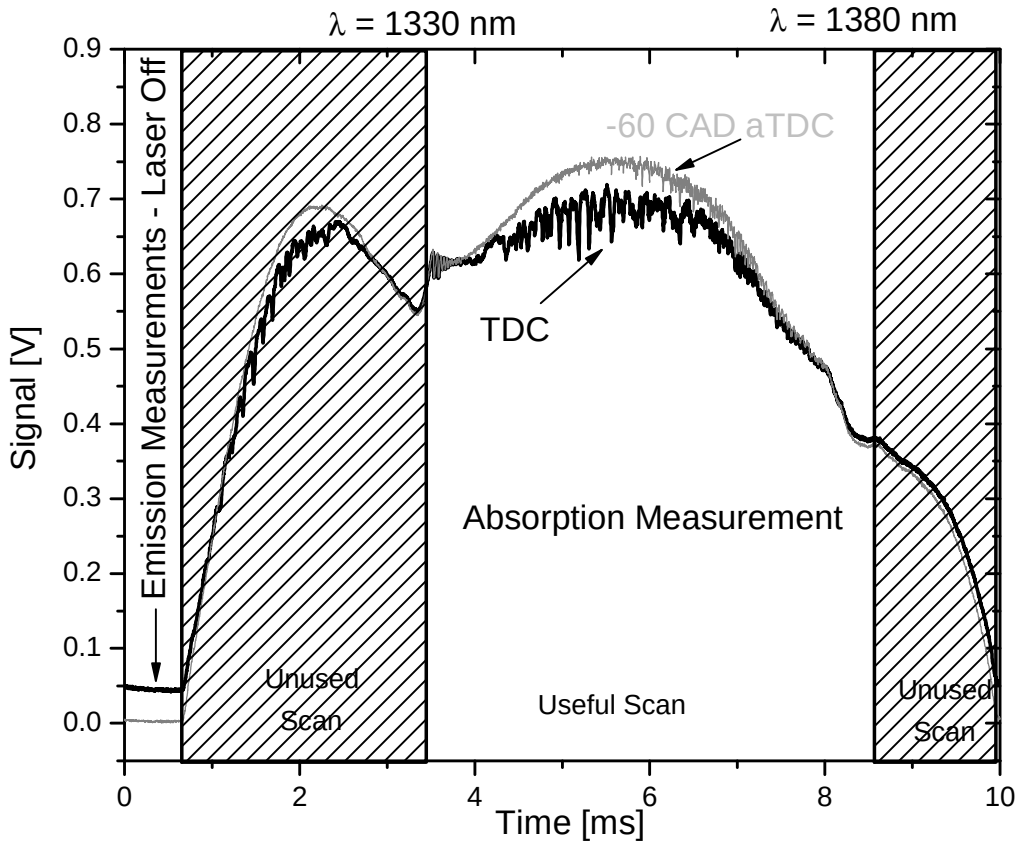

Figure 7-2 – Two raw measured signal from an engine measurement. The black line is taken at TDC, where ~0.05 V of total emission detected when the laser is shut off. The grey line is -60 CAD aTDC. The hatched lines show where the signal is not used for any calculations.

7.4 Post Processing Corrections

There may be circumstances in which emission cannot be eliminated from the measurements, and the laser cannot be shut off to obtain an experimental measure of emission. This section describes a method to calculate emission based on a measured spectrum. The method will only work for wavelength-agile absorption spectroscopy measurements because it assumes that the effect of thermal emissions is a constant signal added to the measured spectra (at all wavelengths).

Figure 7-3 shows two measured absorbance spectra, the top panel at top dead center, and the bottom panel 90^o before TDC, which is the earliest measurement in the engine cycle that was taken. Figure 7-3 does not use a baseline fitter as many of the spectra presented in this thesis do. A baseline fit is never used in temperature calculations, but typically used to make the spectra look more presentable (this is described in the next chapter). A baseline was fit to the bottom panel of Figure 7-1, and that same baseline was used in the upper panels. Having a non-uniform baseline, such as in Figure 7-3 can be helpful in calculating the effect of thermal emissions.

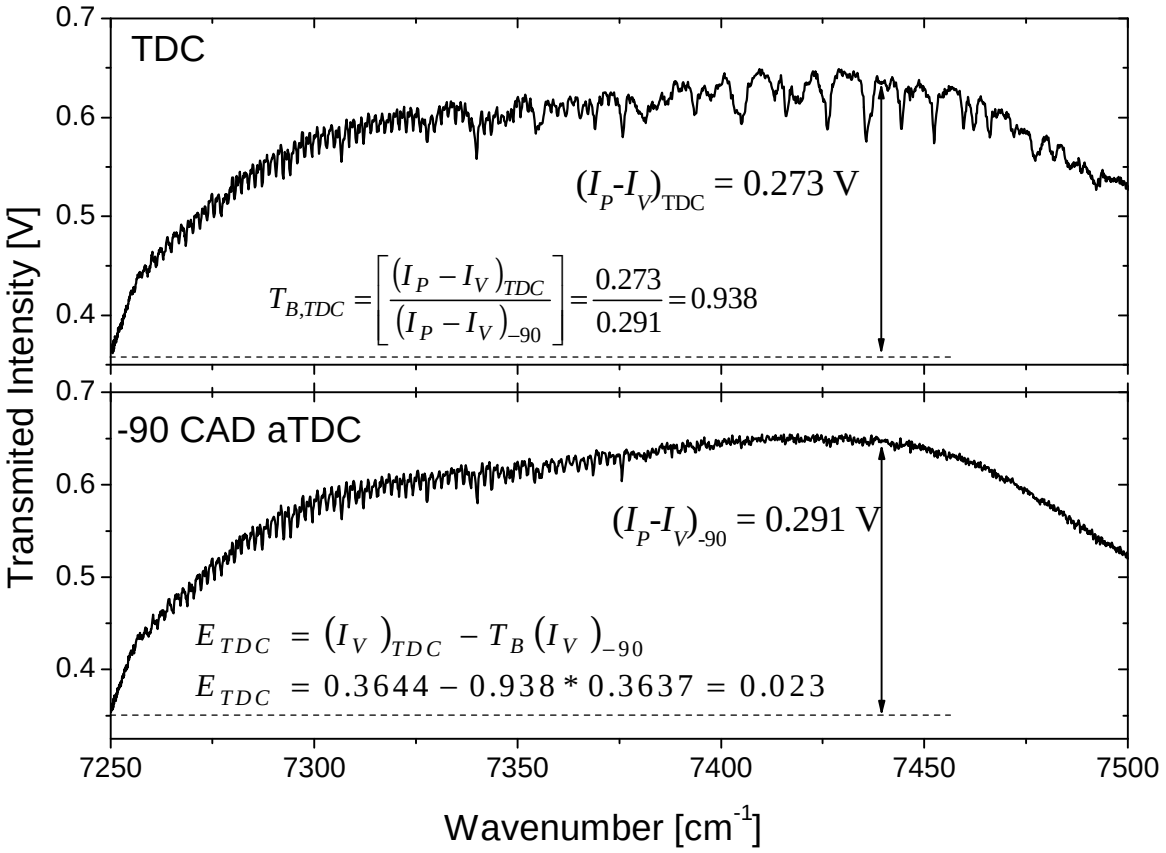

Figure 7-3 – *Lower panel*: Measured signal taken 90^o before TDC. This condition will have the least amount of beam steering and thermal emissions from any of the measured spectra. *Upper panel*: Measured signal taken at TDC. Thermal emission and beam steering will be present.

Each measured spectrum will be compared to the spectrum measured earliest in the engine cycle, which will contains the least amount of both beam steering and emissions. First, a measure of beam steering is calculated. This is done by picking two wavenumbers in the spectrum that contains no water absorption lines. The measured transmitted intensity at the two points should be near a peak (I_P) and a valley (I_V) based on the overall spectrum, but off of an absorbance line. An average of a couple of data points near the peak and valley could also be taken if significant noise is present. The following equation calculations the fractional transmission due to beam steering (T_B) at one particular crank angle (CAD):

$$T_{B,CAD} = \left[\frac{(I_P - I_V)_{CAD}}{(I_P - I_V)_{-90}} \right] \qquad 7.4\text{-}1$$

To calculate a correction value for emission at one particular CAD, equation 7.4-2 calculates an offset due to emission (E_{CAD}) based on the same measured absorbance values:

$$E_{CAD} = (I_V)_{CAD} - T_B (I_V)_{-90} \qquad 7.4\text{-}2$$

Absorbance corrected for emission can then be calculated at each wavelength from the following equation:

$$\alpha_{\nu,CAD} = -\ln\left[\frac{I_\nu - E_{CAD}}{I_{o,\nu}} \right] \qquad 7.4\text{-}3$$

This is not a perfect correction for emission. It assumes that no emission or beam steering is occurring in the first measured spectrum (for this case, -90 CAD aTDC). It also heavily relies on

individual transmitted intensity measurements, which generally are noisy. The measured emission value based on the procedure in section 7.3 for the spectrum in Figure 7-3 was 0.019 V, whereas the calculated emission value as described in this section is 0.023 V. The temperature calculated without any correction for the TDC spectrum from Figure 7-3 is 1703.9 K, the temperature with the correction from section 7.3 is 1702.59 K, and the temperature calculated based on this post-processing method is 1702.32 K.

Going back to Figure 7-1, this spectrum, with essentially no emission or beam steering, calculates a temperature of 843.5 K. Without any correction, the calculated temperature with artificially added emission is 847.6 K (0.48% error). Using the method presented in section 7.3, the calculated temperature is 843.5 K (0% error), whereas the method presented in this section is 844.8 K (0.15% error). While the effects of thermal emission appear small in this example, it is because the example was trying to duplicate the effect of emission found in the HCCI engine. Other engines or experiments, especially the gas turbine experiments, have much stronger sources of emissions.

7.5 Conclusions

This chapter presented ways to eliminate the effects of thermal emissions on absorption spectroscopy measurements. Wavelength-agile strategies in general will be better suited for dealing with emission contamination compared to spectrometers when taking absorption measurements. Other experimental procedures that were recommended were spatial and spectral filtering. A real time emission correction measurement was also described to further reduce the effects of thermal emission on temperature calculations. As a last resort, thermal effects can be post-processed out of measured spectra obtained with a wavelength-agile source.

Although this chapter focused on eliminating thermal emission measurements, emission spectra can contain as much information as absorption spectra. Difficulties that arise with thermal emission measurements are that the signals are generally very weak, and they rely on the measuring species to be hot. Temperature measurements derived from emission spectra will tend to be biased too hot under non-homogenous conditions. Temperature measurements derived from absorption spectra tend to be biased cold under non-homogenous conditions. Future studies could simultaneously measure absorption and emission spectra, and perhaps extract more information about the state of the measured gas.

8 Methods for Calculations

This chapter provides the details to calculate temperature, pressure and absorber mole fraction from measured spectra. The calculations rely on spectrally broad absorption measurements to be obtained. There is no minimum spectral range for the measurements; however, this technique will work best when at least one full rotational branch of a molecule is measured. The methods presented in this paper assume that the measured spectrum encompasses the R-branch of the ν_1+ ν_3 band of H_2O; however, the techniques should work for most measured spectra.

The basic approach is to measure a broad absorption spectrum, ideally an entire rotational branch of a molecule (50 nm works for the R-branch of the ν_1+ ν_3 band of H_2O). Then, logically compare that spectrum to a set of known spectra. Based on how close the measured spectrum matches the reference spectra, temperature and mole fraction values are determined. This chapter will begin by describing the basic methodology of creating a database of reference spectra. The specific steps to calculate temperature, mole fraction, and a method for pressure will then be presented. Finally, two troubleshooting techniques, baseline fitting and axis warping will be presented. These are important if the laser source is behaving poorly, or other non-ideal conditions are present.

8.1 Reference Spectra

The first step is to have the ability to create reference spectra. For a complete review of fundamental spectroscopy, many complete reference materials are available [68, 69], therefore only a simplified overview will be provided here. Following the review of spectroscopy, a discussion of how to choose the library of known spectra is presented.

8.1.1 Spectral Simulations

As stated in Chapter 1, spectroscopy is governed by the Beer-Lambert law, where:

$$\left(\frac{I}{I_o}\right)_\nu = \exp(-k_\nu L) \qquad 8.1\text{-}1$$

The product $k_\nu L$ is termed absorbance (abbreviated α_ν). This is summarized in equation 8.1-2:

$$\alpha_\nu = -\ln\left(\frac{I}{I_o}\right)_\nu = PX_i S_i(T)\phi_\nu L \qquad 8.1\text{-}2$$

Values required to simulate absorption spectra can be measured, however they are generally cataloged with sufficient accuracy. The HITRAN (**Hi**gh resolution **tran**smission) database was originally developed for atmospheric studies, but it is also quite useful for a variety of other spectroscopic studies. H_2O is one of many molecules included in the database. HITRAN 2004 is the latest version of the database [15], although HITRAN 2000 includes a supplemental file (HITEMP) which is better suited for high temperature, high pressure simulations [70]. All versions of HITRAN are compatible with a compiler called HAWKS (**H**ITRAN **A**tmospheric **W**or**ks**tation), which allows a user to input the desired molecule, isotope, and optical range. An output file then lists important spectroscopic parameters (see [15] for a complete list), including $S(T_o)$ and E'' at line-centers ν_o.

The more accurate the simulations, the more accurate the calculations will be. Sufficient accuracy may require one to include effects that were not mentioned in this section. For example, collisional narrowing and line shifting may be important depending on the testing conditions. It is also important to consider the effects of database errors. For example, HITRAN 2004, the latest release relevant to the $\nu_1+\nu_3$ band of H_2O, is known to have errors [19, 20, 71-73]. The errors are often reduced with each new release of HITRAN.

8.1.2 Reference Spectra Requirements

Once known spectra can successfully be simulated from parameters found from HITRAN (or a similar database), a library of pre-compiled reference spectra can be produced. This section will discuss the requirements for optimal calculations, and tips on organization.

The method for calculating temperature involves comparing measured spectra with a logical set of known spectra (as calculated in section 8.1.1). This involves choosing a range of temperatures and pressures to simulate. To calculate mole fraction, assume that the entire spectrum simply scales linearly with concentration; therefore only one mole fraction has to be simulated. This assumption neglects changes in broadening associated with changing gas composition, an effect that can often be neglected in lean combustion application, but in general should be considered.

Considering the wide range of conditions that can be measured using this method, a simulated reference library was created. A 51 x 105 matrix of conditions is sufficient to measure temperatures from 280 K to 3200 K, and pressures from 0.1 atm to 40 atm. There are 51 temperatures simulated at each of the 105 pressures (5355 total simulations). Each temperature simulation is 5% larger than the previous simulation (the first simulation is at 280 K, the next is 5% higher at 294 K, then 308.7 K, and so on), while each pressure simulation is 6% higher than the previous simulation (0.1 atm, 0.106 atm, 0.112 atm, and so on). These increments are described in Eqn. 8.1-8 and 8.1-9.

$$T[i] = 1.05^{i} * T_o \{i = 0:50\} \qquad 8.1\text{-}8$$

$$P[j] = 1.06^{j} * P_o \{j = 0:104\} \qquad 8.1\text{-}9$$

Aside from temperature and pressure, several other variables can be adjusted when creating a spectroscopic reference library, such as spectral resolution and the breadth of the spectral range simulated. Although there is nothing wrong with simulating an extremely broad spectrum at high resolution, the database may become unnecessarily large. This could cause problems such as calculations becoming too computationally expensive or time consuming for practical use. While trying to keep the database down to a reasonable size, it is important to keep the structure of the features intact. For example, when pressure increases, multiple absorption lines will blend together to suggest singular features. It is therefore not as critical to have a fine resolution for higher pressure simulations compared to simulations at lower pressures. We have found that a feature is adequately modeled by 50 points (that is, 50 points distributed over the FWHM of a feature). Therefore, to determine the required resolution of the simulation, the average FWHM should first be estimated. The library begins with low pressure (0.1 atm) simulations that have a point every 0.005 cm^{-1}, and increases to 0.1 cm^{-1} resolution at 40 atm.

Finally, the organization of the reference spectra should be carefully planned out before the simulations are performed. For the library used in this project, each simulation was saved as an individual 2-D array (one column optical frequency [cm^{-1}], one column absorbance [cm^{-1}]). The files were organized such that there were 105 pressure folders (named “0” through “104”), each containing 51 files (named “0” through “50”). To open a specific simulation, it was simple to program a path opening subprogram. For example, a simulation that is 0.1 atm, 280 K would be folder 0, file 0 (Base path\0\0.dat – or using the convention from Eqns. 8.1-8 and 8.1-9: Base path\$j$\$i$.dat). This strategy is nice for accessing individual files quickly.

8.2 Calculation Methods

This section will describe the details for calculating temperature, mole fraction, and pressure based on measured absorption spectra.

8.2.1 Temperature

The method for determining temperature involves individually comparing a measured spectrum with a series of known spectra. An emerging class of hyperspectral sources (such as wavelength-agile or rapidly wavelength-swept lasers) allows non-invasive, rapid acquisition of spectra in a wide range of harsh environments. Because these lasers are relatively new, they may have poor resolution, noise originating from the laser, or scan-to-scan intensity fluctuations. The following method will often produce satisfactory results even in the presence of these and other issues.

8.2.1.1 Spectral Preparation

Initially, the measured signals need to be converted into absorption spectra. Generally, this will be done by converting optical transmission into absorbance (Eqn. 8.1-1), and then dividing by the path length to get absorption coefficient versus optical frequency. The x-axis for the spectra is determined by finding the maximum and minimum wavenumber (ν_{max} and ν_{min}) using an optical spectral analyzer. These extremes are used to generate the wavenumber axis assuming sinusoidal motion within the FFP-TF in the FDML laser. The conversion from data point *i* to wavenumber ν_i for *N* number of points was simply:

$$\nu_i = \bar{\nu} + \left[\frac{\nu_{max} - \nu_{min}}{2}\right] \sin\left(2\pi \frac{i}{N} + \phi\right) \qquad 8.2\text{-}1$$

The offset (ϕ) is found manually by matching water absorption peaks from our database with the measured peaks. This process could also be automated relatively easily.

The first step is to help alleviate high frequency noise. To do this, both the measured and simulated spectra are smoothed. The points are convolved with a Gaussian pulse, although other smoothing filters produce similar results. There is very little sensitivity of the final results to the smoothing technique used; however, on the basis of physical arguments, convolving the spectra with a Gaussian profile was chosen. The optimum degree of smoothing depends on many factors including the spectral resolution of the measurements, the test conditions of the gas (primarily the pressure range), whether or not pressure is to be inferred from the spectra, and the amount of noise present (in particular the Fourier spectrum of the noise). For example, in the piston engine the majority of the compression stroke involves pressures ranging from 5-35 atm. In this range, if the laser resolution is 0.5 cm^{-1}, smoothing the signal to 2 cm^{-1} does not compromise the major features. On the other hand, 2 cm^{-1} could be too much smoothing for lower pressure studies with a high resolution laser source, particularly if low-frequency noise is present. The amount of smoothing should be carefully considered: enough to reduce high frequency noise, but not too much as to eliminate major features. Another point concerning smoothing is to consider the spectral resolution of the laser source. If the resolution of the laser is poor, the measured spectrum is already somewhat smoothed. In this case, use a mean squared analysis to match the smoothing of the reference spectra:

$$\Delta\nu_{ref} = \sqrt{\Delta\nu_{laser}^2 + \Delta\nu_G^2} \qquad 8.2\text{-}2$$

where $\Delta\nu_{ref}$ is the smoothing factor of the reference spectra, $\Delta\nu_{laser}$ is the spectral resolution of the laser, and $\Delta\nu_G$ is Gaussian smoothing factor that should be used for the measured spectrum.

Aside from high frequency noise, low frequency noise and spectral offsets can also be a problem when taking measurements in harsh environments. Wavelength dependent interferences such as broadband absorbers, window fouling, or beam steering can cause the measured spectrum to have a baseline that is significantly higher than zero. Taking the derivative of the smoothed spectra eliminates these offsets, and was found to be a convenient systematic method for dealing with measured spectra. Other approaches for dealing with offsets and slowly varying baselines, such as subtracting from each point the minimum value of the spectrum, using a bandpass filter, and taking an FFT are also acceptable solutions. We found however, that taking the derivative after smoothing was faster (as opposed to an FFT), required no adjusting from one experiment to another (as opposed to a bandpass filter), and less sensitive to any remaining noise in the spectrum (as opposed to the subtraction method).

Figure 8-1 summarizes the smoothing and differentiating technique. The bottom panel of Figure 8-1 shows an absorption spectrum. The middle panel is a plot of the spectrum smoothed to 2 cm^{-1} ($\Delta \nu_G$). The top panel shows the derivative of the smoothed spectrum. This process should be done on both the measured and the library spectra. To reduce calculation time, there are actually 2 spectra libraries: the “base” library is the spectra described in section 8.1.2 (bottom panel), the other is the smoothed and differentiated spectra of the base library (top panel).

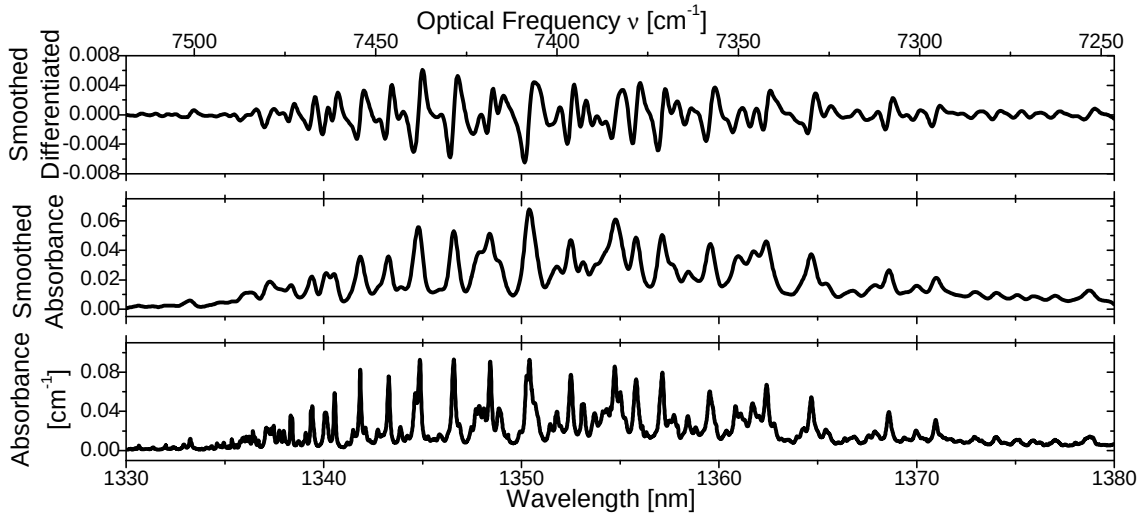

Figure 8-1: The three steps to prepare both measured and simulated spectra. *Bottom panel:* Actual absorption spectrum (absorption coefficient vs. wavelength). *Middle panel:* Spectrum smoothed to 2 cm^{-1}. *Top panel:* Smoothed, differentiated spectrum.

8.2.1.2 Calculation Method

After smoothing and differentiating the measured and simulated spectra, the spectra should be interpolated such that the measured and simulated spectra have points at exactly the same resolution. Using the R-branch of the $\nu_1+\nu_3$ combination band of H_2O, we have found that having one data point every 0.25 cm^{-1} is sufficient for measurements ranging from 5-35 atm. Just as with the amount of smoothing, it is important to consider the resolution. Finer resolution is required for lower pressure measurements so that all spectral lines are represented, but at higher pressures, there is a point of diminishing returns when comparing resolution and calculation times.

As discussed in 8.1.2, the pre-compiled library will have a known set of temperatures and pressures. For the basic temperature calculation (a more advanced scheme will be described in 8.2.3), an external measurement of pressure is required e.g., using a pressure transducer. The measured, smoothed, differentiated spectrum is individually plotted versus each of the smoothed differentiated simulated spectra from the library at the set of temperatures corresponding to the nearest measured pressure. The measured and reference spectra should have exactly the same spectral range and resolution, which will most likely require interpolating one of the spectra. A line is fit through each plot using the method of general linear least squares as a maximum likelihood estimator (see [74], pp. 656-675 for excellent step-by-step instructions). The mean squared error (MSE) for each condition is calculated and saved. Two examples are shown in Figure 8-2, the top panel is a good fit compared to the bottom panel which is a poor fit. Finally, the location of the minimum of the MSE versus known temperatures is interpolated (see Figure 8-3), giving the temperature. The plots that have been provided (Figure 8-2 and Figure 8-3) show an example in which the final calculated temperature is 1231.45 K. To increase the speed of calculations, plots do not need to be displayed. Also, more efficient algorithms could be implemented to converge to a solution, rather than calculating through all temperature conditions. Shock tube studies have shown this method accurate to about ±2.5% up to 1000 K [75].

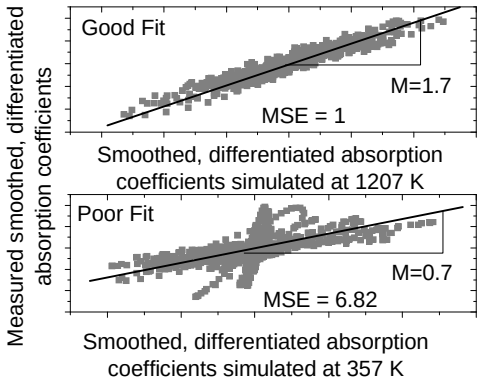

Figure 8-2: Measured versus known smoothed, differentiated absorption coefficients. *Top panel:* The measured coefficients are compared to coefficients simulated at 1207 K. The mean squared error is normalized to 1, and the slope of the best fit line is 1.7 *Bottom panel:* The measured coefficients are compared to coefficients simulated at 357 K. The normalized mean squared error is 6.82, and the slope of the best fit line is 0.7.

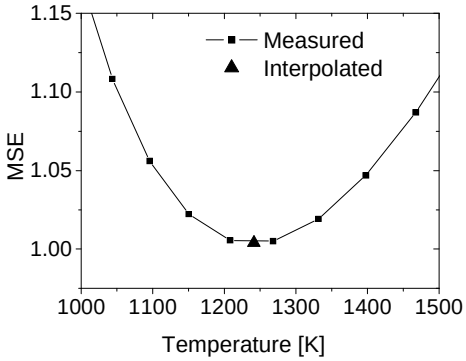

Figure 8-3: Mean squared error versus known temperatures. Square points are calculated from spectra in the pre-compiled library. The triangle indicates the predicted MSE of the measured spectrum.

8.2.1.3 Discussion on Temperature Calculations

In order to get the most accurate measurement possible, the spectral range should be carefully considered. In H_2O measurements, the most accurate results over the widest range of

temperatures are calculated when an entire branch of the spectrum is measured. This study measures the R branch of the $\nu_1+\nu_3$ combination band of H_2O (7246.4 – 7518.8 cm^{-1}). Because this branch is more congested, it is easier to engineer a light source that encompasses the entire branch. When it is not possible to measure the whole spectrum, the temperature results will become biased. If measurements are not included near the band center, the temperature results will be calculated too high since the stronger cold lines are not included. Likewise, if the spectral measurement does not extend far from the band center, the results will be biased cold because crucial hot lines are not contributing to the calculation.

Another consideration for these measurements is the overall validity. These results will be path-integrated over a line-of-sight. This means that if the test gas is exceptionally non-homogeneous, the result will still be one value. The usefulness of that value should be considered. If there are large temperature extremes within the test gas, the results will be biased cold. For roughly homogeneous systems, such as HCCI combustion, shock tubes, and pulse detonation tubes, the results of these calculations can be very useful for physical studies.

8.2.2 Mole Fraction

Once the temperature has been calculated, the mole fraction of the measured species can easily be determined. Section 8.2.1 described fitting a line through the measured versus known absorbance plot. The slope of the calculated temperature is then interpolated from the values of the slopes at known temperatures, as shown in Figure 8-4. Since the mole fraction of the reference spectra is known, the final interpolated slope can be used as a scaling factor. For example, our pre-compiled library is all simulated at 5% H_2O mole fraction. If the slope of the best fit line in the measured versus known plot (as in Figure 8-4) is 0.764, then the calculated

mole fraction for the measured spectrum would be 0.05*0.764 or 0.0382 H_2O mole fraction (3.82%). This method has been shown to calculate H_2O mole fraction up to 2% accurate in a combusting engine [28]. Extending this method to multi-species measurements is possible; however, it does add some complexity to the overall method.

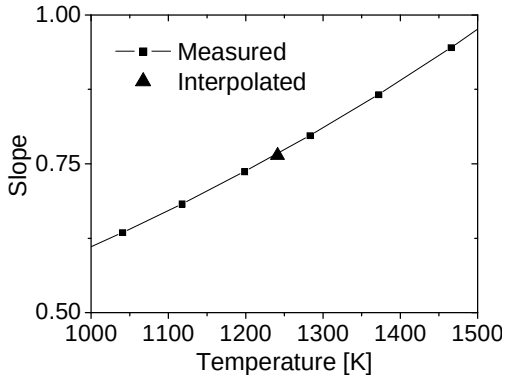

Figure 8-4: Slopes of the best fit lines from Figure 8-2 versus the corresponding known temperatures. Square points are calculated from spectra in the pre-compiled library. The triangle indicates the predicted slope for the best fit line of the measured spectrum.

8.2.3 Pressure

In this section, we present a method to calculate pressure based on measured absorbance spectra. Pressure transducers are easy to use, cheap, and very accurate relative to the method presented here. However, there may be cases where transducers are difficult to implement, such as in supersonic flows where the pressure away from accessible surfaces is desired. The method presented in this section will describe how to calculate temperature, mole fraction, and pressure without an external pressure measurement.

8.2.3.1 Calculation Method

The first step is to calculate temperature and mole fraction as described in sections 8.2.1 and 8.2.2, except instead of choosing the spectra closest to the measured pressure, choose the spectra

at one arbitrary pressure. The closer the guess value is to the actual pressure, the quicker the solution will converge. This initial calculated temperature is then used to calculate pressure in much the same manner as the temperature calculations.

Spectral features broaden with increasing pressure. Therefore, it would be unacceptable to use the same smoothing technique that is used in the temperature calculations for the pressure calculations. Without performing the smoothing, taking the derivative also becomes more difficult. Large spectral offsets and low frequency noise still need to be accounted for. To compensate for these effects, fit a baseline to the measured and the pre-compiled spectra, and subtract that baseline from the spectra (both measured and library). The method for calculating a baseline will be discussed in section 8.3.2.

The measured spectrum is plotted against all of the pre-compiled spectra that are nearest to the temperature calculated with the initial pressure guess. It is important to interpolate so each spectrum is at the same resolution. As in section 8.2.1, a line is fit through each plot, and the MSE is recorded. The minimum MSE is interpolated from the saved MSEs in order to determine the calculated pressure. The new calculated pressure can then be used as a better input to repeat the temperature calculations. The entire process can be repeated until the temperature and pressure results converge to one solution. We have found that when the initial guess pressure is within 50% of the actual pressure, the solutions converge in two iterations.

8.2.3.2 Discussion on Pressure Calculations

We present the method in 8.2.3.1 mostly as a way to calculate temperature without the requirement of an external pressure measurement. Using HITRAN for producing reference

spectra, we have not generally computed accurate pressures. There are several reasons for this. If the spectral resolution of the laser is not excellent, the laser signal will broaden features, biasing pressure results high. For wavelength-agile systems, this is often a problem. Previously measurements have been reported where high pressure simulations were broader than measured spectra [75], implying that the simulated spectra were not accurate. Collisional narrowing was theorized to be required in the simulations (previously ignored), as well as improving broadening coefficients in the databases.

Figure 8-5 shows the results of the calculations of pressure, temperature, and mole fraction using both methods presented in this paper. The initial pressure guess was set to 1 atm for the calculations using the method presented in section 8.2.3. In this figure, the thick black line is the measurement from the pressure transducer (as described in section 8.2.1), the thick grey lines are the initial results from the 1 atm pressure guess, and the thin black lines are the results of the next 2 iterations. A significant difference is noted in the pressure results of Figure 8-5 (lower panel). The final calculated results are generally higher than the transducer measurements, most likely due to the poor laser spectral resolution broadening measured features. The high pressure, lower temperature features had the opposite problem, where the measured pressure was higher than the calculated, possibly due to collisional narrowing not being included in the reference spectra. The temperature results of Figure 8-5 are very similar whether or not the transducer measurement was used (after iteration). Mole fraction results are compromised when pressure values are calculated rather than measured. This makes sense since mole fraction and pressure are tied closely together when looking at the overall height and width of spectral features (Eqn. 8.1-5).

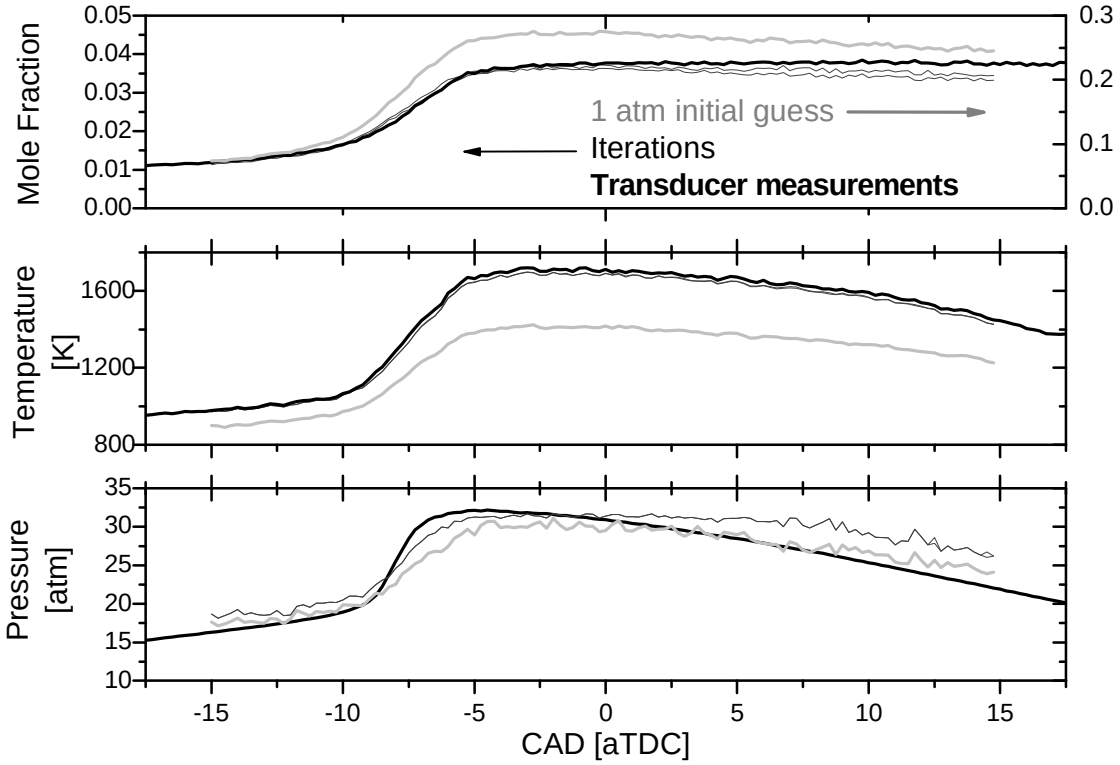

Figure 8-5: Results from a firing HCCI engine experiment as a function of crank angle degrees (CAD) after top dead center (aTDC). *Lower Panel:* Pressure as measured by a pressure transducer (thick, black line) compared to pressure calculated by spectroscopic measurements. The grey trace is the initial result based on a guess pressure of 1 atm. Each plot also has two thin black lines which are the results based on the next two iterations. *Middle and Upper Panels:* Temperature and mole fraction results using the pressure transducer values as input (thick black traces) compared to calculations made without the transducer (grey and thin black traces).

8.3 Troubleshooting

Dealing with harsh environments such as piston cylinder engines, as well as non-ideal laser sources makes accurate absorption measurements difficult. This chapter discusses a robust method to calculate temperature and mole fraction even with noisy spectra. There are

occasionally even more extreme situations that require additional measures to obtain accurate results. A description of axis warping and baseline fitting is provided to assist in analyzing all spectra.

8.3.1 Optical Frequency Axis Warp

There may be times when the optical frequency axis (*x*-axis of the absorbance spectrum) is not well known. It is also possible that there are errors concerning locations of absorption peaks in the HITRAN database. The easiest way we have found to deal with these issues is to warp either the measured or the known frequency axis.

To warp the *x*-axis of one of the spectra, reference points on both measured and simulated spectra must be chosen. We found using the peaks of strong absorption features works well. The peaks can be automatically found, manually chosen, or a combination of the two. For example in our codes, both spectrums are divided into equal parts, and the maximum point in each section is initially set as a cursor locations. These cursor locations can then be manually adjusted to have complete control over the reference points. Care must be taken to assure that the same feature that is referenced in the simulated spectrum is also referenced in the measured spectrum (so there should always be a pair of reference points). A spline is then fit through the measured reference points versus simulated reference points. Finally, the points of the warped spectrum are used to interpolate values from the calculated spline. As a reminder, it may be required to interpolate this axis yet again if performing a temperature calculation, such that the resolution of both measured and pre-compiled spectra are identical.

8.3.2 Baseline Fitting

There may be times when taking the derivative of the spectrum is not enough to eliminate a non-linear baseline. An example of this situation is if quartz windows are used to gain optical access. Quartz absorbs strongly in the same spectral range our preferred H_2O branch. The baseline of the measured spectrum in this case has an S shape to it. To solve this problem, we fit a baseline to the measured spectrum, and then subtract that baseline out.

To fit the baseline, reference points are chosen on the measured spectrum. This can be done in much the same manner as the axis warping. In our codes, the spectrum is divided into equal parts, and the minimum point in each section is initially set as a cursor locations. The cursor locations can then be manually adjusted to have complete control over the reference points. A spline is then fit through the reference points. The entire optical frequency axis is then used to interpolate absorption values from the calculated spline. These absorption values can then be subtracted out of the original spectrum to remove non-linear baselines.

8.4 Conclusions

This chapter presented a detailed explanation of temperature, mole fraction, and pressure calculations than can be performed on spectrally broad measured absorption spectra. The calculations will be especially useful for wavelength-agile laser systems because of the robust nature. Descriptions of spectral simulations, database structure, and calculation methods were discussed. Temperature and mole fraction accuracies as good as 2.5% have been reported using this method. Pressure measurements are more difficult, and are not meant to replace pressure transducers. The results of this type of measurement will be line-of-sight path integrated. Studies are being done to explore the possibility of extending these calculations to tomographic

reconstructions and multi-species measurements. Additionally, future studies could be done to explore the feasibility of extending this method to emission and fluorescence spectra. Reconstructing a single measured spectrum into multiple spectra based on a range of temperatures may also be useful, especially in non-homogenous situations. Measuring broad absorption spectra can give a wealth of information when trying to understand combustion problems, or other physical phenomenon. The method presented here describes how to extract three of the most important quantities; temperature, mole fraction, and pressure.

9 Results

When designing new diagnostic tools, one of the most important questions that needs to be addressed is: “How good are the results?” If the accuracy and precision of a new tool is unknown, the overall capability of the diagnostic is unknown, and the results will be suspect. Several plots have already been presented which show absorption spectra can be measured and then converted into temperature and mole fraction (Figures 2-1, 2-7, 5-3, and 8-7). This chapter will present additional results, but more importantly, will address the quality of the results. The results will first be checked to see if they pass basic common sense tests (“Reality Checks”). They will also be compared to thermodynamic calculations (ideal gas, polytropic coefficients). The precision of the results, and absolute accuracy experiments and results will then be presented.

9.1 Reality Check

Figure 9-1 provides a set of the measured results from the HCCI engine experiment. The details of obtaining the spectra are described in Chapter 5, and the method for calculation temperature and mole fraction are discussed in Chapter 8. These results were measured to study a practical problem (determining the cold combustion limits of HCCI), which is presented in the next chapter.

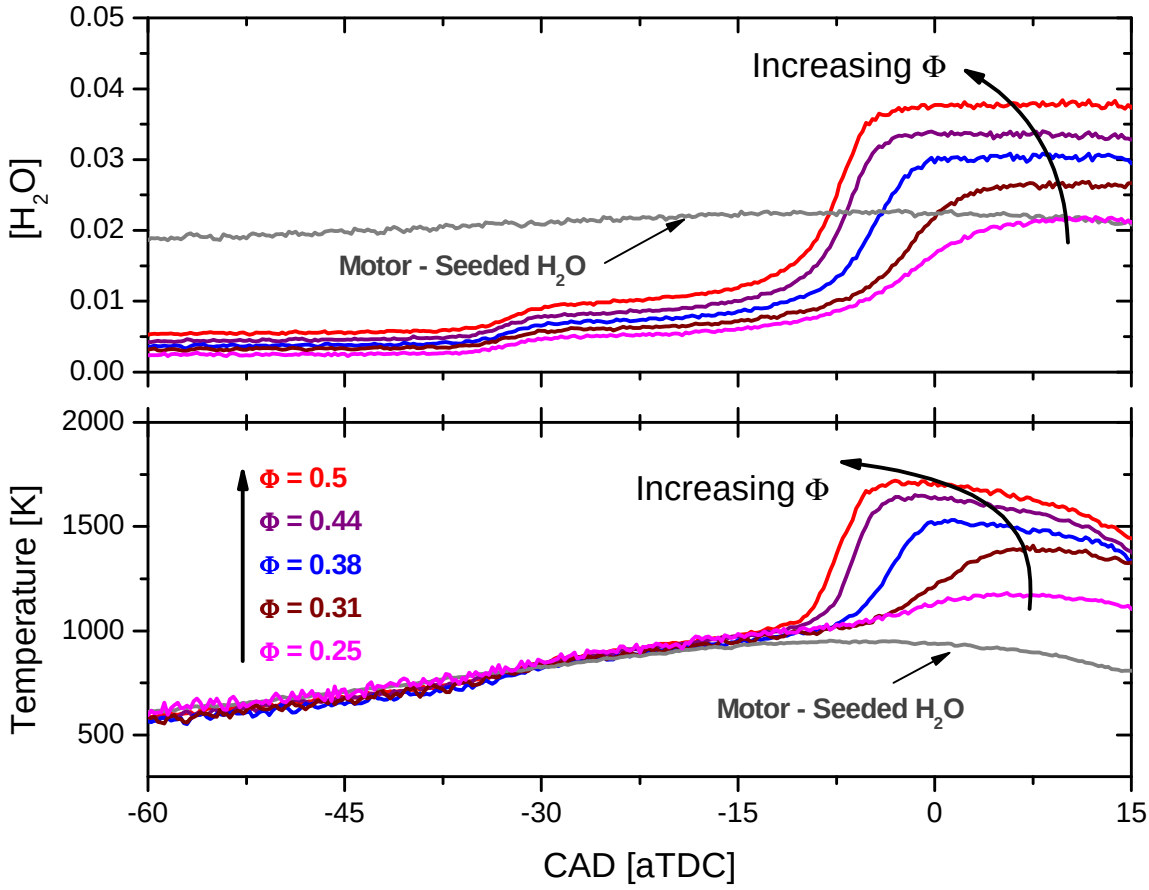

Figure 9-1 – *Bottom panel*: Measured temperature versus crank angle in a firing HCCI engine, seeded with 50% argon diluent at various equivalence ratios (50 absorption spectra averaged cycle-to-cycle). *Top Panel*: Corresponding H_2O mole fraction results.

Generally, the results in Figure 9-1 make physical sense. HCCI is known to have two stages of combustion, which is easily observed in the mole fraction plot. Peak temperatures and final H_2O mole fraction results are expected to increase with increasing equivalence ratios. Equivalence ratio is described by the following equation:

$$\Phi = \frac{\left(F/A\right)_{Actual}}{\left(F/A\right)_{Stoich.}} \qquad 9.1\text{-}1$$

In this equation, *F/A* stands for the ratio of fuel to air (by mass), and therefore equivalence ratio indicates how lean (< 1) or rich (> 1) the combustion is compared to stoichiometry. Increasing equivalence ratios will also cause the second stage of combustion to occur earlier in the engine the cycle. As equivalence ratios increase, there would also be more H_2O vapor present in the naturally occurring the exhaust gas recirculation (EGR). This can be observed in pre-combustion (-60 to -30 CAD aTDC) H_2O mole fraction results. Finally, the motoring results generally follow the firing results before the start of combustion.

Figure 9-1 passes these most basic tests, but that is only the tip of the iceberg when it comes to assessing the capabilities of the diagnostic. Figure 9-2 provides more details of one of the cases ($\Phi = 0.38$) from Figure 9-1. In addition to the calculated temperature and mole fraction, pressure measured from the pressure transducer and a calculated heat release rate is presented. The equation for calculating heat release rate is:

$$\frac{dQ_{HR}}{d\Theta} = \frac{1}{\gamma - 1} \forall \frac{dP}{d\Theta} + \frac{\gamma}{\gamma - 1} \left(P_{firing} - P_{motoring} \right) \frac{d\forall}{d\Theta} \qquad 9.1\text{-}2$$

where Θ represents crank angle degrees, $\forall$ is volume, γ is ratio of specific heat. The code used to calculate heat release rates as a function of crank angle were written by Professor Ghandhi, details can be found here [45]. Additional quantities that define how well the engine was operating are also listed. Indicated Mean Effective Pressure (IMEP) for this case was 28.22 kPa, the coefficient of variation (COV) of the IMEP is 0.0845, and the peak pressure (PP) is 2828.06 kPa. IMEP is the ideal average pressure that the engine can output, and the COV of IMEP describes how much variability there is on a cycle to cycle basis. These values are taken from an average of 100 cycles, and are recorded after the absorption measurements were obtained. The

"X ideal" quantity is the mole fraction calculated for ideal combustion, and "X emission" is the mole fraction that was measured from the exhaust gas. The X emission measurement was performed at the same engine conditions, but separately from the absorption spectroscopy measurements. The mole fraction results from the absorption spectroscopy measurements generally are close to the X emission results.

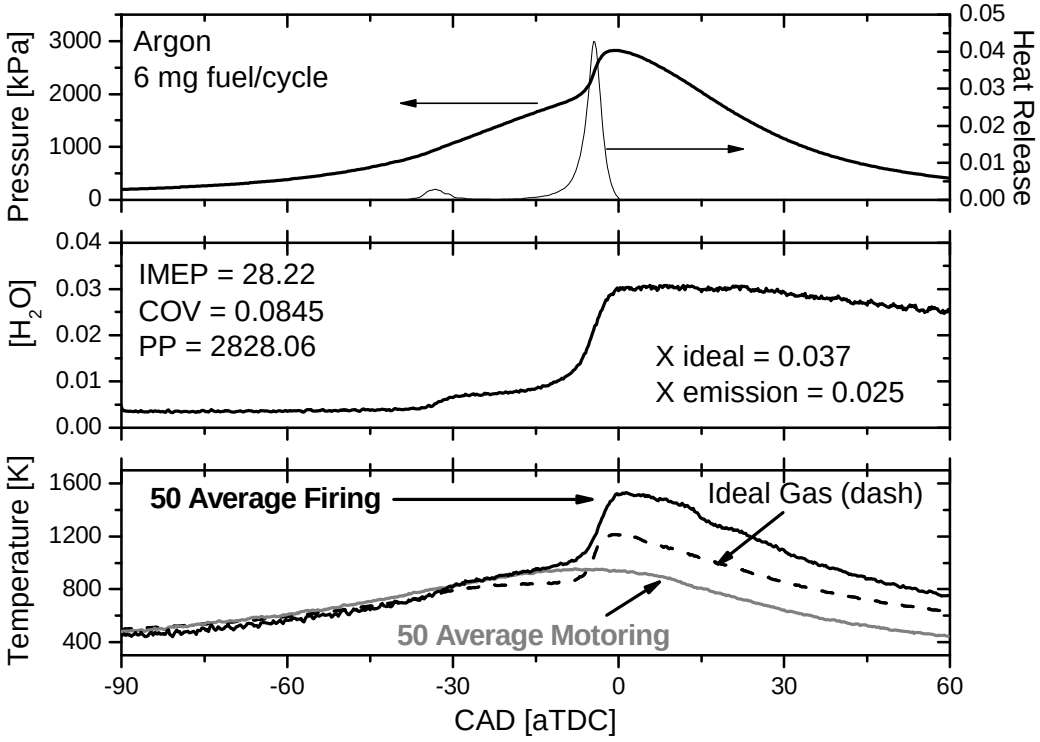

Figure 9-2 – Summary of results for the Φ = 0.38 (6 mg fuel/cycle), 50% argon diluent case. The bottom panel provides absorption spectroscopy firing (black), motoring (grey), and ideal gas (dashed line) temperatures. The center panel shows H_2O mole fraction, and various engine quantities measured external to the optical experiment. The top panel shows the pressure as measured by the transducer, and a calculation of heat release.

9.1.1 Ideal Gas

Figure 9-2 also plots the ideal gas temperature (dashed line). Ideal gas temperature (T_{IG}) is calculated from the following equation:

$$T_{IG} = \frac{P\forall}{n\Re} \qquad 9.1\text{-}3$$

Pressure (P), volume ($\forall$), and the universal gas constant ($\Re$) are either measured or known, however n, the number of moles, is unknown. To set the number of moles, T_{IG} is equated to the temperature measured from absorption spectroscopy (T_{ABS}) at some point before combustion. This calculated n is then used as a constant throughout the T_{IG} calculations. The point at which the temperatures are equated was chosen right before the first stage of combustion. For example, in Figure 9-2, the first stage of combustion occurs at -36 CAD aTDC, which is where T_{IG} equals T_{ABS}.

Similar graphs to Figure 9-2 for all of the engine conditions that were tested can be found in Appendix I. All of these figures (including Figure 9-2) show T_{IG} lower than T_{ABS}, but otherwise follow the correct behavior. This can be explained by realizing that significant blow-by is occurring in the engine. Blow-by means that gas is leaving the engine. If blow-by is occurring, then the n calculated by $T_{IG} = T_{ABS}$ (before combustion) would be greater than the actual n. If the n being used in Eqn. 9.1-3 is too big, then the calculated T_{IG} would be too low. Therefore, the ideal gas results in Figure 9-2 and Appendix I continue to support the idea that the results from the wavelength-agile absorption spectroscopy diagnostic tool can pass basic tests. This assumes that the measured P and $\forall$ are well known and accurate, which is a fair assumption since the pressure transducer has been repeatedly calibrated with a dead-weight tester, and the volume is a

function of the known geometry of the engine. These results still do not answer the question of absolute accuracy, but they are useful as a first check.

9.1.2 Polytropic Coefficient

Aside from ideal gas, another parameter that can check the temperature results in an engine is the polytropic coefficient (γ). During isentropic, adiabatic conditions, PV^{γ} is constant. Plotting log P versus log V, γ will be the slope of the isentropic, adiabatic line. One can also use a log P versus log T_{ABS} to determine γ. In this case, $[\gamma / (\gamma-1)]$ is the slope of the log P - log T_{ABS} plot. Calculating γ from both plots can therefore provide another check for the T_{ABS} measurements. This assumes that the measured P and V are well known and accurate, just as in the ideal gas measurements.

Figure 9-3 and Figure 9-4 are examples of using this concept to check T_{ABS} measurements. In Figure 9-3, the agreement between γ calculated from the PV compared to the PT_{ABS} plot is excellent (1.38 compared to 1.381). On the other hand, Figure 9-4 has poor agreement (1.36 compared to 1.47). The adiabatic, isentropic zones were chosen during the compression stroke, from the start of the measurements until just before the start of the initial combustion.

Small variations in γ represent large errors in temperature, therefore getting these measurements correct is not trivial. This is a difficult test for the diagnostic to pass. Similar graphs to Figure 9-3 and Figure 9-4 for all of the engine conditions that were tested can be found in Appendix II. It can be seen that sometimes the results for this test are great and other times not good. The main indication therefore is that further studies must be done to determine absolute accuracy.

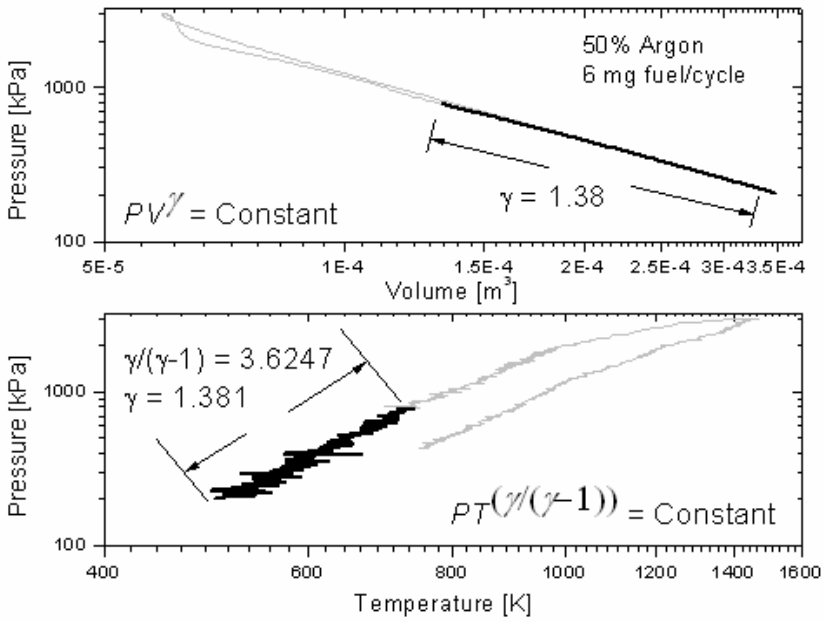

Figure 9-3 – *Lower panel*: Log *P* versus log T_{ABS} for Φ = 0.38 case. Upper panel: Log *P* versus log ~~V~~ .

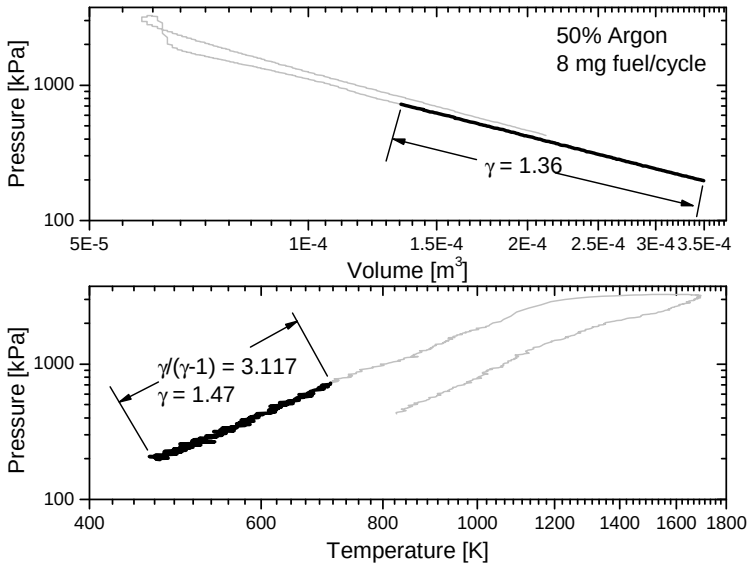

Figure 9-4 – *Lower panel*: Log *P* versus log T_{ABS} for Φ = 0.5 case. *Upper panel*: Log *P* versus log ~~V~~ .

9.1.3 Motoring Conditions

Motoring conditions were also monitored. For the experiment described in the next chapter, intake gas was seeded with Argon or CO_2 diluents to adjust the specific energy of the gas. Figure 9-5 shows the results of the motoring cases with these diluents, as well as 100% intake air. H_2O was seeded into the intake gas since there was not sufficient H_2O normally from the intake air, and one unseeded motoring condition in which the intake air was taken from a vent to the room. A pressure cooker was used to deliver the seeded vapor. Although the system was designed to give a constant flow rate of H_2O into the intake gas, leakage was clearly visible, and therefore did not allow this test to be a quantitative measure of mole fraction accuracy. It is interesting to note however that the average mole fraction of the test that was vented into the room air (the thin line) was within 5% of the humidity for that day. The reason that the measured mole fraction is not constant throughout the engine cycle will be discussed in the next section.

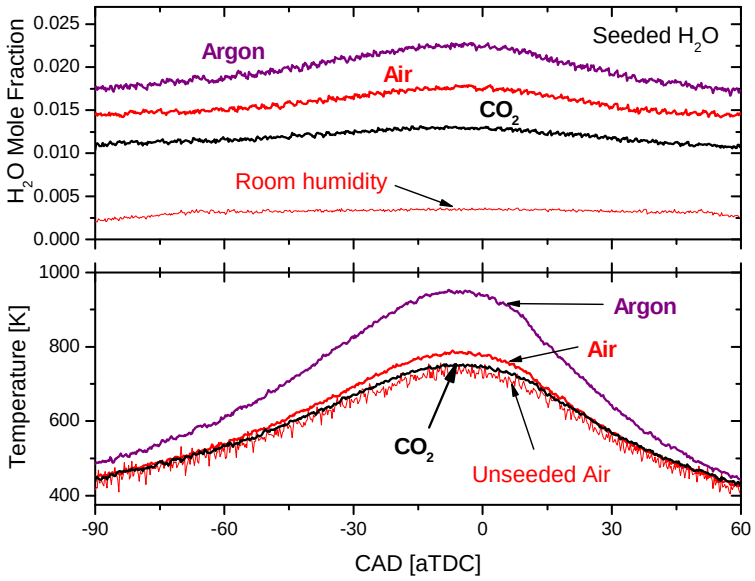

Figure 9-5 – Motoring temperature and mole fraction results. The thick lines have H_2O seeded into the intake gas. The thin lines have a vent to room air open into the intake gas.

9.2 Precision

The precision of temperature and H_2O mole fraction measurements is easily assessed. A measurement every 0.25 CAD is recorded and the precision is immediately visible as high-pitch scatter in the data. For example, consider Figure 9-6. The calculated temperature of a random single engine cycle measurement was plotted versus crank angle along with the results from the average of 50 cycles. As expected, precision improves with averaging. To quantify the amount of scatter, a running average of 5 points is calculated. The peak-to-peak (P-P) variation of each individual temperature measurement (both the averaged and single cycle) is then recorded, and plotted in the bottom panel of Figure 9-6. The precision of a single cycle temperature measurement is approximately 5% P-P in the high pressure, high concentration region (around TDC), and significantly worse before -30^o aTDC because of low H_2O content (~20% P-P). Averaging 50 spectra produces precisions better than 2% P-P, even in the low-water-content portion preceding -30^o aTDC. After combustion, when there is high water concentration, temperature precision is as good as 0.1% P-P.

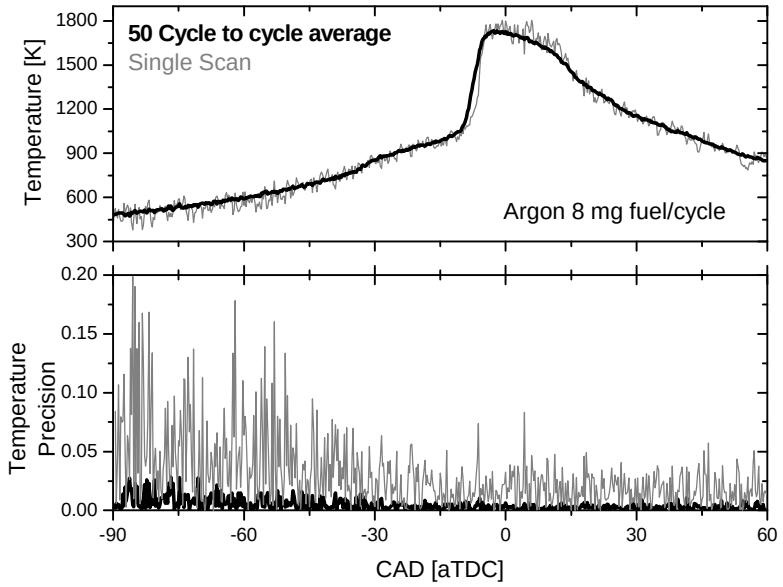

Figure 9-6 – Comparison of a single scan (grey) and 50 cycle-to-cycle phase locked average (black) temperature calculations. *Top panel*: Temperature versus crank angle degrees. *Bottom panel*: Precision of temperature measurements based on a running average.

Figure 9-7 summarizes the precision of the water mole fraction results. Before and after combustion, the average value for the single scan was taken as the running average of the averaged results, since those values should be constant, during combustion, a running average was used. At worst (low pressure and concentration), the precision is ~30% P-P in the single cycle and 5% in the averaged results. At best (high pressure, high concentration), the precision is 7% P-P in the single cycle and 2.5% P-P in the averaged results. The reason for the increased scatter after combustion will be discussed next.

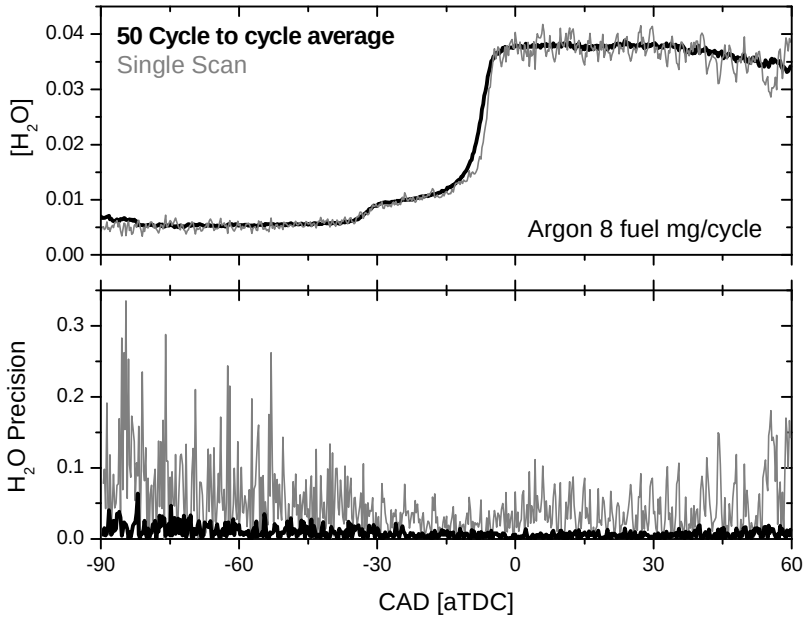

Figure 9-7 – Comparison of a single scan (grey) and 50 cycle-to-cycle phase locked average (black) H_2O mole fraction calculations. *Top panel*: Mole fraction versus crank angle degrees. *Bottom panel*: Precision of mole fraction measurements based on a running average.

Figure 9-8 shows 2 absorbance spectra used to calculate the results of Figure 9-6 and Figure 9-7. The FDML can have either excellent spectral resolution (better than 0.05 nm) for a small range, or average resolution for the entire scan (~0.1 nm). It was determined that it is better to optimize the entire laser scan at 0.1 nm resolution rather than one section of the scan with excellent resolution. Figure 9-8 highlights the issues that remain with the FDML. The signal-to-noise level is about 2 in the low pressure, low concentration single scan measurement (bottom panel), slightly better when more water is present (top panel).

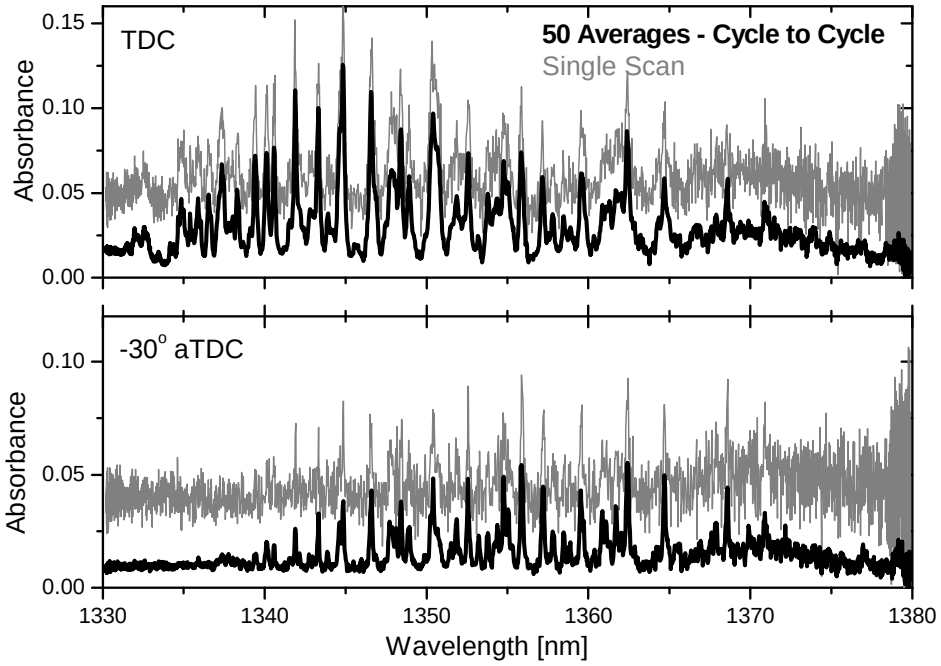

Figure 9-8 – *Top panel*: Absorbance measurements taken at top dead center used to calculate the results from Figure 9-6 and Figure 9-7. *Bottom panel*: Absorbance measurements taken at -30 CAD aTDC. Grey lines are from single scan measurements, black lines are phase locked 50 cycle-to-cycle averages.

There are two main issues with the mole fraction. First, the averaged results show the mole fraction decreasing after combustion and before the exhaust valve is open. The amount of water after combustion should remain a constant. The other issue is that there is an unacceptable amount of fluctuation in the single scan results. One hypothesis that would explain both problems is that the FDML laser is randomly skipping wavelengths within a scan, similar to the mode-hopping that was evident in the first generation ECDL. This has been observed by looking at all of the absorbance spectra at a particular crank angle. Skipping wavelengths will cause feature strengths to be either eliminated or weakened, thus causing the overall mole fraction to

appear to be decreasing in the averaged results, as well as playing havoc on the individual results. Figure 9-9 shows 5 scans from one of the lower equivalence ratio conditions (50% argon diluent, Φ = 0.31). The circles on the figure represent places where mode-hopping likely occurred, since features are either missing or significantly shorter in absorption strength (meaning the mode hop occurred near the absorption feature).

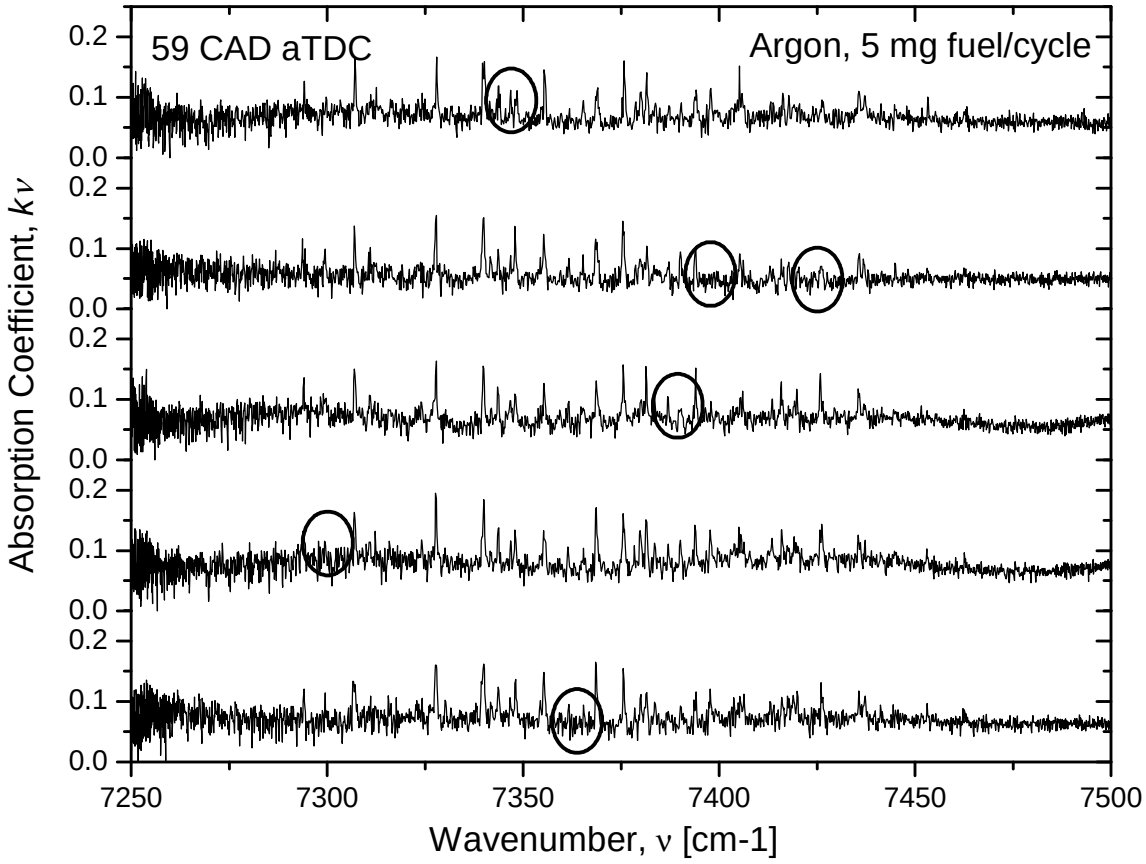

Figure 9-9 – Absorption spectra from 5 individual laser scans (no averages), all taken at 59 CAD aTDC. Circles highlight areas where a mode-hop likely occurred.

9.3 Experiments to Quantify Temperature Accuracy

Two methods for quantifying absolute accuracy are presented. Chapter 5 introduced the experimental setups and issues associated with the shock tube and combustor rig experiments. The following sections present the results of these experiments as they pertain to quantifying the absolute accuracy of wavelength-agile absorption spectroscopy measurements.

9.3.1 Shock Tube

Initial experiments performed in the Wisconsin Shock Tube Laboratory (WiSTL) [48] aimed at assessing sensor accuracy are reported. These measurements essentially form a global check on the accuracy of the HITEMP database in the R-branch of $\nu_1 + \nu_3$ H_2O band. Spectra were measured 15 cm from the end wall of the tube, allowing measurements behind the incident as well as the reflected shock. A Mach 2.46 and mach 1.25 shocks were propagated into low pressure (97.5 kPa) air containing ambient humidity. The theoretical (shock relations) and measured (wavelength-agile thermometer: 30-scan average) temperatures behind the incident M=2.46 shock were 628.04 K and 637.2 K, indicating a measurement bias of **+1.4%**. Behind the reflected (2.46) shock, the theoretical and measured temperatures were 1026.15 K and 1002.1 K respectively, indicating a measurement bias of **-2.2%**. The theoretical and measured temperatures behind the incident M = 1.25 shock were 348 K and 339.2 K respectively, indicating a measurement bias of **+2.5%**. Behind the reflected 1.25 shock, the theoretical and measured temperatures were 408 K and 422.6 K respectively, indicating a measurement bias of +**3.6%**. Figure 9-10 shows the temperature results of the shock tube experiment. Additional experiments of this kind will be required to fully assess the accuracy of the wavelength-agile thermometer, but these initial data points suggest that accuracy is acceptable for many applications at least up to ~ 1000 K.

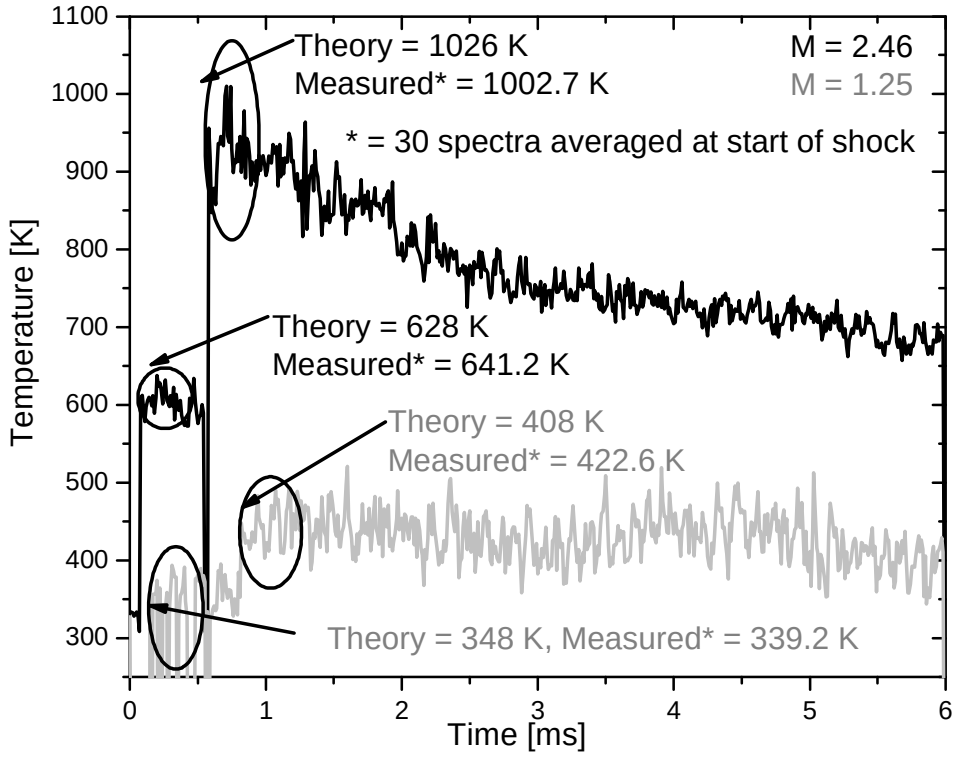

Figure 9-10 – Results from non-averaged spectra measured in during an M=2.46 and M=1.25 shock. 30 consecutive spectra beginning as the shock passed the laser path (in both the primary and reflected cases) were averaged to produce results within ±2% absolute accuracy.

9.3.2 Gas Turbine Combustor Rig

Measurements were made for a 3x3 matrix of combustor conditions. The equivalence ratios tested were approximately 0.22, 0.27, and 0.32. The pressures in the combusting section were 340, 520, and 690 kPa. The fuel used was JP-8. At each condition, 1000 signals were first averaged then converted to absorbance using the Beer-Lambert law. As mentioned in Chapter 5, this is a convenient experiment because it runs at steady conditions, therefore heavy averaging can be employed; however, segregated zones cause added complexity to calculations.

The top panel of Figure 9-11 shows the raw measured spectrum for the Φ = 0.220, P = 696 kPa case. The path for the room air totaled 25 cm. An absorption spectrum for H_2O at 322 K and 0.014 H_2O mole fraction (corresponding to 54% relative humidity at room temperature, measured that day) along a 25-cm path was calculated and subtracted from the measured spectra. The middle panel shows the spectrum that results when the raw spectrum is corrected by subtracting out the room-H_2O spectrum. The bottom panel shows the HITEMP spectrum for the corresponding flame temperature (1277 K, 696 kPa).

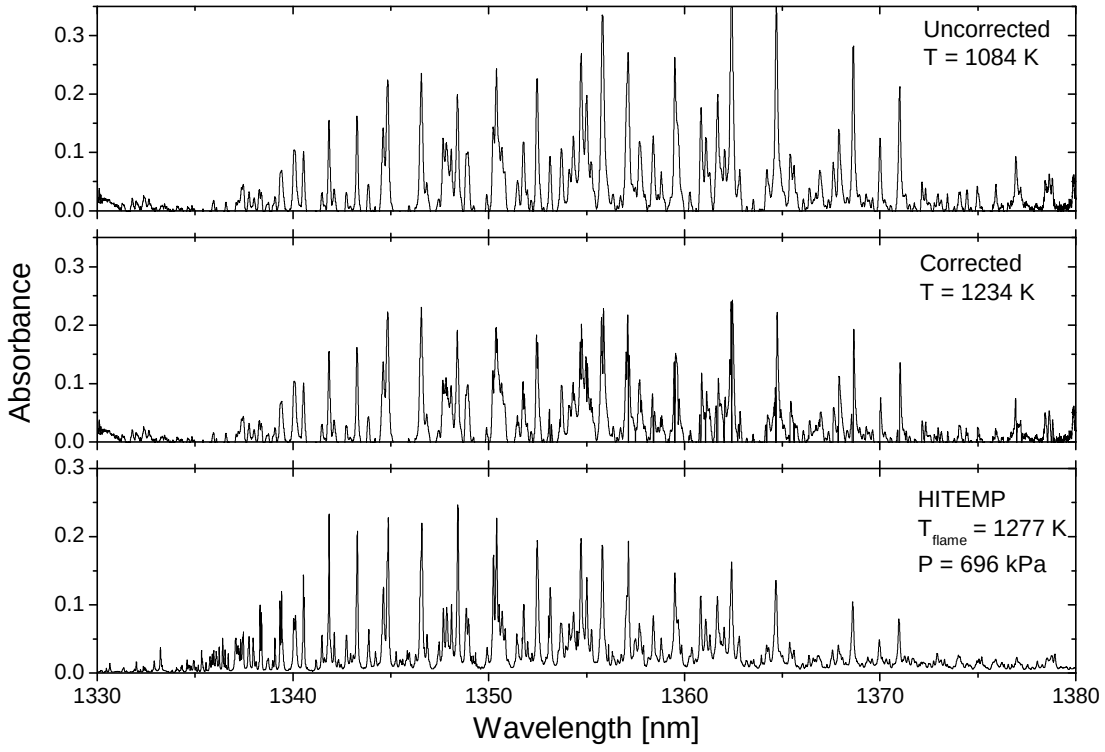

Figure 9-11: Raw measured spectrum (top panel), corrected spectrum (middle panel), and corresponding HITEMP spectrum (bottom panel) at the theoretical flame temperature for the Φ = 0.220, P = 696 kPa case. The indicated temperatures in the top and middle panel are calculated from the plotted spectrum.

Figure 9-12 shows the temperatures from the raw data (in red) as a function of the measured equivalence ratio. The grey symbols are the calculated flame temperatures based on sampled gas analysis. The measured temperatures are expected to be slightly lower than the calculated temperatures since the laser was mounted downstream from the hottest part of the combustion chamber; however, the measured values in Figure 9-12 are unacceptably low due to the room-air contribution.

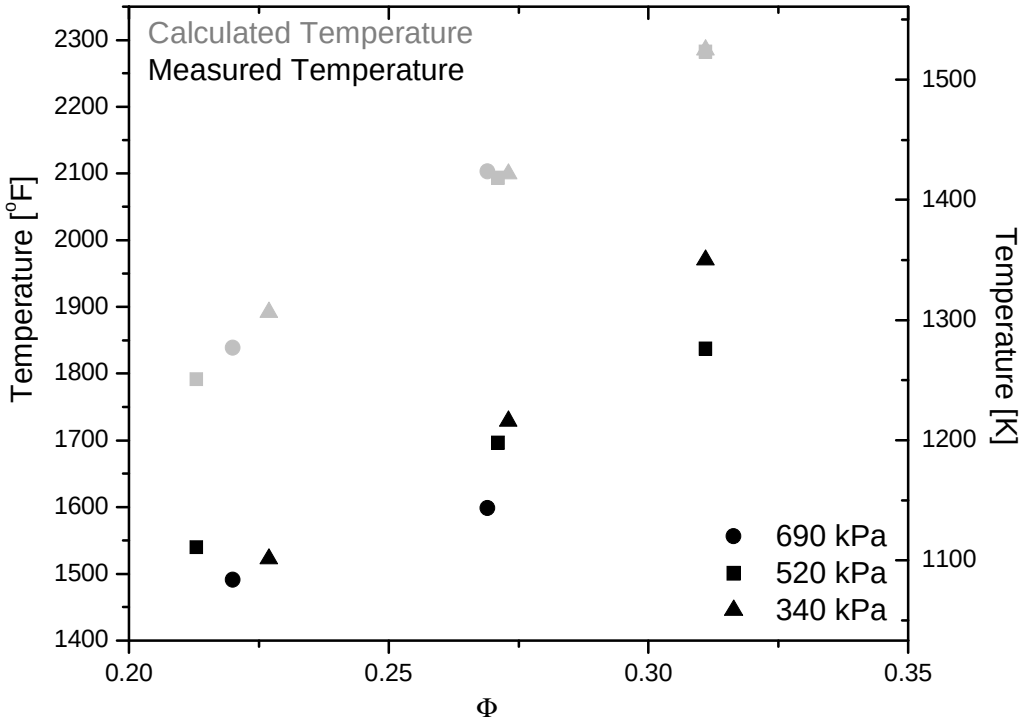

Figure 9-12 – Uncorrected results which include room and warm air.

Figure 9-13 shows the results after subtraction of this room-H_2O spectrum (as described above). In fact, the actual room-air temperature in the vicinity of the experiment is slightly higher than room temperature because the combustor test rig warms the surroundings, therefore the

subtracted spectrum was simulate at 322 K. Future measurements should purge from the lines of sight between the laser and test section and between the test section and detector. Error bars based on the shock tube experiment are drawn on for reference.

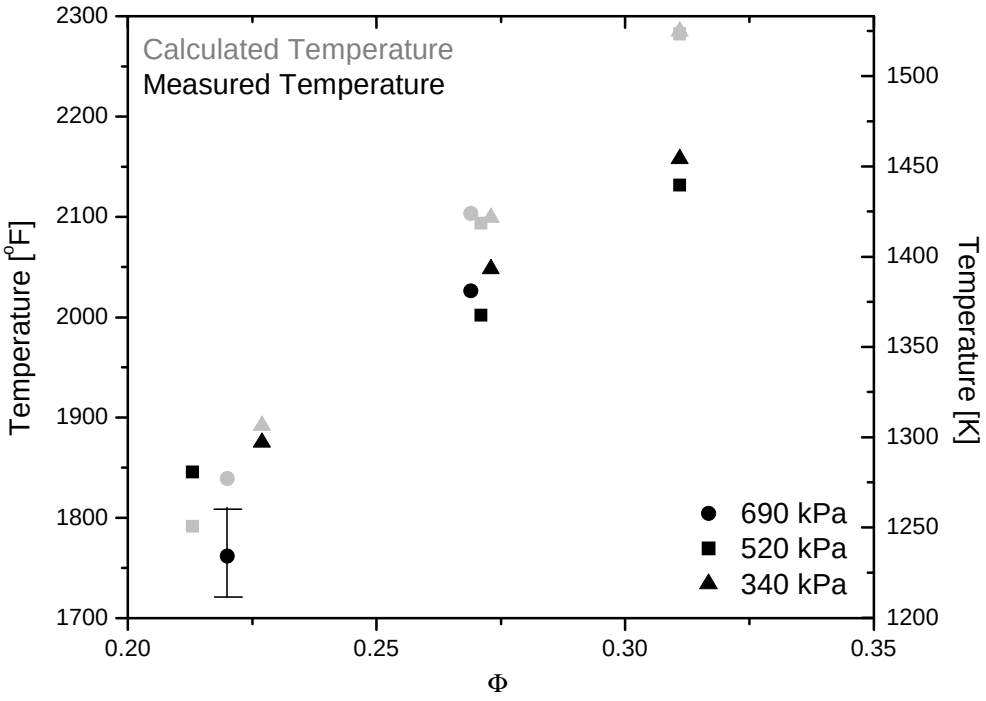

Figure 9-13 – Corrected results where room-air spectrum has been subtracted from measured spectra. The error bar for the lowest temperature point represents the best estimate of uncertainty (±2%).

9.4 High Temperature Accuracy Discussion

Section 9.1 highlighted the need to quantify the absolute accuracy of this diagnostic tool. Section 9.3 discussed two experiments that attempted to accomplish this need. Figure 9-14 summarizes the temperature results from section 9.3. The temperatures calculated from theory are on the x-axis, and the results from absorption spectroscopy measurements are on the y-axis. Generally, it can be observed that temperature accuracies are better at lower temperatures (as

calculated above, ~3% absolute accuracy), and above 1000 K, the measurements become biased too low.

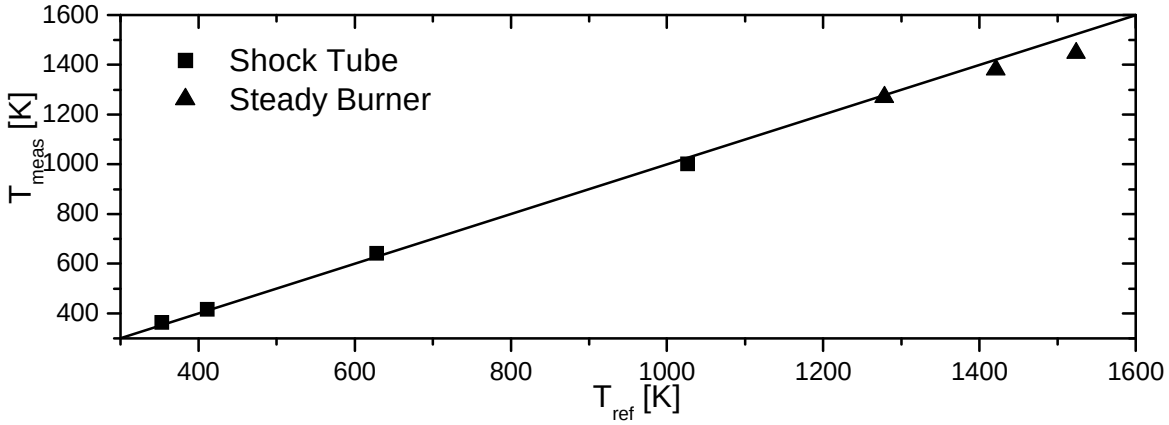

Figure 9-14 – Reference temperatures (based on calculations) compared to temperature measurements from wavelength-agile absorption spectroscopy.

The application of this diagnostic is high temperature combustion measurements; therefore, these inaccuracies must be addressed. There are two explanations to why the results are poor at higher temperatures. One is that the measurements are wrong, and the other is that the reference spectra that the measurements are being compared to are wrong. I have attempted to prove throughout this thesis that measurements were taken carefully, harsh environmental issues were taken into consideration, and the best possible wavelength-agile laser source has been used. This is not to say wavelength-agile sources will not improve, and improved spectra will not ever be measured. The spectra were however obtained with careful consideration of many possible sources of error.

9.4.1 Database Considerations

As mentioned in Chapter 8, the database that creates the spectra that the measured spectra are compared to is HITEMP. HITEMP is a specialized high temperature derivation from the more

popular HITRAN database. HITRAN is updated more often; however, it leaves out many absorption features that are important at high temperatures, which is where HITEMP comes into play. In general, both HITRAN and HITEMP get basic quantum parameters (*S*, *E"*, *etc*.) from experimental results, and then derive further parameters from quantum theory. HITRAN and HITEMP are known to contain errors [19, 20, 71-73].

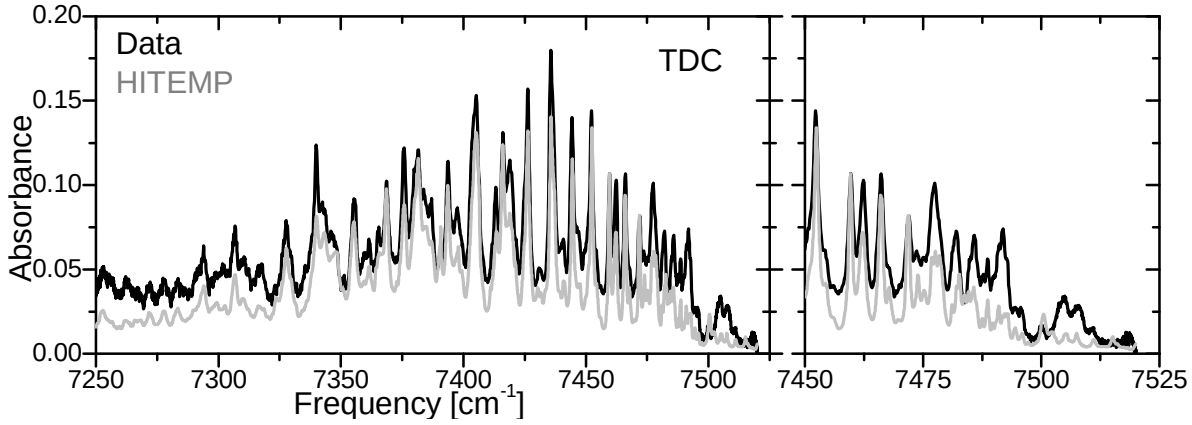

Figure 9-15 – *Left panel*: Measured absorption spectrum (black) taken at TDC in a firing engine (Φ = 0.605), compared to a corresponding HITEMP simulation at the best fit conditions (31.4 atm, 1511 K). *Right panel*: Zoomed in section of problem area.

Figure 9-15 plots the measured spectrum of the highest equivalence ratio (Φ = 0.605), at top dead center. This set of data should therefore contain the basically the hottest measured data from the FDML source. The best fit HITEMP spectrum is also plotted in Figure 9-15. Overall, the left panel seems to have reasonable agreement between the reference and measured spectrum. The right panel zooms into the features that are critical at hotter temperatures (absorption features near the band center are considered "hot lines"). There are rather significant differences

in this section, which may be one of the reasons that the measured spectra are returning temperatures too low.

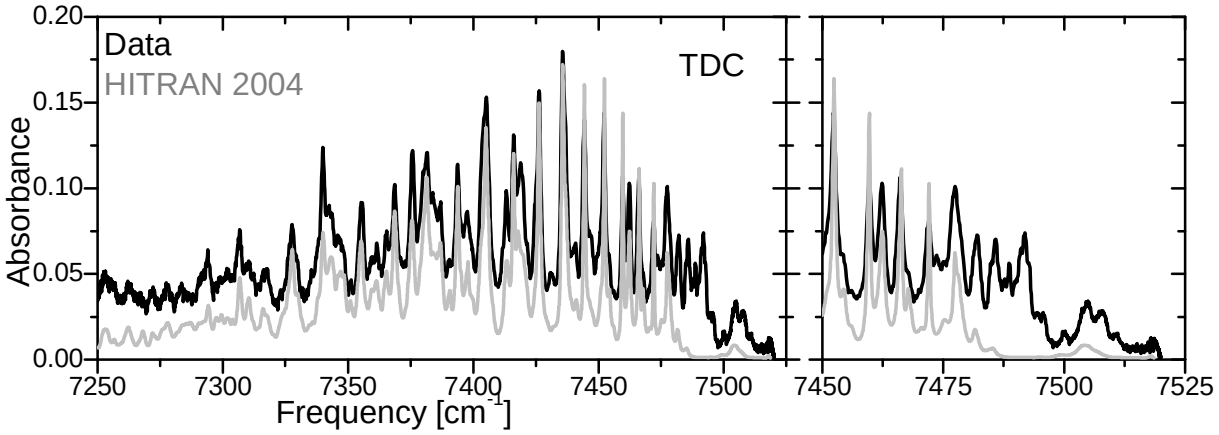

Figure 9-16 – *Left panel*: Measured absorption spectrum (black) taken at TDC in a firing engine (Φ = 0.605), compared to a corresponding HITRAN 2004 simulation at the best fit conditions (31.4 atm, 1511 K). *Right panel*: Zoomed in section of problem area.

Figure 9-16 plots the same measured spectra as Figure 9-15 with a HITRAN 2004 spectrum instead of HITEMP. This is included for two reasons. One is that HITRAN 2004 has been updated more recently than HITEMP. If there were corrected lines from HITEMP to HITRAN 2004, this plot would highlight the need to update the database created for this project. The other reason is to emphasize the need to use HITEMP. It is evident that HITRAN does indeed eliminate crucial spectroscopic parameters in the high temperature regions.

Very recently, a water spectroscopic database has been released that is created completely from theoretical simulations, no experimental parameters are included [76, 77]. This database is

called BT2. BT2 provides similar spectroscopic parameters as HITEMP and HITRAN, with a notable exception of the broadening coefficients. By estimating a broadening coefficient based on the measured data, the spectrum in Figure 9-17 was created. Based on the zoomed in section in the right panel, it would appear that the measured data has a better agreement to the BT2 database compared to HITEMP.

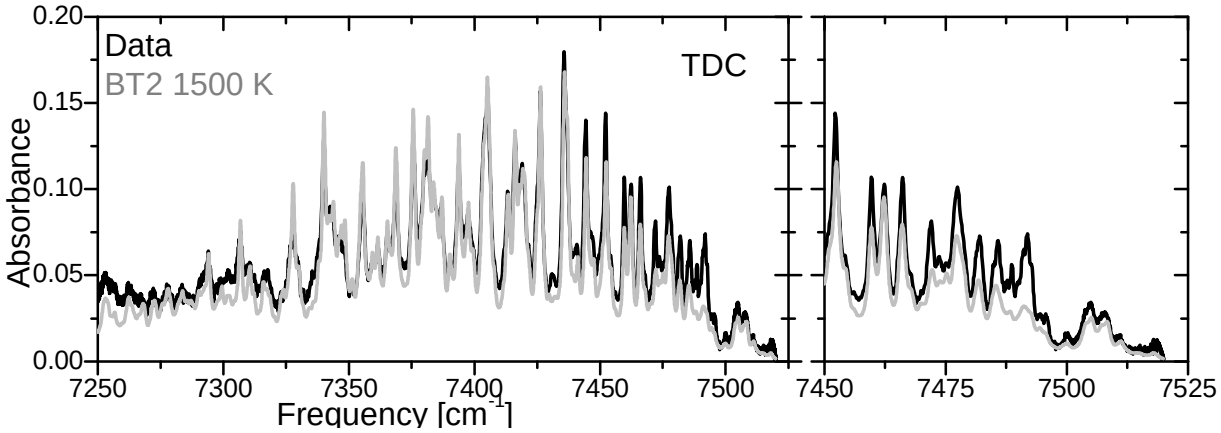

Figure 9-17 – *Left panel*: Measured absorption spectrum (black) taken at TDC in a firing engine (Φ = 0.605), compared to a corresponding BT2 simulation near the best fit conditions (1511 K). *Right panel*: Zoomed in section of problem area.

Since the calculated temperatures from HITEMP have been shown to produce results that are too cold, another hotter spectrum was created from the BT2 database. Figure 9-18 shows the same data plotted with a 2200 K spectrum from BT2. The spectrum in Figure 9-18 has the best overall fit to the data compared to any of the previous figures, further implying that our results are currently biased cold.

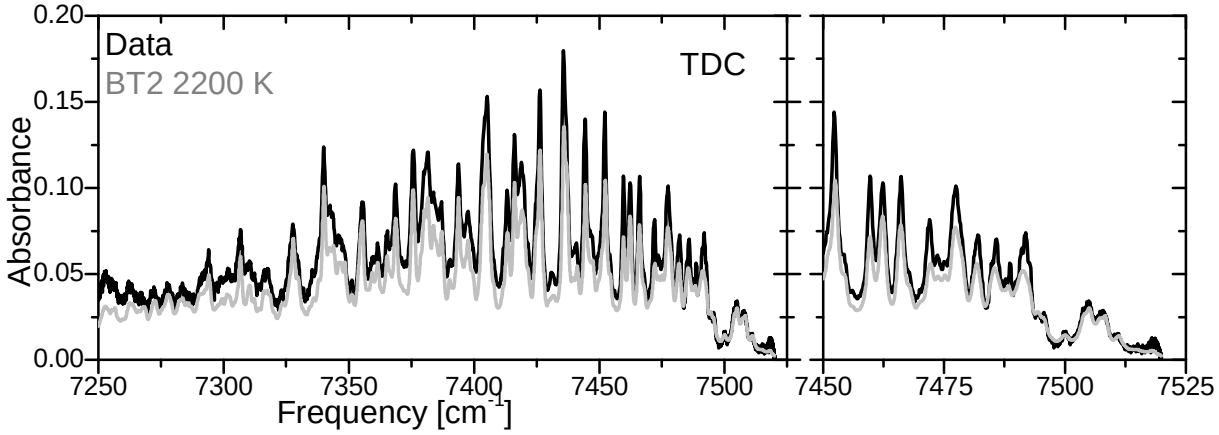

Figure 9-18 - *Left panel*: Measured absorption spectrum (black) taken at TDC in a firing engine (Φ = 0.605), compared to a corresponding BT2 simulation at 2200 K. *Right panel*: Zoomed in section of problem area.

The process of creating a new pre-compiled library of reference spectra (as highlighted in Chapter 8) is very time consuming and computationally expensive. A new library is being planned, and temperature results based on a BT2 database could be ready by early 2007. A minor issue will be how to include pressure broadening parameters. Two possibilities are to either use the parameters from HITEMP, or base the broadening off of the measured broadening. Both are currently being explored before the new pre-compiled library is simulated.

A small BT2 library was created to calculate temperature for the spectra measured in the gas turbine experiment. The spectra were simulated by Drew Caswell, using a FWHM of 1 cm^{-1}. In the tested range of the gas turbine, this was an acceptable estimation for the broadening parameter. The results are shown in Figure 9-19. The results are still not perfect, but they show that BT2 indeed calculates higher temperatures.

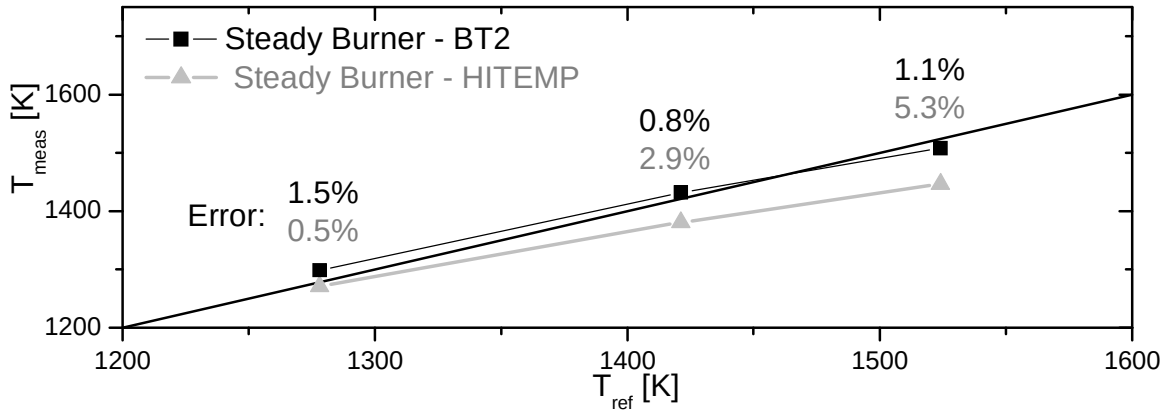

Figure 9-19– Comparison of HITEMP (triangle) and BT2 (square) calculations of temperature. Reference temperatures (based on calculations) compared to temperature measurements from wavelength-agile absorption spectroscopy.

9.4.2 Experimental Verification

Aside from relying on other groups to create the databases that will ultimately determine the accuracy of our measurements, there are also plans to independently verify the spectroscopic library. H_2O is a nice molecule to measure during combustion because it is almost always present. It is a complicated molecule however when it comes to predicting the quantum behavior (hence, BT2, a completely numerical simulation is just being released in 2006). OH on the other hand, is much better understood. Dr. Sanders has plans to simultaneously measure high resolution OH absorption spectra, as well as H_2O spectra from the FDML laser in the HCCI engine. OH will only be present right around combustion, but that will still provide important high temperature known conditions. We will be able to extend the line in Figure 9-14 to approximately 2000 K. Once high temperatures are known with measured H_2O spectra, we can begin creating our own reference library. A simple solution will be to create a calibration curve

for our measurements. A more complicated, but more complete, solution will be to adjust the parameters from HITEMP, and create additional absorption lines based on the measurements.

Independent experimental verification of absolute accuracy is important for development of any diagnostic tool. This will most likely be a major emphasis in the Sander's research group for the next several years. This chapter introduced some basic concepts for accuracy studies, but also highlighted the need for additional work.

10 Practical Application: Low Temperature Limits for HCCI

This chapter provides an example of a practical application for wavelength-agile absorption spectroscopy measurements. Specifically, temperature measurements were taken to determine the low temperature limit for acceptable HCCI combustion. The transition from acceptable to unacceptable combustion is observed by a significant increase of CO in the exhaust gas. There is a hypothesis that this transition occurs purely as a function of a peak cylinder temperature, rather than a function of equivalence ratio.

An experiment from Dec and Sjöberg studied this low limit by varying the types of fuel to achieve different peak temperatures [78]. Another study confirmed the acceptable combustion limit to be a function of combustion temperature by observing measured OH absorption spectra in the cylinder [45], OH being a critical agent in the $CO \rightarrow CO_2$ reaction. This experiment expands on the OH study, and offers a quantitative measure of the low temperature limit of HCCI, independent of fuel type or equivalence ratio.

10.1 Method

The experiment was designed to study combustion as a function of peak temperature, independent of equivalence ratio. This was accomplished by adding diluents to the intake gas, altering the specific energy of the intake gas. Argon and CO_2 have specific heats lower and higher than air respectively. Adding argon diluent to the intake gas causes the combustion to reach the critical acceptable peak temperature at a lower fuel mass than 100% air. Alternatively, CO_2 causes the combustion to reach the critical acceptable peak temperature at a higher fuel mass than 100% air. To put it another way, if a constant amount of fuel was used, combustion

with the argon diluent would have the highest peak temperature, followed by combustion with 100% intake air, and finally combustion with CO_2 diluent would have the lowest peak temperatures.

A matrix of experimental conditions was tested in the HCCI Triptane engine. When diluents were added, intake gases were seeded with either 50% argon or 20% CO_2 by mass. Each condition was then tested with several amounts of fuel. At each condition, the CO in the exhaust gas was measured with a five-gas emission analyzer from Horiba Instruments, Inc.. Specifically, the CO was measured by Nondispersive Infrared analyzers [45]. The engine was run at 600 RPM with a 9.6:1 compression ratio.

10.2 Results

Figure 10-1 plots the CO as a function of the mass of the fuel for the three different intake conditions. CO is measured as EICO, standing for Emissions Index of CO. EICO is the measured mass flow rate of exhaust CO normalized by mass flow rate of fuel into the cylinder [45].

$$EICO = \frac{\dot{m}_{CO}}{\dot{m}_{fuel}} = \left[\frac{g_{CO}/s}{kg_{fuel}/s} \right] = \left[\frac{g_{CO}}{kg_{fuel}} \right] \qquad 10.1\text{-}1$$

Figure 10-1 shows that as fuel mass decrease, CO emissions increase. The transitions occur at different fuel masses depending on the diluent. From this figure, the critical conditions can be determined. 100% intake air with 9 mg fuel, 50% argon with 6 mg of fuel, and 20% CO_2 with 11 mg of fuel are all the lowest fueling conditions where combustion is still acceptable.

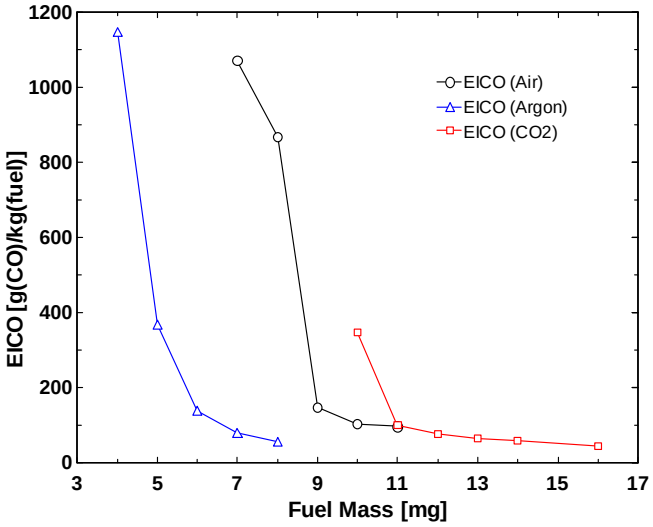

Figure 10-1 – Measured CO from exhaust gas as a function of the fuel mass per cycle.

Pressure and heat release data was recorded from the experiments used to create Figure 10-1. Wavelength-agile H_2O absorption spectroscopy experiments were performed at similar engine conditions as described throughout this thesis. These experiments took place several months after the emissions tests. Because of the extended time between tests, it was necessary to determine similar engine conditions by comparing heat release values. Appendix IV provides the specific data sets that were used to calibration the engine conditions from the CO emissions tests to the H_2O absorption tests.

Figure 10-2, Figure 10-3, and Figure 10-4 show the results of the H_2O absorption spectroscopy experiments. Peak temperatures for the critical conditions are summarized in Table 10-1.

Condition	Peak Temperature [K]
100% intake air, 9 mg fuel	1435
50% argon, 6 mg fuel	1400
20% CO_2, 11 mg of fuel	1521

Table 10-1 – Summary of peak temperatures at critical combustion conditions.

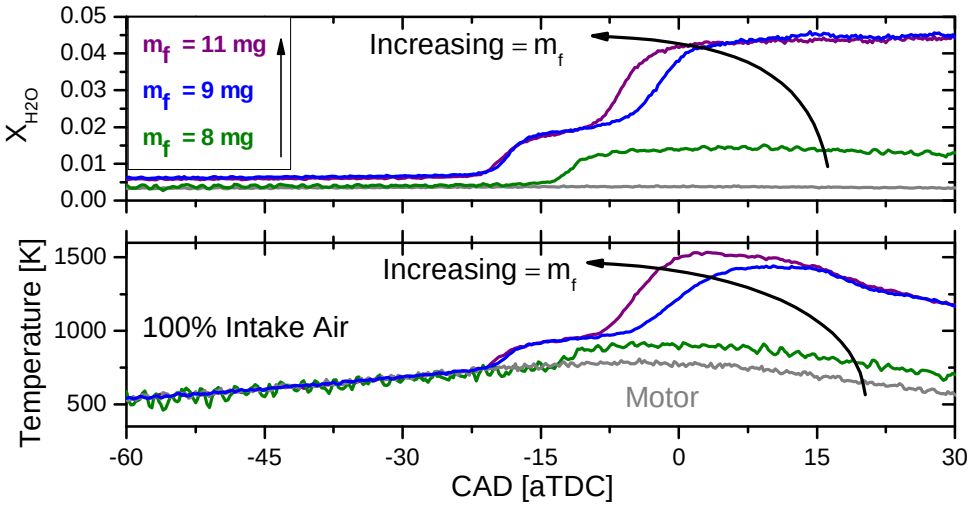

Figure 10-2 - *Bottom panel*: Measured temperature versus crank angle in a firing HCCI engine, with increasing amounts of fuel and no diluents added (50 absorption spectra averaged cycle-to-cycle). *Top Panel*: Corresponding H_2O mole fraction results.

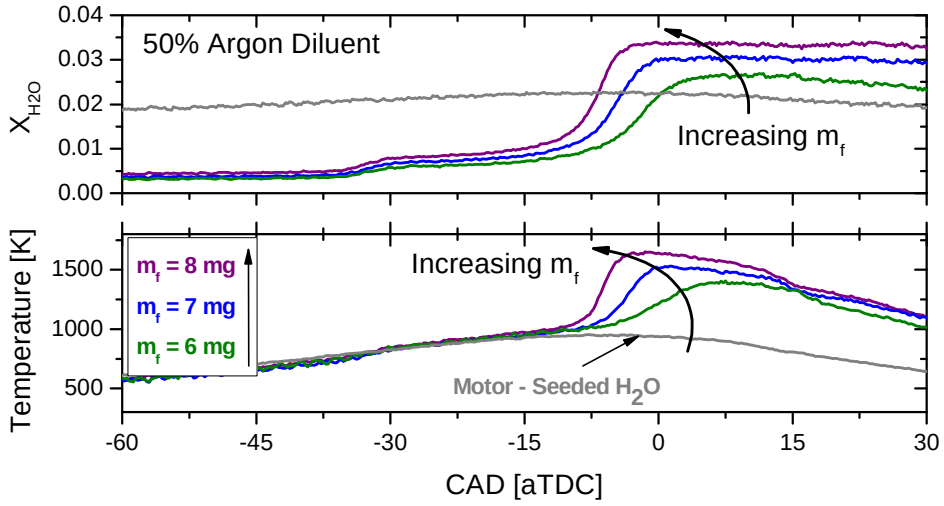

Figure 10-3 - *Bottom panel*: Measured temperature versus crank angle in a firing HCCI engine, seeded with 50% Argon diluent with increasing amounts of fuel (50 absorption spectra averaged cycle-to-cycle). *Top Panel*: Corresponding H_2O mole fraction results.

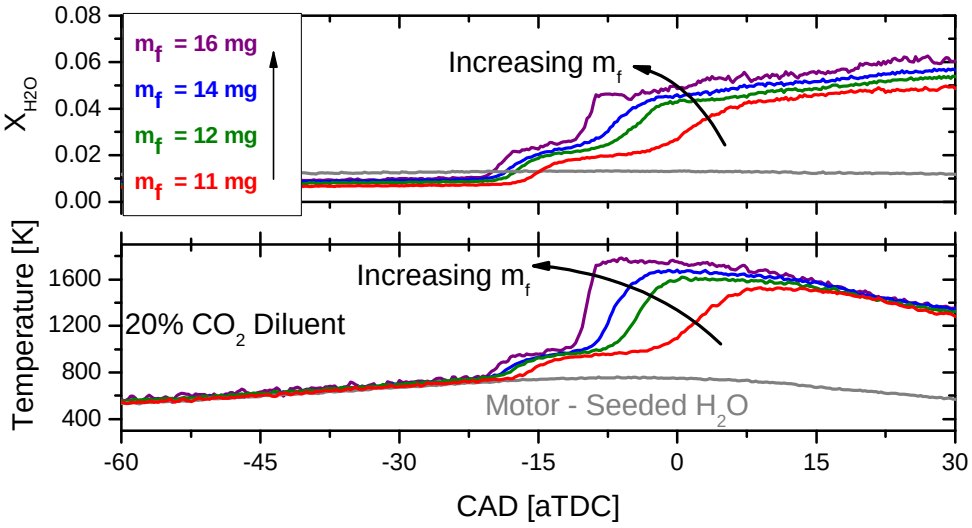

Figure 10-4 - *Bottom panel*: Measured temperature versus crank angle in a firing HCCI engine, seeded with 20% CO_2 diluent with increasing amounts of fuel (50 absorption spectra averaged cycle-to-cycle). *Top Panel*: Corresponding H_2O mole fraction results.

10.3 Conclusions

This section has described an experiment that could be useful for understanding an aspect of HCCI. Additionally, it highlights the potential of wavelength-agile absorption spectroscopy as a practical combustion diagnostic tool.

Dec and Sjöberg predicted that the low temperature limit for acceptable combustion was 1500 K for an engine operating at 1200 RPM and a 18:1 compression ratio [78]. The conditions in this experiment were 600 RPM and 9.6:1 compression ratio. The measured critical temperatures were mostly lower than expected (1400 K, 1435 K, and 1521 K), however this is consistent with the discussion in Chapter 9 stating that higher temperature tend to be calculated with a cold bias.

This experiment was performed over the span of several months. One of the issues was to confirm that the CO emission measurements were taken at consistent conditions as the H_2O absorption spectroscopy measurements. All of the measurements (CO emission gas and H_2O absorption) should be repeated once the engine is functional and the new BT2 database has been implemented. This will assure that consistent conditions are being compared. The new database should increase the value of the measured temperatures, and the results may match previously published results.

11 Conclusions

The goal of this project has been to obtain quantitative temperature and mole fraction measurements in harsh environments using wavelength-agile absorption spectroscopy. This concluding chapter summarizes the findings of this project and highlights some recommendations for future work.

11.1 Project Summary

This project has developed the necessary tools and methods to measure H_2O absorption spectra in harsh environments, and calculate temperature and mole fraction from the measured spectra. Various wavelength-agile sources were developed. The best performing wavelength-agile laser source for H_2O measurements to date is the Fourier-Domain Mode-Locking laser developed at MIT. Specific procedures were highlighted to best accommodate the measurements in the presence of beam steering and thermal emissions. A robust method to calculate temperature and absorber mole fraction was also developed.

Measurements were taken to quantify accuracy in a shock tube and steady burner (used to stimulate gas turbine conditions). Results from HCCI engine measurements demonstrated the precision of the measurements. Figure 11-1 summarizes the temperature results up to 1000 K (based on the accuracy measurements from the shock tube experiment). With no averaging, the measurements can be obtained in 5 μs. The difference in signal level as defined by Figure 11-1 is that at TDC, the engine contains significantly more water at higher pressures than at 90 CAD before TDC. The results from the shock tube contained about the same H_2O concentration as TDC conditions, therefore the accuracy results are only valid for high signal levels.

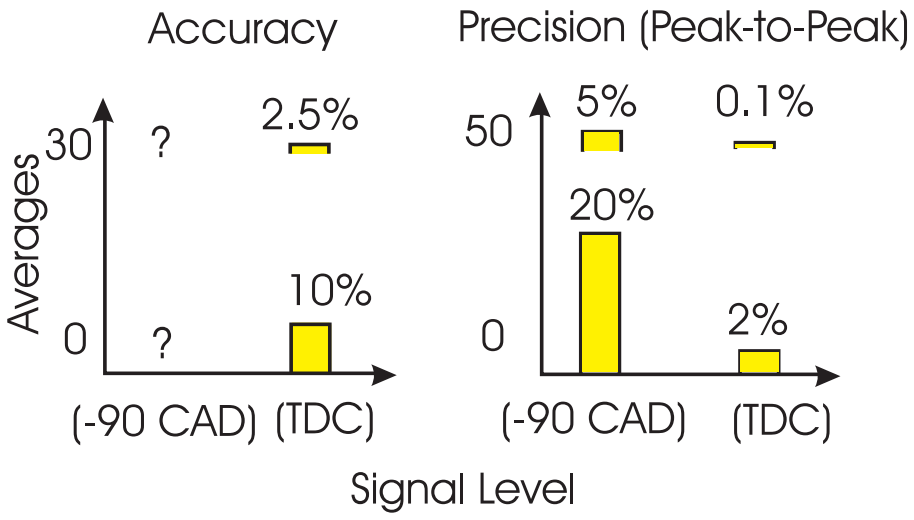

Figure 11-1 – Accuracy uncertainty and precision temperature summary up to 1000 K.

Temperature results greater than 1000 K have been shown to be biased low. This is a major concern since the main function of the sensor is high temperature combustion studies. Preliminary studies indicate that using a better database for reference spectra should improve these high temperature results.

Figure 11-2 summarizes the mole fraction results. Precision, which is easy to measure, is worse in the mole fraction results compared to the temperature results. Mole fraction will be more sensitive to laser performance, therefore as wavelength-agile lasers improve, so also should mole fraction precision. Accuracy has been difficult to quantify. For the engine measurements, when the measured mole fraction is compared to the mole fraction measured from the exhaust gas, the results show an average of 87% accuracy in the high signal levels. Some of the results are within 1% of the ideal combustion mole fraction (X ideal), while others are off by more than 20%. Room humidity, which would be considered a low signal level, has been measured to be within

5% of the actual humidity with averaging in the engine. Further studies should be performed to quantify the absolute accuracy of the mole fraction results.

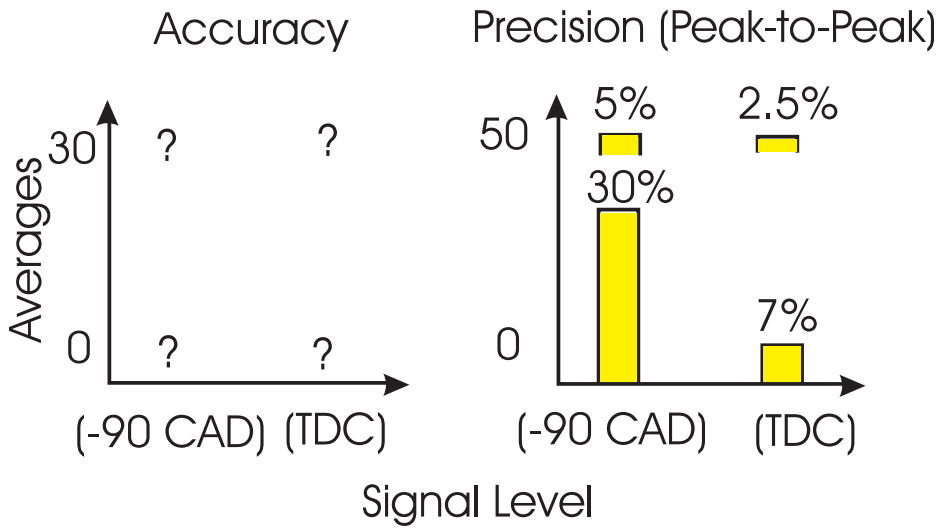

Figure 11-2– Accuracy uncertainty and precision mole fraction summary.

11.2 Recommendations for Future Work

Wavelength-agile laser technology will continue to improve, making faster scanning lasers at higher spectral resolutions. As these improvements occur, the focus of future work should be to first verify the spectroscopic databases. A good first step will be to implement the BT2 database into the calculations. This database has already been shown to improve the accuracy of the results for high temperature measurements. As wavelength-agile resolution and scan-to-scan stability improves, H_2O mole fraction results should also continue to improve in precision and accuracy. With each improvement to the laser system, tests should be performed to verify the accuracy. As laser bandwidth improves, this technique should be extended to other species, as well as multiple species. Finally, this technique provides a path integrated measurement. Multi-beams or tomographic reconstruction could allow quantitative temperature distributions measurements to be achieved.

References

[1] Ku, J. C., and Greenberg, P. S., 1997, "Temperature and radiative heat flux measurements in microgravity jet diffusion flames," Proceedings of the 1997 4th International Microgravity Combustion Workshop, May 19-21 1997, Cleveland, OH, USA, pp. 211-216.

[2] Anderson, T. N., Lucht, R. P., and Meyer, T. R., 2005, "Diode-Laser-Based Ultraviolet-Absorption Sensor for High-Speed Detection of the Hydroxyl Radical," Optics Letters, 30(11), pp. 1321-3.

[3] Hult, J., Burns, I. S., and Kaminski, C. F., 2005, "Two-Line Atomic Fluorescence Flame Thermometry using Diode Lasers," Proceedings of the Combustion Institute, 30(1), pp. 1535-1543.

[4] Schulz, C., and Sick, V., 2005, "Tracer-LIF Diagnostics: Quantitative Measurement of Fuel Concentration, Temperature and fuel/air Ratio in Practical Combustion Systems," Progress in Energy and Combustion Science, 31(1), pp. 75-121.

[5] Meyer, T. R., Roy, S., and Lucht, R. P., 2005, "Dual-Pump Dual-Broadband CARS for Exhaust-Gas Temperature and CO_2-O_2-N_2 Mole-Fraction Measurements in Model Gas-Turbine Combustors," Combustion and Flame, 142(1-2), pp. 52-61.

[6] Malarski, A., Beyrau, F., and Leipertz, A., 2005, "Interference Effects of C/sub 2/-Radicals in Nitrogen Vibrational CARS Thermometry using a Frequency-Doubled Nd:YAG Laser," Journal of Raman Spectroscopy, 36(2), pp. 102-8.

[7] Jeffries, J. B., Schulz, C., and Mattison, D. W., 2004, "UV Absorption of CO/sub 2/ for Temperature Diagnostics of Hydrocarbon Combustion Applications," Proceedings of the Combustion Institute, 30(1), pp. 1591-9.

[8] Hendricks, A. G., Vandsburger, U., and Saunders, W. R., 2006, "The use of Tunable Diode Laser Absorption Spectroscopy for the Measurement of Flame Dynamics," Measurement Science & Technology, 17(1), pp. 139-44.

[9] Allen, M. G., 1998, "Diode Laser Absorption Sensors for Gas Dynamic and Combustion Flows," Measurement Science and Technology, 9(4), pp. 545-562.

[10] Kohse-Höinghaus, K., and Jeffries, J.B., 2002, "Applied Combustion Diagnostics," Taylor & Francis, New York.

[11] Eckbreth, A., 1996, "Laser Diagnostics for Combustion Temperature and Species," Overseas Publishers Association, Amsterdam, The Netherlands.

[12] Varghese, P. L., and Villarreal, R., 2005, "Frequency Resolved Absorption Tomography with Tunable Diode Lasers," Applied Optics, Laser Diagnostics for Gasdynamics.

[13] Sanders, S. T., Wang, J., and Jeffries, J. B., 2001, "Diode-Laser Absorption Sensor for Line-of-Sight Gas Temperature Distributions," Applied Optics, 40, pp. 4405-4415.

[14] Rothman, L. S., Rinsland, C. P., and Goldman, A., 1996, "The HITRAN Molecular Spectroscopic Database and HAWKS (HITRAN Atmospheric Workstation): 1996 Edition," J.Quant.Spectrosc.Radiat.Transf., 60(5), pp. 665-710.

[15] Rothman, L. S., Jacquemart, D., and Barbe, A., 2005, "The HITRAN 2004 Molecular Spectroscopic Database," Journal of Quantitative Spectroscopy and Radiative Transfer, 96(2 SPEC ISS), pp. 139-204.

[16] Whiting, E. E., 1968, "An Empirical Approximation to the Voigt Profile," Journal of Quantitative Spectroscopy and Radiative Transfer, 8(6), pp. 1374-1384.

[17] Hui, A. K., Armstrong, B. H., and Wray, A. A., 1978, "Rapid Computation of the Voigt and Complex Error Functions," Journal of Quantitative Spectroscopy and Radiative Transfer, 19(5), pp. 509-16.

[18] Kranendonk, L. A., Caswell, A. W., and Sanders, S. T., submitted 2006, "Robust Method for Calculating Temperature, Pressure and Absorber Mole Fraction from Broadband Spectra," submitted to: Applied Optics.

[19] Zhou, X., Jeffries, J. B., and Hanson, R. K., 2005, "Development of a Fast Temperature Sensor for Combustion Gases using a Single Tunable Diode Laser," Applied Physics B (Lasers and Optics), B81(5), pp. 711-22.

[20] Liu, X., Jeffries, J. B., and Hanson, R. K., 2006, "Development of a Tunable Diode Laser Sensor for Measurements of Gas Turbine Exhaust Temperature," Applied Physics B (Lasers and Optics), B82(3), pp. 469-78.

[21] Hanson, R. K., Kuntz, P. A., and Kruger, C. H., 1977, "High-Resolution Spectroscopy of Combustion Gases using a Tunable Ir Diode-Laser," Applied Optics, 16, pp. 2045-2048.

[22] Sanders, S. T., 2001, "Diode-Laser Sensors for Harsh Environments with Application to Pulse Detonation Engines," Ph.D. thesis, Stanford University, Palo Alto, CA.

[23] Sanders, S. T., Mattison, D. W., and Jeffries, J. B., 2001, "Rapid Temperature Tuning of a 1.4-Um Diode Laser with Application to High-Pressure H2O Absorption Spectroscopy," Opt.Lett., 26, pp. 1568-1570.

[24] Sanders, S. T., Mattison, D. W., and Ma, L., 2002, "Wavelength-Agile Diode-Laser Sensing Strategies for Monitoring Gas Properties in Optically Harsh Flows: Application in Cesium-Seeded Pulse Detonation Engine," Optics Express, 10, pp. 505-514.

[25] Sanders, S. T., 2002, "Wavelength-Agile Fiber Laser using Group-Velocity Dispersion of Pulsed Super-Continua and Application to Broadband Absorption Spectroscopy," Applied Physics B: Lasers and Optics, 75, pp. 799-802.

[26] Sanders, S. T., Kim, T., and Ghandhi, J. B., 2003, "Gas Temperature Measurements during Ignition in an HCCI Engine," SAE Paper 2003-01-0744, .

[27] Kranendonk, L. A., Caswell, A. W., and Myers, A. N., 2003, "Wavelength-Agile Laser Sensors for Measuring Gas Properties in Engines," SAE 2003 Transactions Journal of Engines, pp. 1578-1583.

[28] Kranendonk, L. A., Walewski, J. W., and Kim, T., 2005, "Wavelength-Agile Sensor Applied for HCCI Engine Measurements," Proceedings of the Combustion Institute, 30(1), pp. 1619-1627.

[29] Walewski, J. W., and Sanders, S. T., 2004, "High-Resolution Wavelength-Agile Laser Source Based on Pulsed Super-Continua," Applied Physics B: Lasers and Optics, 79(4), pp. 415-418.

[30] Walewski, J. W., Borden, M. R., and Sanders, S. T., 2004, "Wavelength-Agile Laser System Based on Soliton Self-Shift and its Application for Broadband Spectroscopy," Applied Physics B: Lasers and Optics, 79(8), pp. 937-940.

[31] Pertzborn, A. J., Walewski, J. W., and Sanders, S. T., 2005, "Wavelength-Agile Source Based on a Potassium Atomic Vapor Cell and Application for Absorption Spectroscopy of Iodine," Optics Communications, 254(1-3), pp. 173-173-183.

[32] Kranendonk, L. A., Bartula, R. J., and Sanders, S. T., 2005, "Modeless Operation of a Wavelength-Agile Laser by High-Speed Cavity Length Changes," Optics Express, 13(5), pp. 1498-1507.

[33] Huber, R., Wojtkowski, M., and Fujimoto, J. G., 2006, "Fourier Domain Mode Locking (FDML): A New Laser Operating Regime and Application for Optical Coherence Tomography," Optics Express, 14(8), pp. 3225-3237.

[34] Liu, K., and Littman, M. G., 1981, "Novel Geometry for Single-Mode Scanning of Tunable Lasers," Optics Letters, 6(3).

[35] Wippich, M., and Dessau, K. L., 2003, "Tunable Lasers Enhance Fiber Sensors," Laser Focus World, 39**,** pp. 89-94.

[36] Yun, S. H., Tearney, G. J., and Boer, J. F. d., 2003, "High-Speed Optical Frequency-Domain Imaging," Optics Express, 11(22), pp. 2953-2963.

[37] Yun, S. H., Boudoux, C., and Tearney, G. J., 2003, "High-Speed Wavelength-Swept Semiconductor Laser with a Polygon-Scanner-Based Wavelength Filter," Optics Letters, 28(20), pp. 1981-1983.

[38] Pilgrim, J. S., 2002, "Wavelength Agile External Cavity Diode Laser for Trace Gas Detection," Trends in Optics and Photonics, 69.

[39] Lim, M. J., Sukenik, C. I., and Stievater, T. H., 1998, "Improved Design of a Frequency-Shifted Feedback Diode Laser for Optical Pumping at High Magnetic Field," Optics Communications, 147(1-3), pp. 99-102.

[40] Yoshizawa, A., and Tsuchida, H., 1998, "Chirped-Comb Generation in Frequency-Shifted Feedback Laser Diodes with a Large Frequency Shift," Optics Communications, 155(1-3), pp. 51-54.

[41] Huber, R., Wojtkowski, M., and Taira, K., 2005, "Amplified, Frequency Swept Lasers for Frequency Domain Reflectometry and OCT Imaging: Design and Scaling Principles," Optics Express, 13(9), pp. 3513-3528.

[42] Huber, R., Taira, K., and Wojtkowski, M., 2005, "Fourier Domain Mode Locked Lasers for OCT Imaging at Up to 290 kHz Sweep Rates," Proceedings of OSA-SPIE Biomedical Optics, 5861(58611B).

[43] Huber, R., Taira, K., and Fujimoto, J. G., 2005, "Fourier Domain Mode Locking: Overcoming Limitations of Frequency Swept Light Sources and Pulsed Lasers," Conference on Lasers and Electro-Optics Europe/ European Quantum Electronics Conference, CP3-5-THU.

[44] Kranendonk, L. A., Walewski, J. W., and Sanders, S. T., 2006, "Measurements of Gas Temperature in a HCCI Engine using a Fourier Domain Mode Locking Laser," Society of Automotive Engines, SAE Paper 2006-01-1366.

[45] Younger, S., 2005, "OH Absorption Spectroscopy to Investigate Light-Load HCCI Combustion," Master's thesis, University of Wisconsin, Madison, WI.

[46] Bright, A. G., 2004, "Residual Gas Mixing in Engines," Master's thesis, University of Wisconsin, Madison, WI.

[47] Kranendonk, L. A., and Sanders, S. T., 2005, "Optical Design in Beam Steering Environments with Emphasis on Laser Transmission Measurements," Applied Optics, 44(31), pp. 6762-6772.

[48] Anderson, M. H., Puranik, B. P., and Oakley, J. G., 2000, "Shock Tube Investigation of Hydrodynamic Issues Related to Inertial Confinement Fusion," Shock Waves, 10(5), pp. 377-87.

[49] Radi, P. P., Mischler, B., and Schlegel, A., 1999, "Absolute Concentration Measurements using DFWM and Modeling of OH and S_2 in a Fuel-Rich H_2/air/SO_2 Flame," Combustion and Flame, 118(1-2), pp. 301-307.

[50] Sanders, S. T., Mattison, D. W., and Ma, L., 2002, "Wavelength-Agile Diode-Laser Sensing Strategies for Monitoring Gas Properties in Optically Harsh Flows: Application in Cesium-Seeded Pulse Detonation Engine," Optics Express, 10, pp. 505-514.

[51] Wehe, S. D., Baer, D. S., and Hanson, R. K., 1999, "Diode-Laser Sensor for Velocity Measurements in Hypervelocity Flows," AIAA Journal, 37**,** pp. 1013-1015.

[52] Supplee, J. E., Whittaker, E. A., and Lenth, W., 1994, "Theoretical Description of Frequency Modulation and Wavelength Modulation Spectroscopy," Applied Optics, 33(27), pp. 6294-6302.

[53] Peterson, E. L., 1998, "A Shock Tube and Diagnostic for Chemistry Measurements at Elevated Pressures with Application to Methane Ignition," Ph.D. thesis, Stanford University, Palo Alto, CA.

[54] Jumper, E. J., and Fitzgerald, E. J., 2001, "Recent Advances in Aero-Optics," Progress in Aerospace Sciences, 37**,** pp. 299-399.

[55] Landolt-Bornstein, 1962, "Zahlenwerte und Funktionen aus Physik, Chemie, Astronomie, Geophysik, und Technik," Springer-Verlag, Berlin.

[56] Born, M., and Wolf, E., 1964, "Principles of Optics," The MacMillan Co., New York.

[57] Musculus, M. P. B., and Pickett, L. M., 2005, "Diagnostic Considerations for Optical Laser-Extinction Measurements of Soot in High-Pressure Transient Combustion Environments," Combustion and Flame, 141(4), pp. 371-391.

[58] Sutton, G. W., 1969, "Effect of Turbulent Fluctuations in an Optically Active Fluid Medium," American Institute of Aeronautics and Astronautics Journal, 7**,** pp. 1737-1743.

[59] Celik, I., and Ibrahin, Y., 1997, "An Assessment of Turbulence Scales Relevant to IC Engines," American Society of Mechanical Engineers, 28(1).

[60] Chernov, L.A., 1960, "Wave Propagation in a Random Medium," McGraw-Hill Book Co., New York.

[61] Welford, W.T., and Winston, R., 1978, "The Optics of Non-Imaging Concentrators," Academic Press, New York.

[62] Young, M., 1986, "Optics and Laser," Springer-Verlag, Berlin.

[63] Steel, W. H., 1974, "Luminosity, Throughput Or Etendue?" Applied Optics, 13(4), pp. 704.

[64] Kee, S. S., Mohammadi, H., and Hirano, Y., 2003, "Experimental Study on Combustion Characteristics and Emissions Reduction of Emulsified Fuels in Diesel Combustion using Rapid Compression," SAE Paper 2003-01-1792.

[65] Corcione, F. E., Merola, S. S., and Vaglieco, B. M., 2001, "Nanometric Particle Formation in Optically Accessible Diesel Engine," SAE Paper 2001-01-1258.

[66] Stoner, M., and Litzinger, T., 1999, "Effects of Structure and Boiling Point of Oxygenated Blending Compounds in Reducing Diesel Emissions," SAE Paper 1999-01-1475.

[67] Tree, D. R., and Dec, J. E., 2001, "Extinction Measurements of in-Cylinder Soot Deposition in a Heavy-Duty DI Diesel Engine," SAE Paper 2001-01-1296.

[68] Atkins, P.W., 2001, "Physical Chemistry," Oxford University Press, Italy, pp. 997.

[69] Banwell, C.N., and McCash, E.M., 1994, "Fundamentals of molecular spectroscopy," McGraw-Hill, London ; New York, pp. 308.

[70] Rothman, L. S., Barbe, A., and Benner, D. C., 2003, "The HITRAN Molecular Spectroscopic Database: Edition of 2000 Including Updates through 2001," J. Quant. Spectrosc. Radiat. Transfer, 82**,** pp. 5-44.

[71] Xin Zhou, Xiang Liu, and Jeffries, J. B., 2003, "Development of a Sensor for Temperature and Water Concentration in Combustion Gases using a Single Tunable Diode Laser," Measurement Science & Technology, 14(8), pp. 1459-68.

[72] Arroyo, M. P., and Hanson, R. K., 1993, "Absorption-Measurements of Water-Vapor Concentration ; Temperature ; and Line-Shape Parameters using a Tunable Ingaasp Diode-Laser," Applied Optics, 32, pp. 6104-6116.

[73] Langlois, S., Birbeck, T. P., and Hanson, R. K., 1994, "Diode-Laser Measurements of H2o Line-Intensities and Self-Broadening Coefficients in the 1.4-Mu-M Region," Journal of Molecular Spectroscopy, 163, pp. 27-42.

[74] Press, W.H., Teukolsky, S.A., and Vetterling, W.T., 1992, "Numerical Recipes in C - The Art of Scientific Computing," Cambridge University Press, New York, NY, pp. 994.

[75] Kranendonk, L. A., Huber, R., and Fujimoto, J. G., 2007, "Wavelength-Agile H_2O Absorption Spectrometer for Thermometry of General Combustion Gases," Proceedings of the Combustion Institute, 31, pp. doi:10.1016/j.proci.2006.08.003.

[76] Barber, R. J., Tennyson, J., and Harris, G. J., 2006, "A High-Accuracy Computed Water Line List," Monthly Notices of the Royal Astronomical Society, 368(3), pp. 1087-94.

[77] Tennyson, J., 2006, "Calculating the Vibration-Rotation Spectrum of Water," Physica Scripta, 73(1), pp. 53-56.

[78] Sjoberg, M., and Dec, J. E., 2004, "An Investigation into Lowest Acceptable Combustion Temperatures for Hydrocarbon Fuels in HCCI Engines," Proceedings of the Combustion Institute, 30(1), pp. 2719-26.

Appendix A: Ideal Gas

50% Argon Diluent:

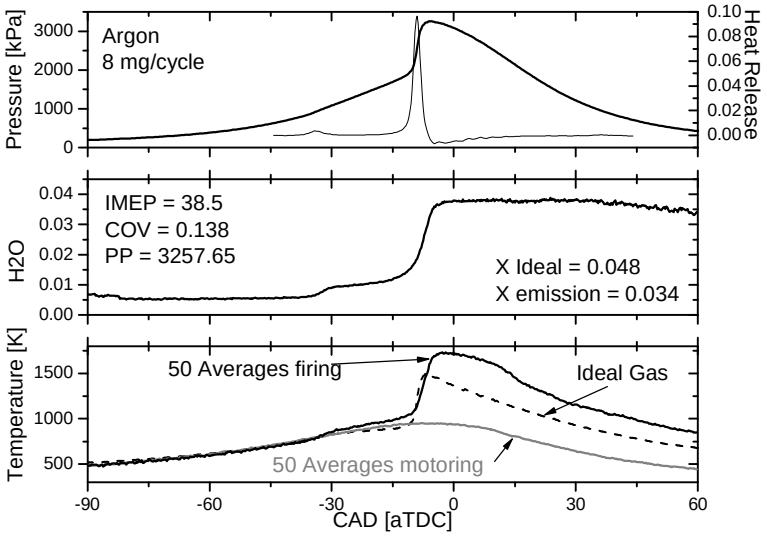

Figure A-3 - Φ = 0.5, 50% Argon, 8 mg fuel/cycle.

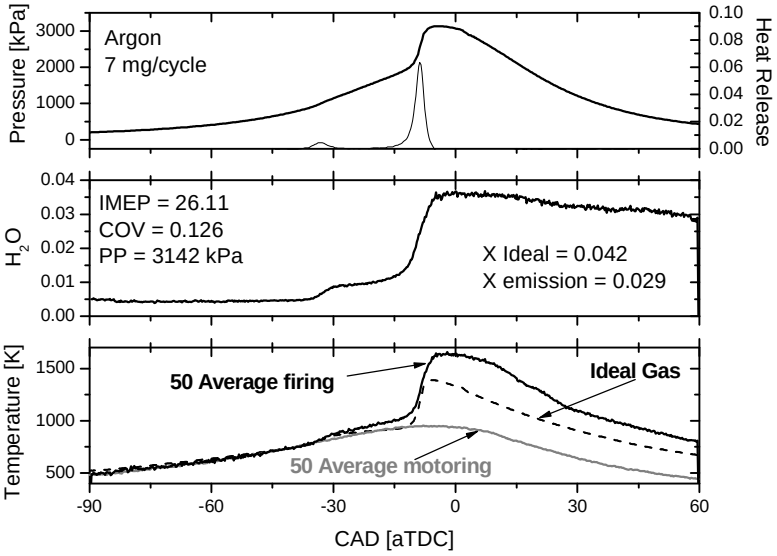

Figure A-4 - Φ = 0.44, 50% Argon, 7 mg fuel/cycle.

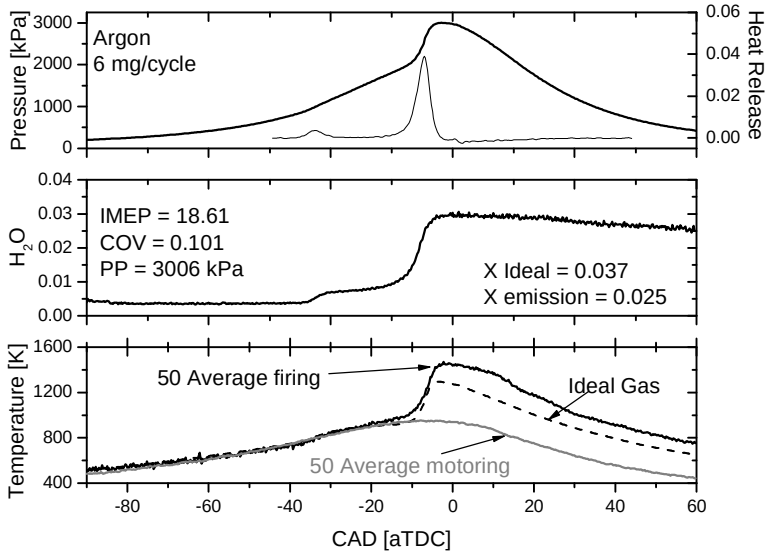

Figure A-5 - Φ = 0.38, 50% Argon, 6 mg fuel/cycle.

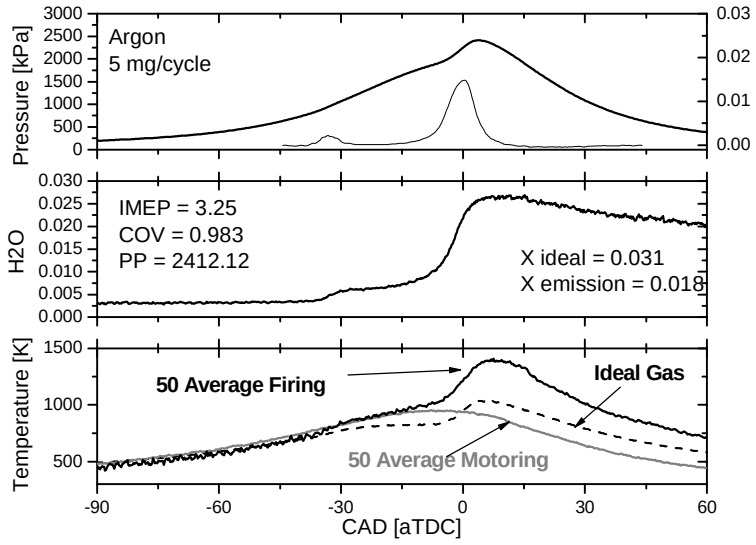

Figure A-6 - Φ = 0.31, 50% Argon, 5 mg fuel/cycle.

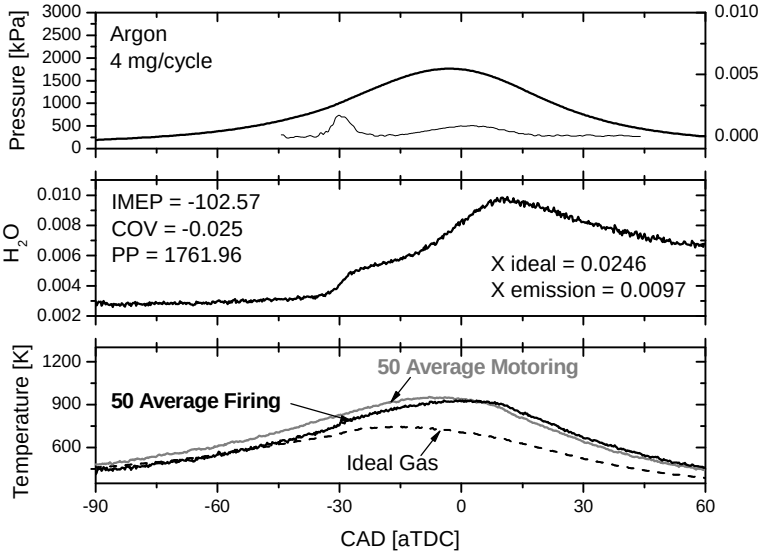

Figure A-7 - Φ = 0.252, 50% Argon, 4 mg fuel/cycle.

100% Inlet Air:

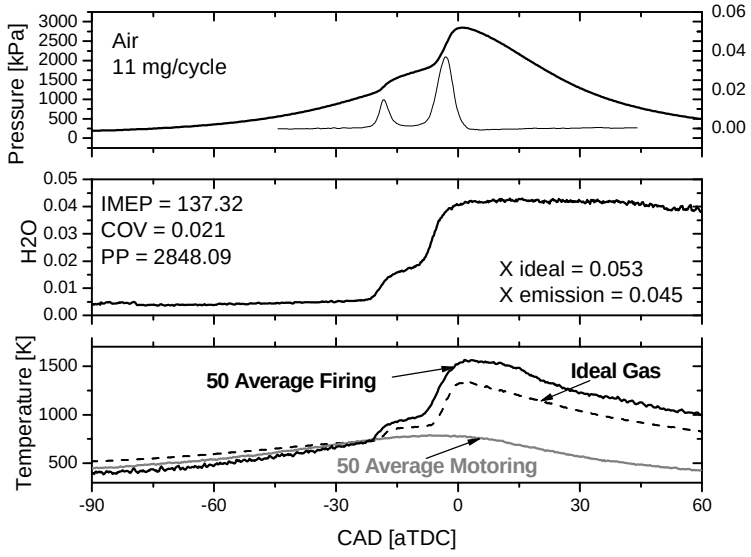

Figure A-8 - Φ = 0.357, 100% Air, 11 mg fuel/cycle.

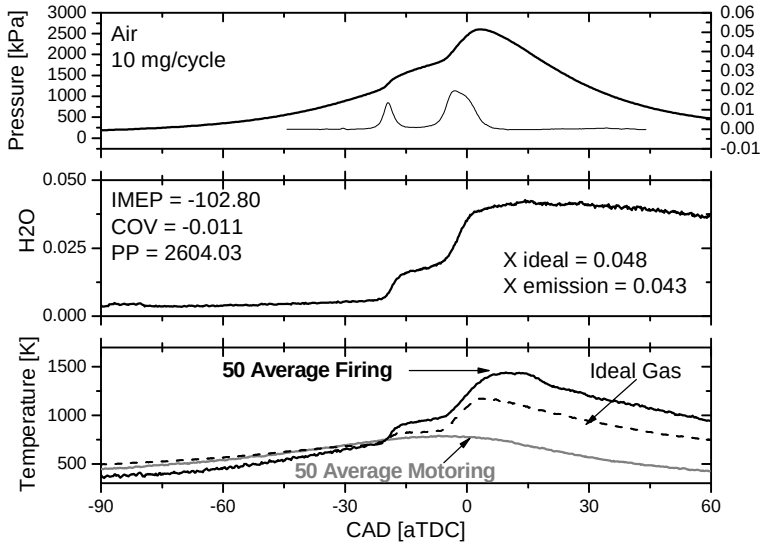

Figure A-9 - Φ = 0.324, 100% Air, 10 mg fuel/cycle.

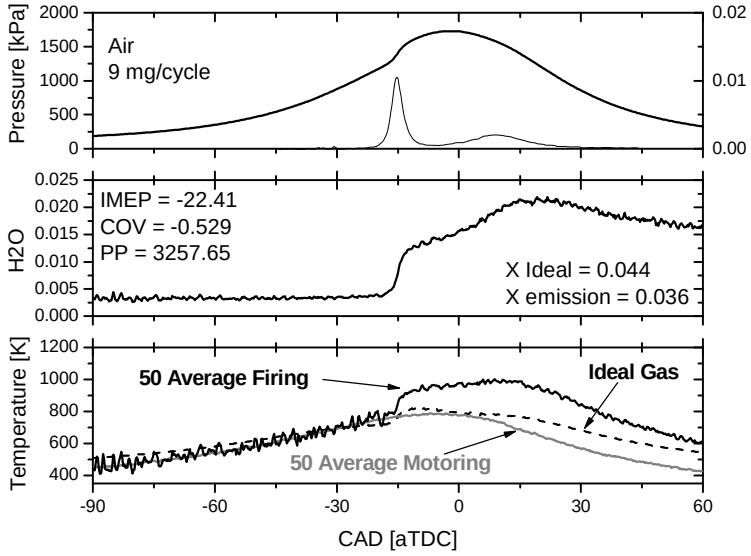

Figure A-10 - Φ = 0.292, 100% Air, 9 mg fuel/cycle.

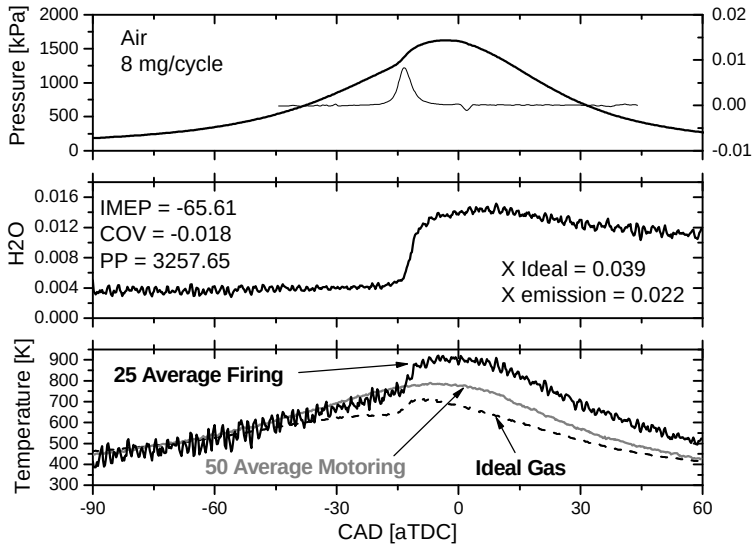

Figure A-11 - Φ = 0.259, 100% Air, 8 mg fuel/cycle.

20% CO_2 Diluent:

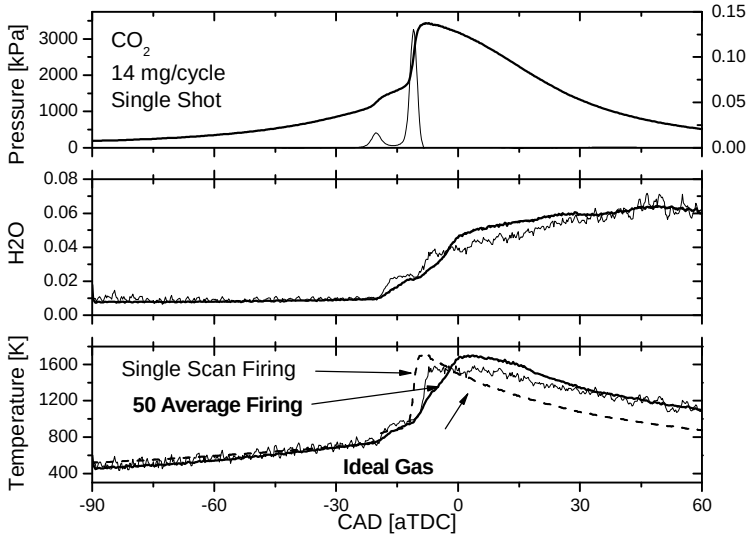

Figure A-12 - Φ = 0.605, 20% CO_2, 14 mg fuel/cycle.

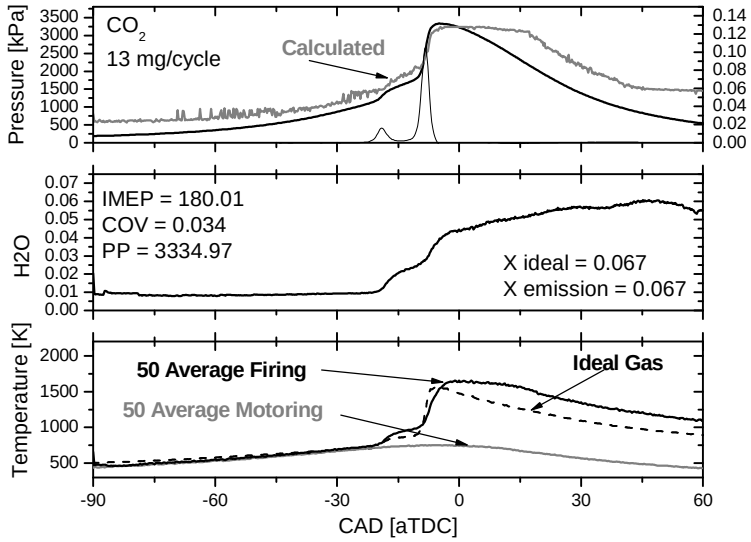

Figure A-13 - Φ = 0.562, 20% CO_2, 13 mg fuel/cycle.

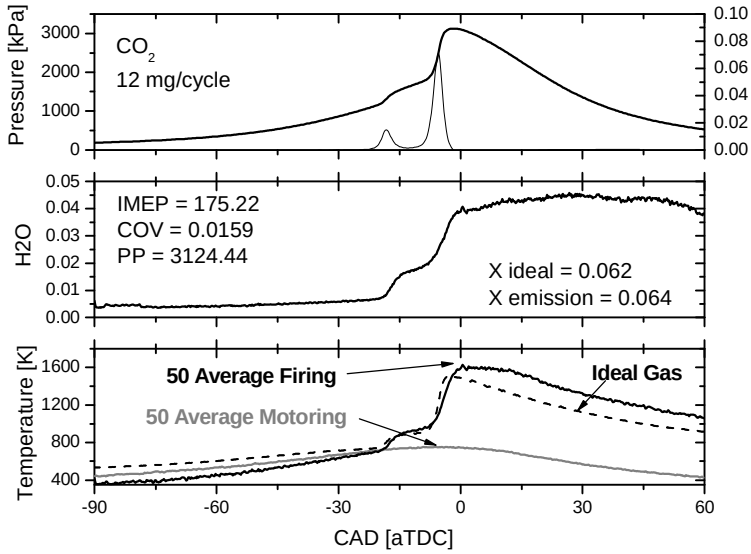

Figure A-14 - Φ = 0.519, 20% CO_2, 12 mg fuel/cycle.

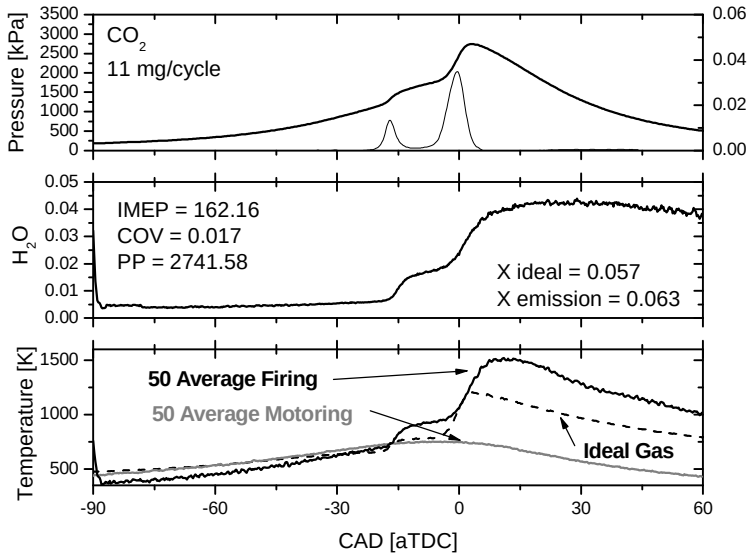

Figure A-15 - Φ = 0.475, 20% CO_2, 11 mg fuel/cycle.

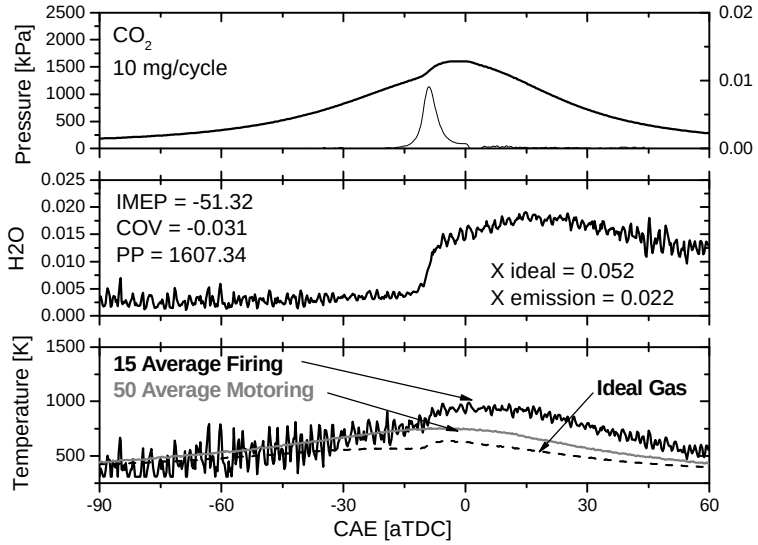

Figure A-16 - Φ = 0.432, 20% CO_2, 10 mg fuel/cycle.

Appendix B: Polytropic Coefficients

50% Argon Diluent:

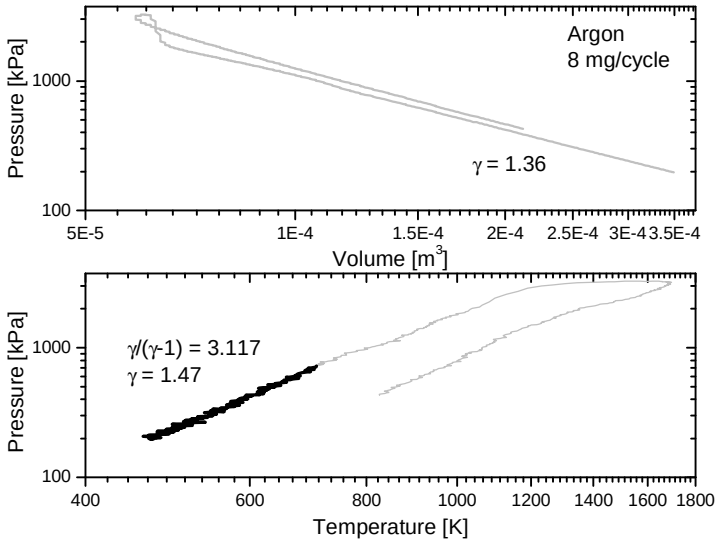

Figure B-1 - Φ = 0.5, 50% Argon, 8 mg fuel/cycle.

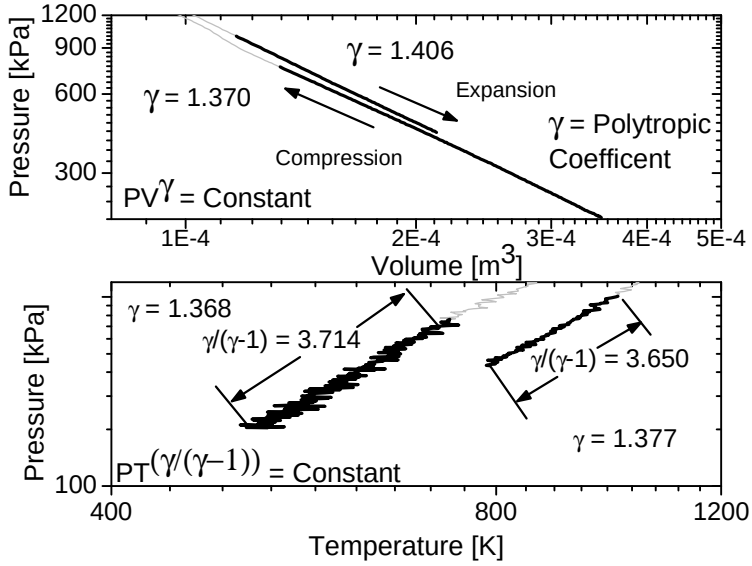

Figure B-2 - Φ = 0.44, 50% Argon, 7 mg fuel/cycle.

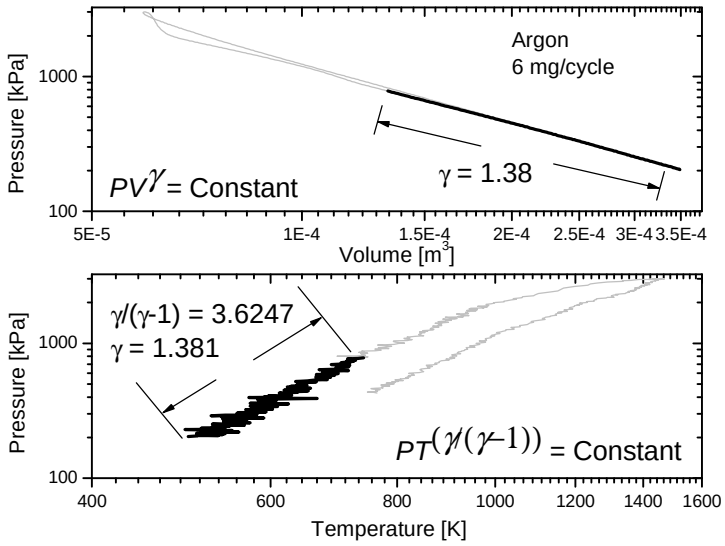

Figure B-3 - Φ = 0.38, 50% Argon, 6 mg fuel/cycle.

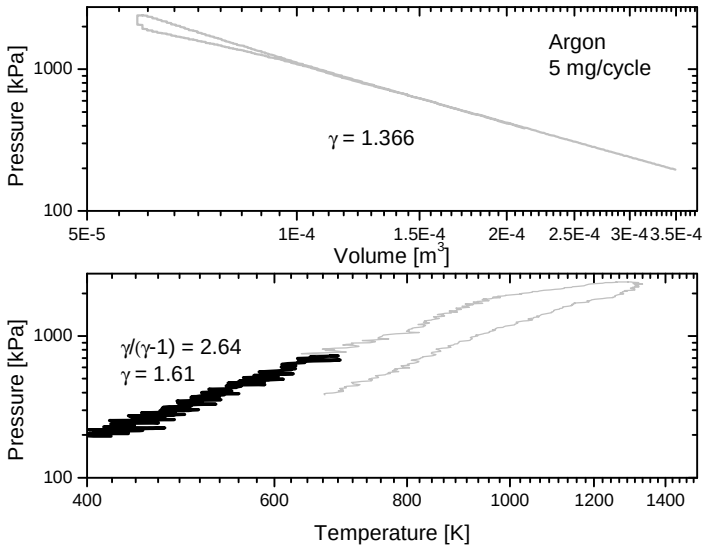

Figure B-4 - Φ = 0.31, 50% Argon, 5 mg fuel/cycle.

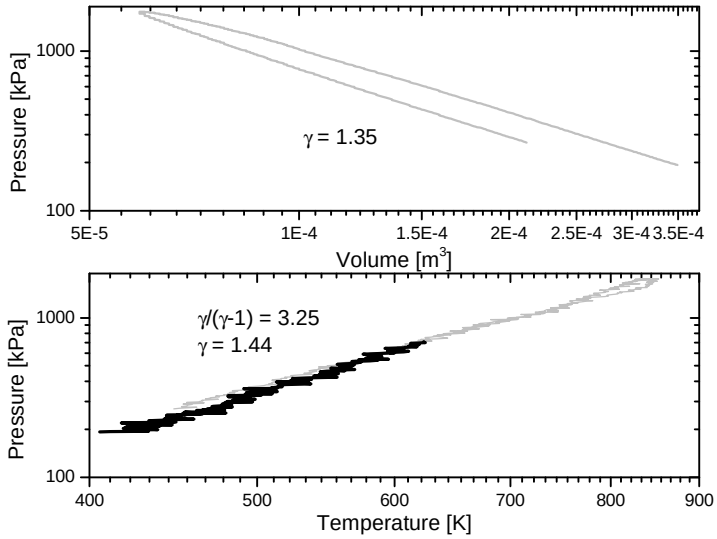

Figure B-5 - Φ = 0.252, 50% Argon, 4 mg fuel/cycle.

100% Inlet Air

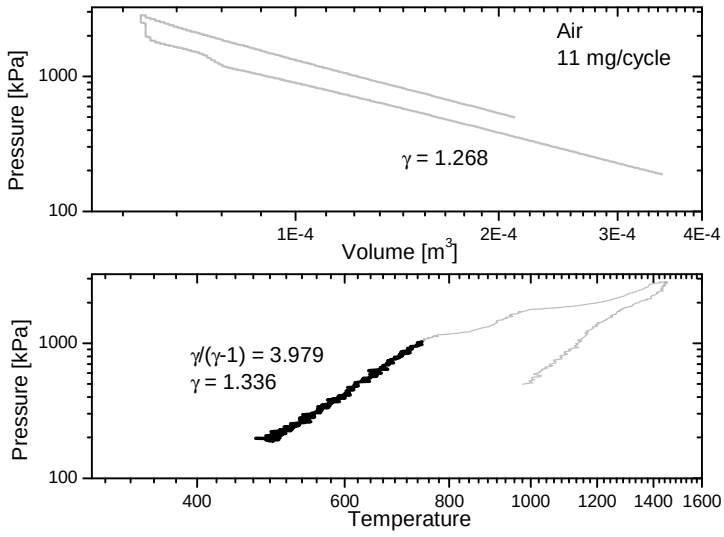

Figure B-6 - Φ = 0.357, 100% Air, 11 mg fuel/cycle.

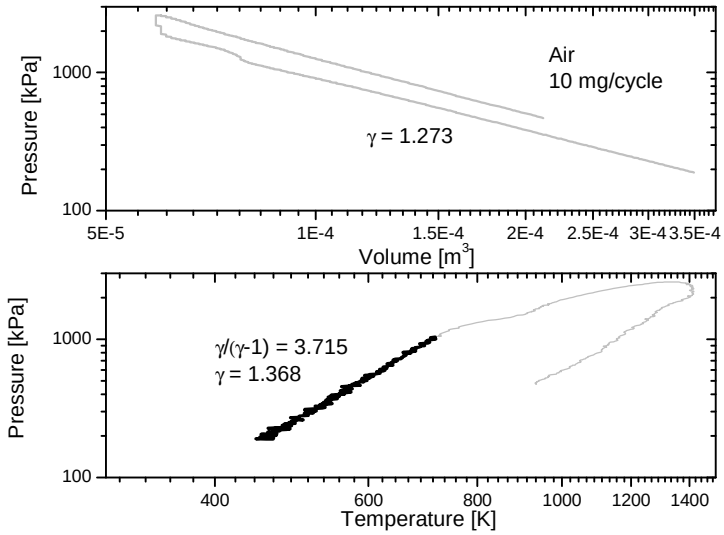

Figure B-7 - Φ = 0.324, 100% Air, 10 mg fuel/cycle.

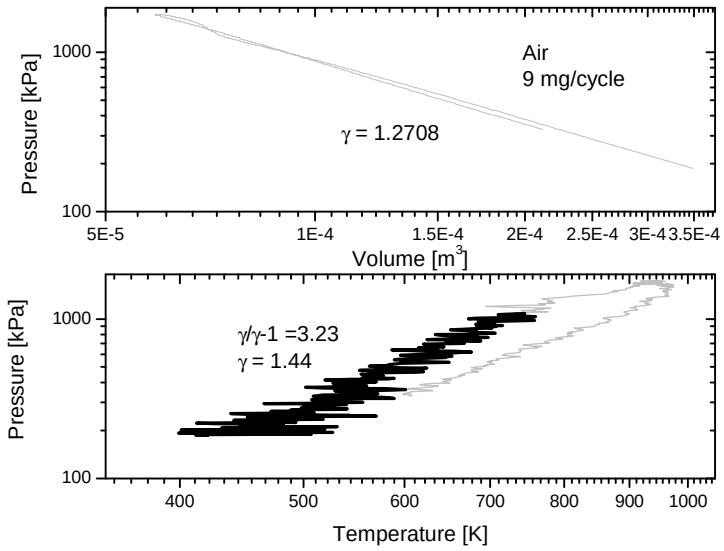

Figure B-8 - Φ = 0.292, 100% Air, 9 mg fuel/cycle.

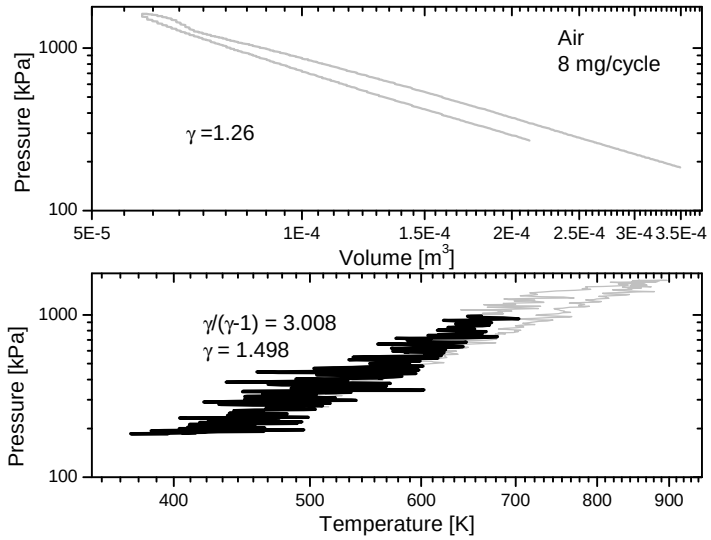

Figure B-9 - Φ = 0.259, 100% Air, 8 mg fuel/cycle.

20% CO_2 Diluent:

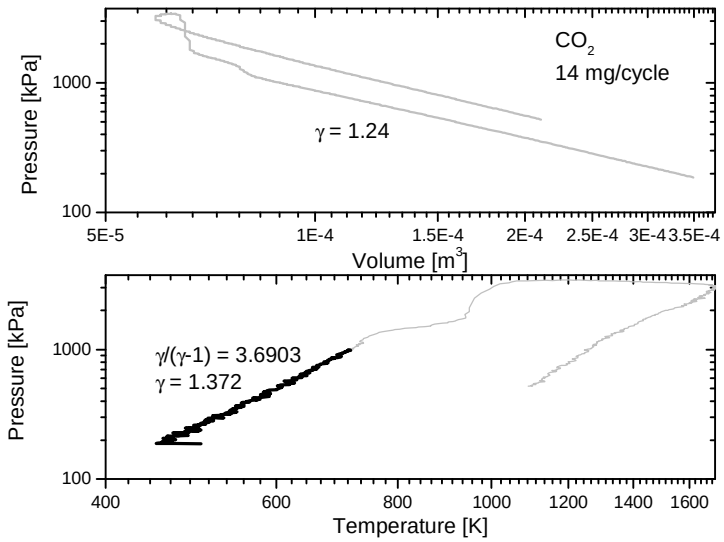

Figure B-10 - Φ = 0.605, 20% CO_2, 14 mg fuel/cycle.

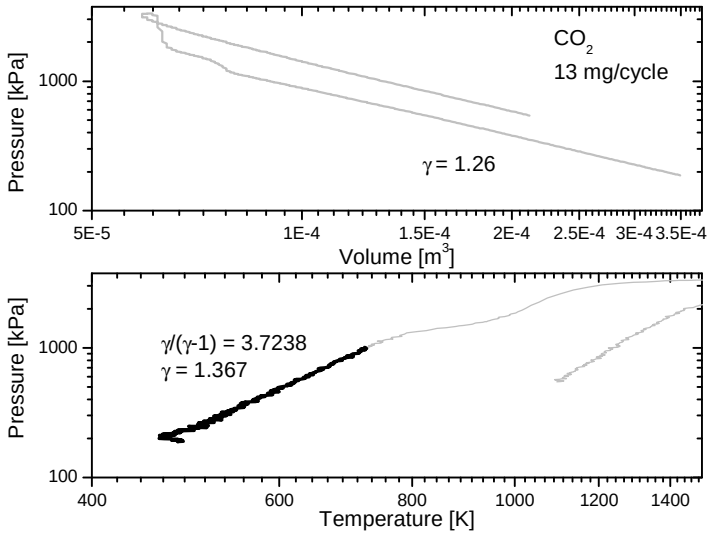

Figure B-11 - $\Phi = 0.562$, 20% CO_2, 13 mg fuel/cycle.

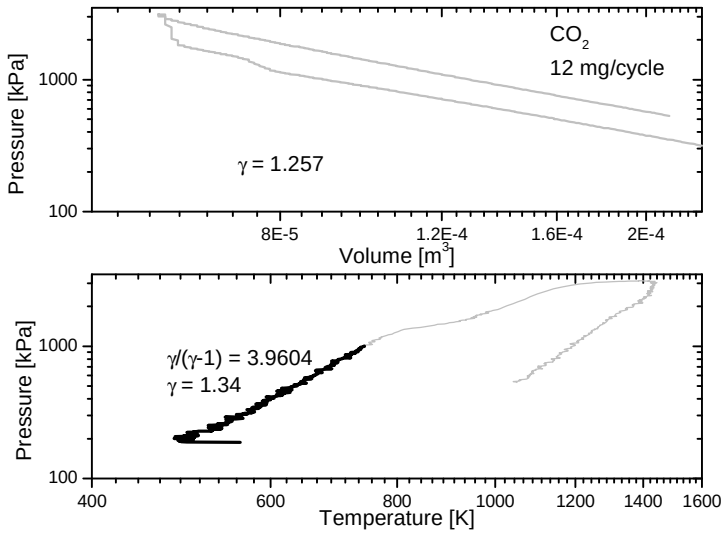

Figure B-12 - $\Phi = 0.519$, 20% CO_2, 12 mg fuel/cycle.

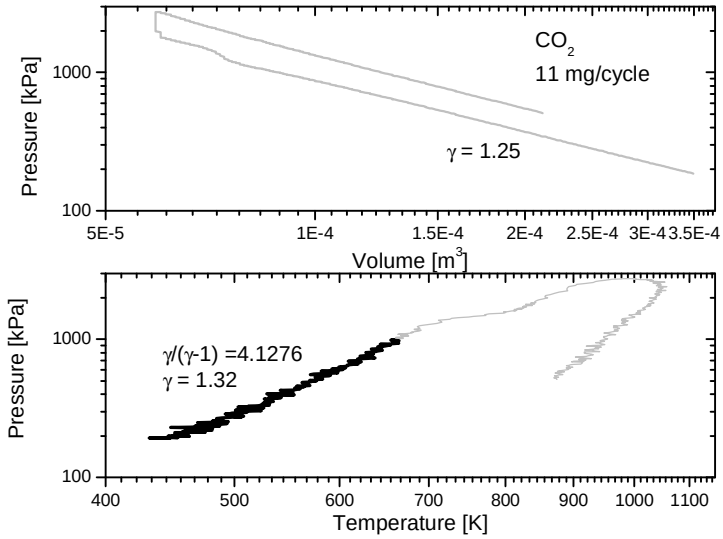

Figure B-13 - Φ = 0.475, 20% CO_2, 11 mg fuel/cycle.

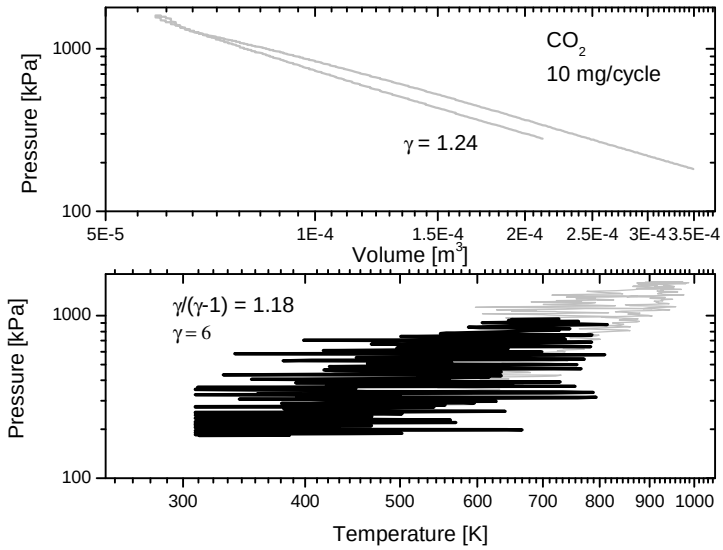

Figure B-14 - Φ = 0.432, 20% CO_2, 10 mg fuel/cycle.

Appendix C: Average vs. Single Scan

50% Argon Diluent

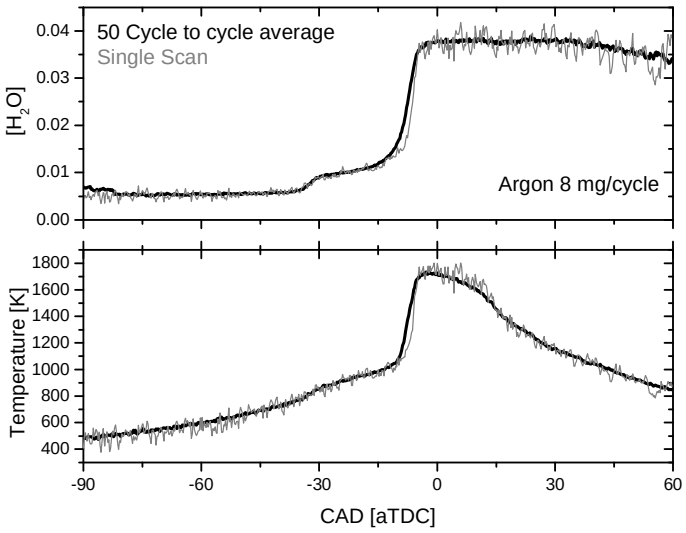

Figure C-1 - Φ = 0.5, 50% Argon, 8 mg fuel / cycle.

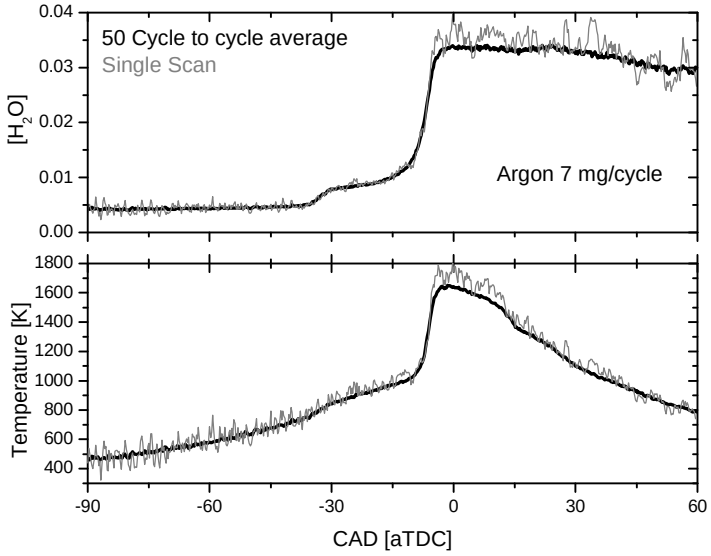

Figure C-2 - Φ = 0.44, 50% Argon, 7 mg fuel / cycle.

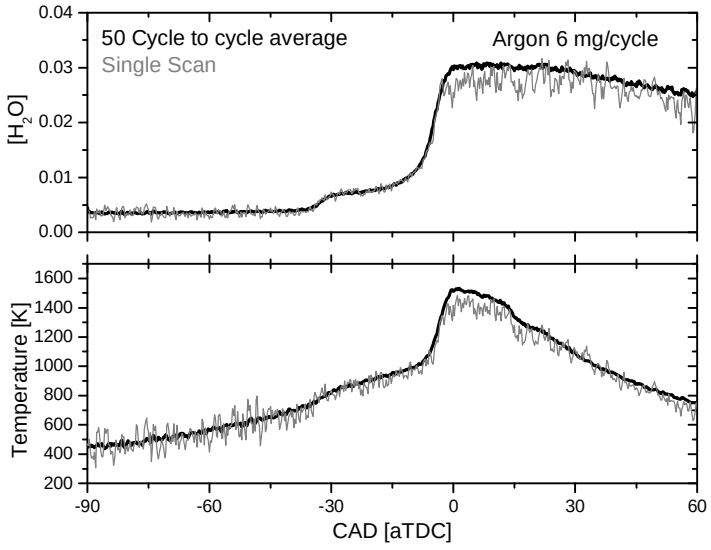

Figure C-3 - Φ = 0.38, 50% Argon, 6 mg fuel / cycle.

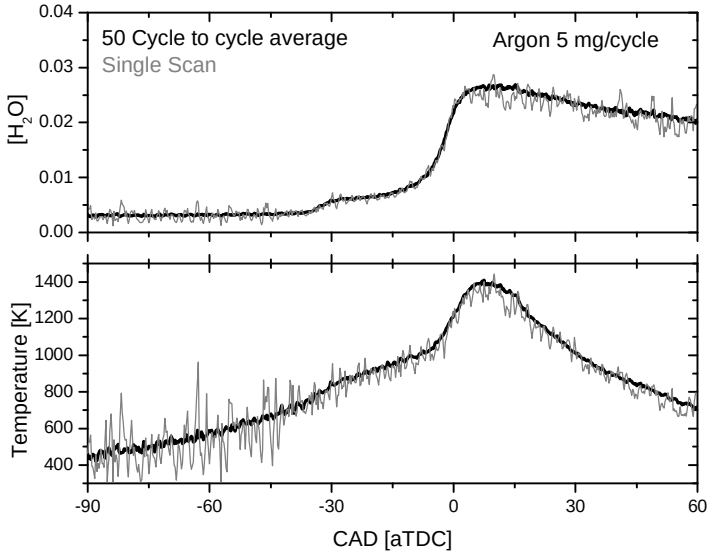

Figure C-4 - Φ = 0.31, 50% Argon, 5 mg fuel / cycle.

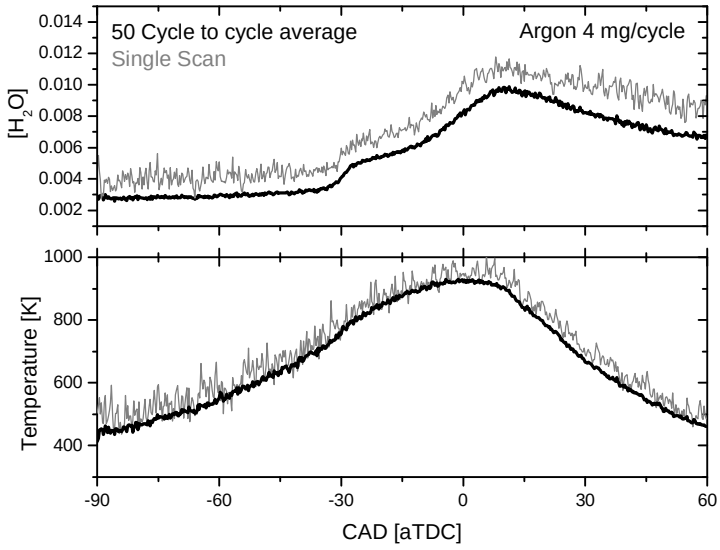

Figure C-5 - Φ = 0.252, 50% Argon, 4 mg fuel / cycle.

100% Inlet Air

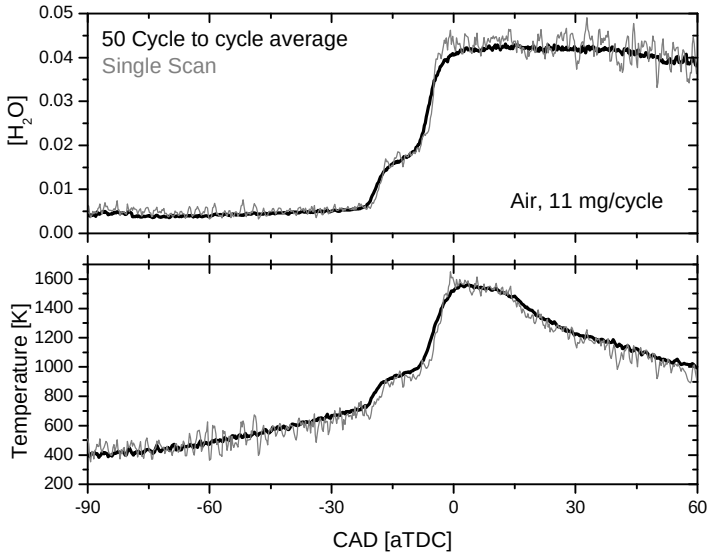

Figure C-6 - Φ = 0.357, 100% Air, 11 mg fuel / cycle.

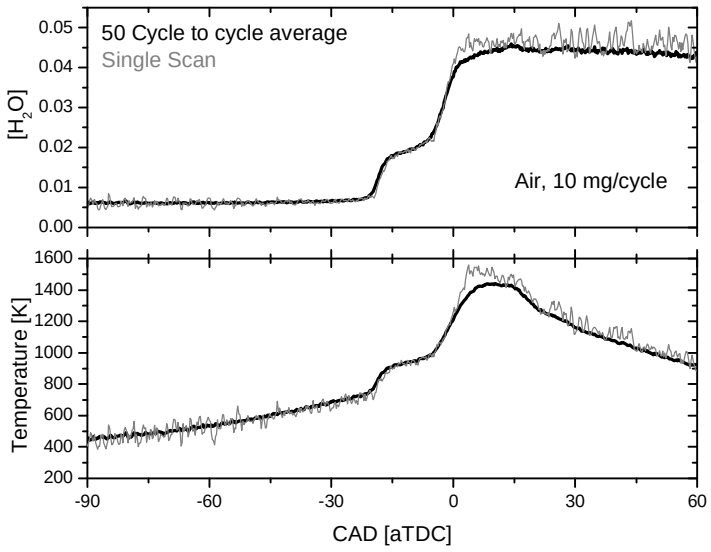

Figure C-7 - Φ = 0.324, 100% Air, 10 mg fuel / cycle.

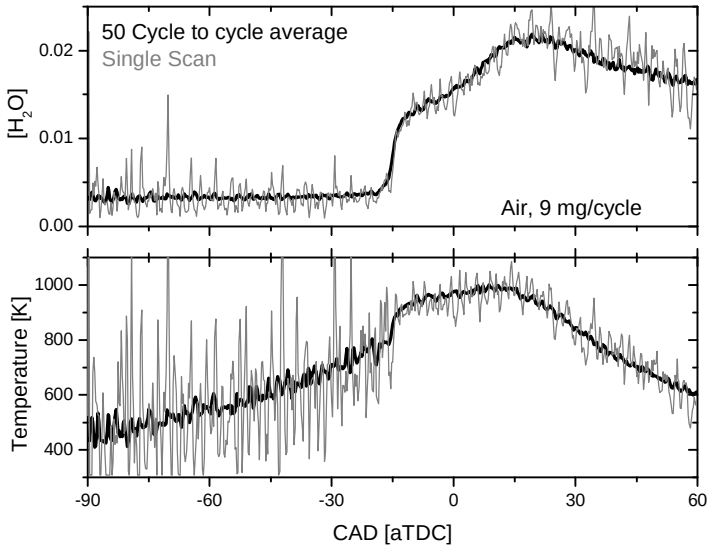

Figure C-8 - Φ = 0.292, 100% Air, 9 mg fuel / cycle.

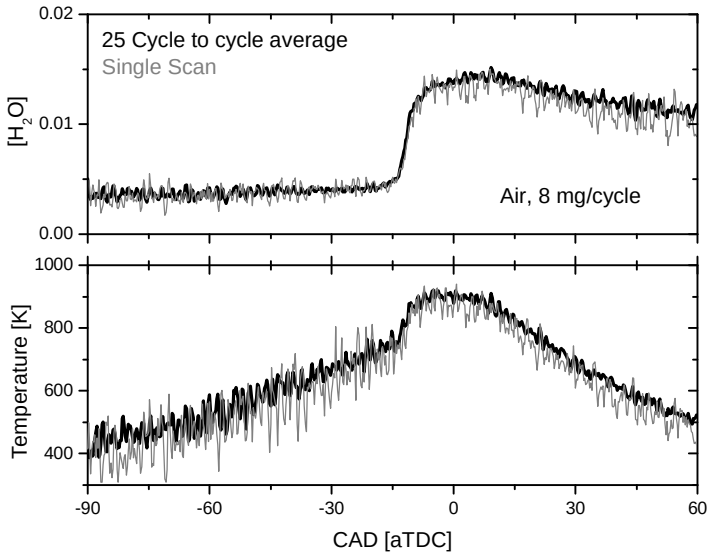

Figure C-9 - Φ = 0.259, 100% Air, 8 mg fuel / cycle.

20% CO_2 Diluent

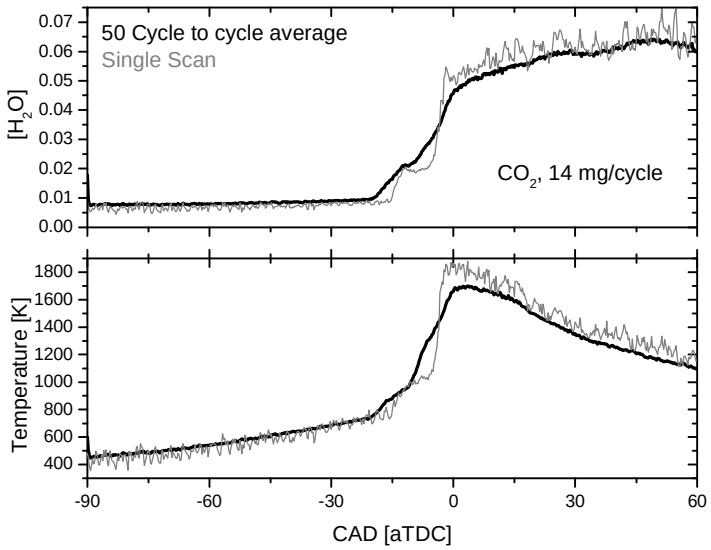

Figure C-10 - Φ = 0.605, 20% CO_2, 14 mg fuel / cycle.

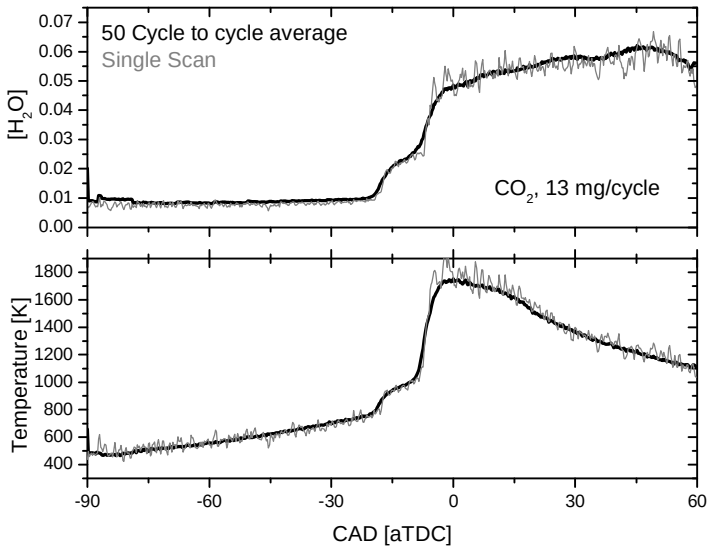

Figure C-11 - Φ = 0.562, 20% CO_2, 13 mg fuel / cycle.

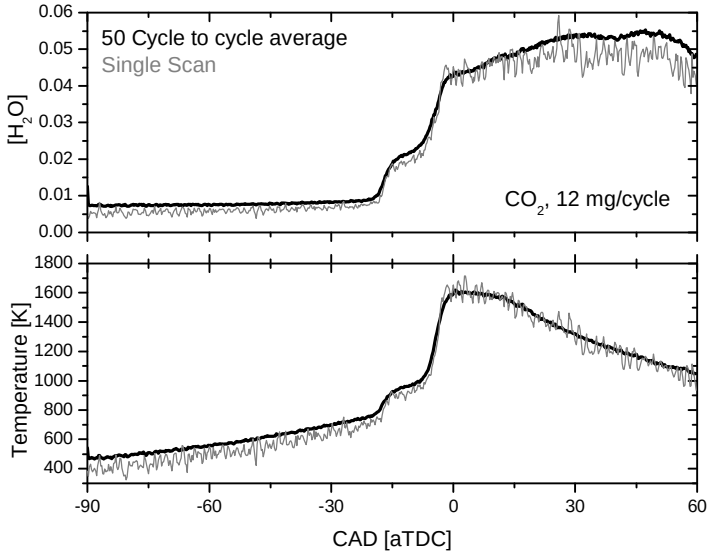

Figure C-12 - Φ = 0.519, 20% CO_2, 12 mg fuel / cycle.

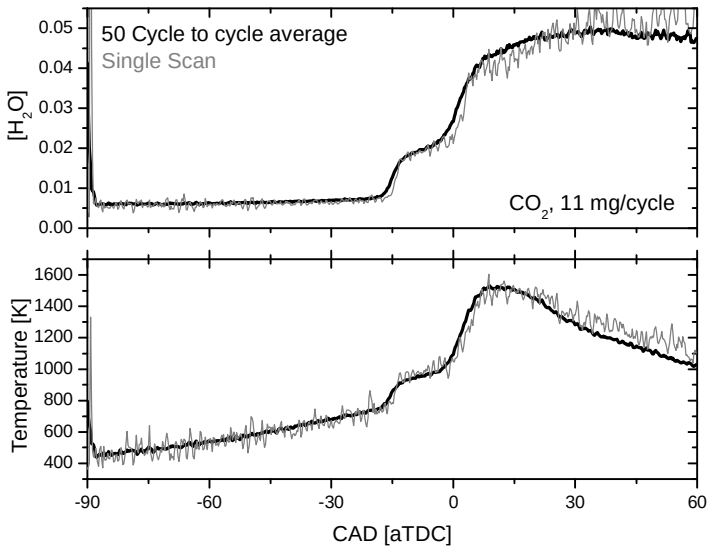

Figure C-13 - Φ = 0.475, 20% CO_2, 11 mg fuel / cycle.

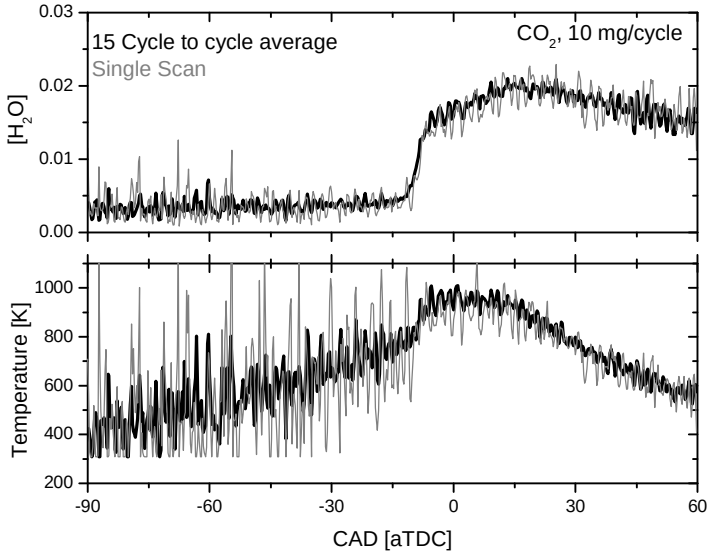

Figure C-14 - $\Phi = 0.432$, 20% CO_2, 10 mg fuel / cycle.

Appendix D: Calibrating Engine Conditions

One of the main issues hindering the experiment described in Chapter 10 was that the data for separate figures was taken over the span of several months. Also, different people were operating and maintaining the engine. These circumstances caused the engine to behave differently under the "same" operation conditions. This appendix describes the process that was used to label the conditions in Chapter 10. It can be assumed in Chapter 10 that an engine run with 50% argon diluent and 7 mg fuel/cycle behaved in the same manner in Figure 10-1 as Figure 10-3. As described below, this assumption is fair because the engine computer unit was not trusted, but rather the measured heat release rates.

The calculated heat release rates are a good measure for defining combustion. Therefore, the heat release from the CO emission experiments were compared to the heat release from the H_2O absorption experiments. Differences in phasing were ignored. When the heat releases were similar enough, the overall condition was defined to be whatever the CO experiment defined. As mentioned in the chapter, this is not a particularly good solution. A better practice would be to eliminate the problem by taking CO emission data on the same day (or even better, simultaneously) as the absorption spectroscopy data. The following figures and tables summarize the results of the heat release analysis.

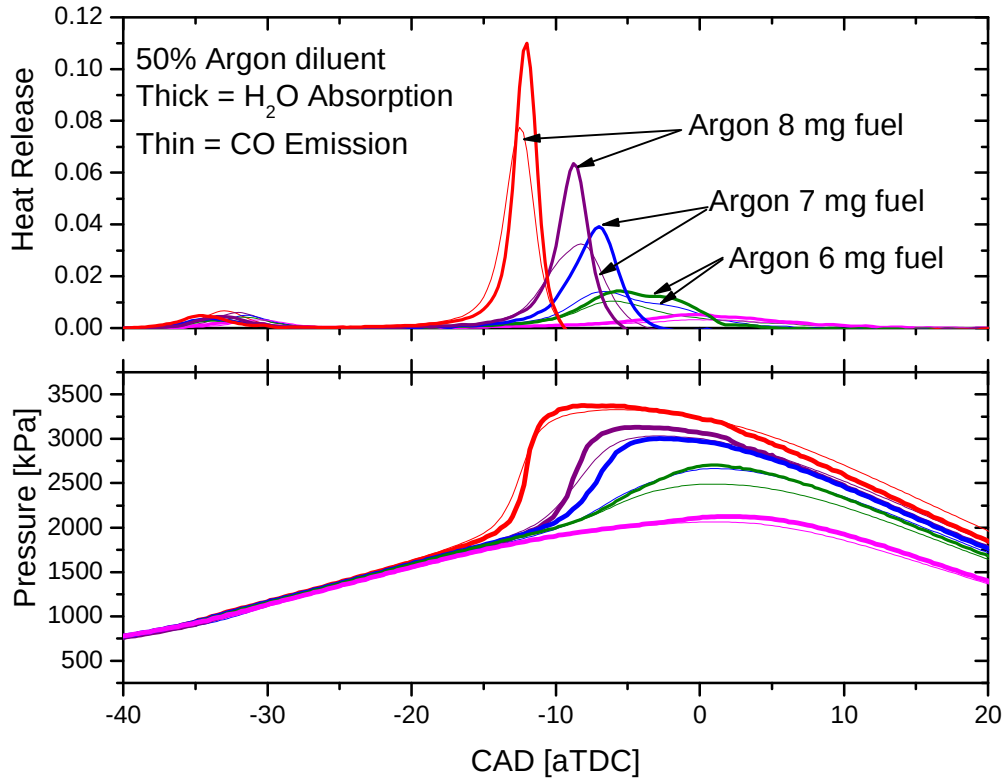

Figure D-1 – Pressure and heat release data for engine cases seeded with argon diluent. Thick lines were measured during the absorption spectroscopy experiment, thin lines during the CO emission measurements.

Engine Conditions for CO Emission	Most similar H_2O Absorption
8 mg fuel / cycle	7 mg fuel / cycle
7 mg fuel / cycle	6 mg fuel / cycle
6 mg fuel / cycle	5 mg fuel / cycle

Table D-1 – Summary of argon diluent organization.

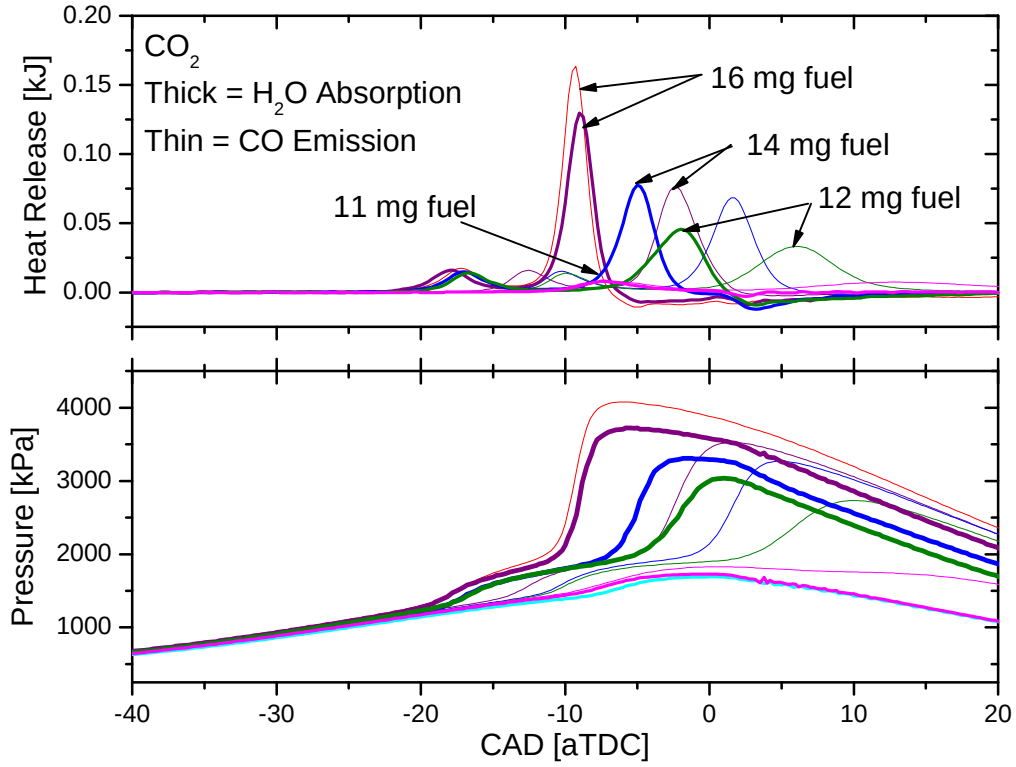

Figure D-2– Pressure and heat release data for engine cases seeded with CO_2 diluent. Thick lines were measured during the absorption spectroscopy experiment, thin lines during the CO emission measurements.

Engine Conditions for CO Emission	Most similar H_2O Absorption
16 mg fuel / cycle	14 mg fuel / cycle
14 mg fuel / cycle	13 mg fuel / cycle
12mg fuel / cycle	12mg fuel / cycle
11mg fuel / cycle	11 mg fuel / cycle

Table D-2 – Summary of CO_2 diluent organization.

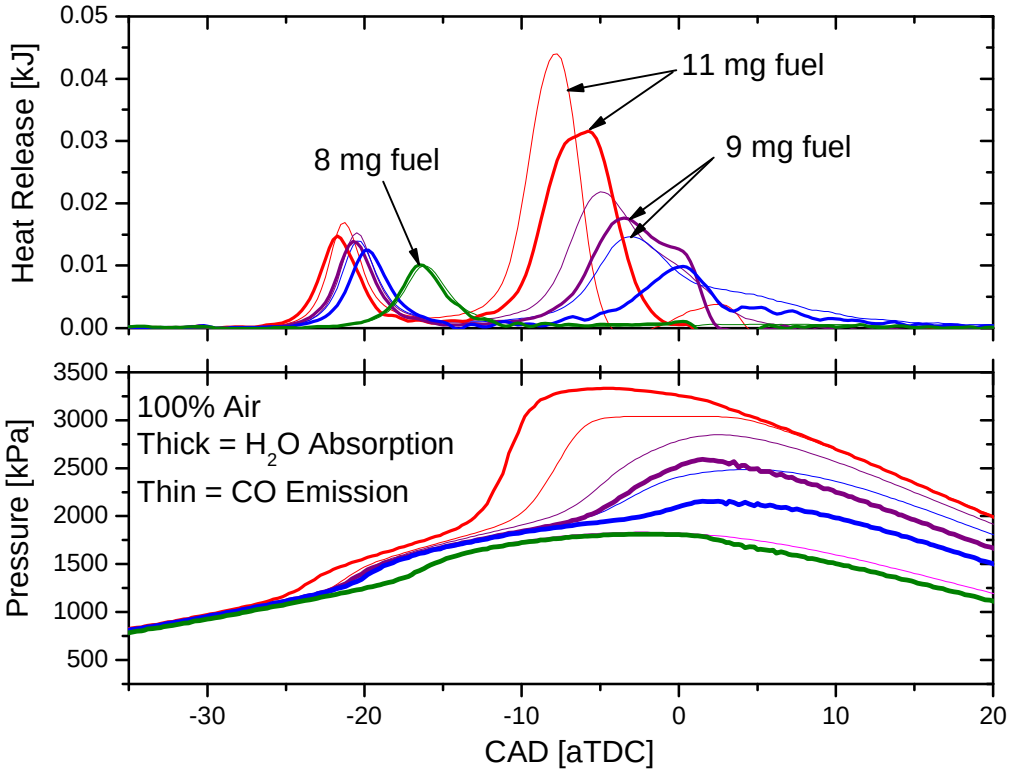

Figure D-3– Pressure and heat release data for engine cases seeded with argon diluent. Thick lines were measured during the absorption spectroscopy experiment, thin lines during the CO emission measurements.

Engine Conditions for CO Emission	Most similar H_2O Absorption
11 mg fuel / cycle	11 mg fuel / cycle
10 mg fuel / cycle	9 mg fuel / cycle
8 mg fuel / cycle	8 mg fuel / cycle

Table D-3 – Summary of 100% air intake organization.